The Dissertation Committee for Morgan Chase Bruns Certifies that this is the approved version of the following dissertation:

Modeling and Simulation of Linear Thermoplastic Thermal Degradation

Committee:

Ofodike A. Ezekoye, Supervisor

Venkat Ganesan

John R. Howell

Joseph H. Koo

Marc R. Nyden

Rodney S. Ruoff

Modeling and Simulation of Linear Thermoplastic Thermal Degradation

by

Morgan Chase Bruns, B.S.M.E.; M.S.M.E.

Dissertation

Presented to the Faculty of the Graduate School of

The University of Texas at Austin

in Partial Fulfillment

of the Requirements

for the Degree of

Doctor of Philosophy

The University of Texas at Austin

May 2012

Acknowledgements

I would like to thank my supervisor Professor Ofodike Ezekoye for his guidance. His patience and intelligence were a tremendous help throughout the completion of this dissertation. Dr. Joseph Koo deserves thanks for his support and encouragement throughout my studies. I thank Dr. Marc Nyden for teaching me about reactive molecular dynamics and giving me an opportunity to perform research at NIST in the summer of 2009. Professor Greg Rodin gave many helpful suggestions at our weekly ablation group meetings. Professor John Howell provided me with my first research opportunity as an undergraduate and has taught me many things about heat transfer in general and radiation in particular.

I would also like to acknowledge my fellow graduate students for helping me with various problems. Special thanks are in order for Dr. Rochan Upadhyay for helping me to understand population balance equations and their solution, Dr. Omar Lopez for his willingness to assist me with computational issues, Dr. Uday Godse for our discussions on molecular dynamics, Dr. Craig Weinschenk for his friendship and support, and Kristopher Overholt for sharing his expertise in fire research. I also thank Reed Anzalone, Ben Barr, and Mikko Ponkala for their assistance on various problems.

Above all I would like to thank my family—especially my parents, Joe and Sudy, for their love and support.

Modeling and Simulation of Linear Thermoplastic Thermal Degradation

Publication No._____

Morgan Chase Bruns, Ph.D.

The University of Texas at Austin, 2012

Supervisor: Ofodike A. Ezekoye

Thermal degradation of linear thermoplastics is modeled at several scales. High-density polyethylene (HDPE) is chosen as an example material. The relevant experimental data is surveyed. At the molecular scale, pyrolysis chemistry is studied with reactive molecular dynamics. Optimization is used to calibrate several pyrolysis mechanisms with thermogravimetric analysis (TGA) data. It is shown that molecular scale physics may be coupled to continuum scale transport equations through a population balance equation (PBE). A PBE solution method is presented and tested. This method has the advantage of preserving detailed information for the small species in the molecular weight distribution with minimal computational expense. The mass transport of these small species is modeled at the continuum scale with a bubble loss mechanism. This mechanism includes bubble nucleation, growth, and migration to the surface of the condensed phase. The bubble loss mechanism is combined with a random scission model

of pyrolysis to predict TGA data for HDPE. The modeling techniques developed at these three scales are used to model two applications of engineering interest with a combined pyrolysis and devolatilization PBE. The model assumes a chemically consistent form of the random scission pyrolysis mechanism and an average, parameterized form of the bubble loss mechanism. This model is used to predict the piloted ignition of HDPE. Predictions of the ignition times are reasonable but the model over predicts the ignition temperature. This discrepancy between model and data is attributed to surface oxidation reactions. The second application is the prediction of differential scanning calorimetry (DSC) data for HDPE. The model provides detailed information on the energy absorption of the thermally degrading sample, but the literature data is too variable to validate the model.

Table of Contents

List of Tables

List of Figures

1: Introduction

1.1 Motivation and Background

The development of synthetic polymeric materials has solved many technological problems. Unfortunately, the proliferation of polymers has introduced several difficulties. Chief among these issues is the flammability and reuse of these materials. Both flammability and reuse depend strongly on the physics of thermal degradation.

Synthetic polymers greatly increase the fire load of commercial and residential buildings. In the United States alone, approximately 20,000 people are injured in house fires per year (Nelson, 2000). To mitigate this problem, the fire research community has sought to implement improvements in building design, sprinkler systems, and firefighting tactics. Rather than reacting to the fire, a more proactive approach is to use engineering and chemistry-based solutions (e.g., fire retardants) to prevent fires by reducing material flammability. Research in material flammability seeks to develop innovative, cost effective, and fire safe materials for consumer products. The development of these materials is slow and expensive because of the lack of small-scale tools for predicting large-scale flammability performance. Simulations are ideal for designing low flammability materials. They allow the researcher to identify critical flammability characteristics with minimal experimental data. Unfortunately, much of the chemistry and physics underlying material flammability is insufficiently understood at both the

macroscopic and microscopic scales. The models that do exist are often unphysical and poorly validated.

Polymers account for 7-8% of domestic waste (Bockhorn et al., 1999). Around 32-37% of this polymeric waste is polyethylene (Conesa et al., 1996). Because of the large chemical energy (~18,000-38,000 kcal/kg) stored in plastic waste, incineration is one practical method of disposal (Hernandez et al., 2005). Another alternative is feedstock recycling to produce valuable chemicals such as ethane, propene, styrene, etc. These materials can be used to reproduce polymers, as refuse-derived fuels, or in other applications. Design of pyrolysis reactors requires knowledge of the chemical mechanism, reaction rates, and mass loss physics. Careful design is needed to avoid production of toxic and environmentally harmful chemicals. As in designing fire resistant materials, simulation is a valuable tool for improving pyrolysis processing facilities.

The purpose of this dissertation is to explore improved modeling tools for thermal degradation. The scope is limited to linear thermoplastics, and high-density polyethylene (HDPE) is selected as the principle test case for validation. One of the primary reasons for focusing on HDPE is the large amount of experimental data available. Three experiments in particular prove useful for understanding thermal degradation: thermogravimetric analysis (TGA), differential scanning calorimetry (DSC), and evolved gas analysis (EGA). Although there is a large amount of data, thermal degradation experiments are complex and not sufficiently described by current physical models. For

this reason, progress in understanding the thermal degradation of polymers will require rational, physically-sound models of the underlying processes.

The physical complexity of these experiments requires detailed modeling for accurate data reduction. Throughout the remainder of this dissertation, the physics of thermal degradation will be discussed in the context of several length scales. At the largest length scale relevant to engineering applications, continuum mechanics is the appropriate tool for predicting the response of a system to a large thermal load. At small length scales, the physics are controlled by the quantum mechanics of the chemically reacting molecules. *Ab initio* treatments of complex condensed phase reactions are computationally intractable. One promising alternative is reactive molecular dynamics (RMD). In RMD, a collection of molecules is directly simulated by solving the classical equations of motion on a reactive force field. While RMD can be used to identify elementary pyrolysis reactions and estimate their rates, new methods are needed to make use of this information for the large length scales of material flammability scenarios. The necessity of a third modeling length scale arises from the great disparity between the continuum and molecular length scales.

In this chapter, HDPE is discussed in terms of its structure and its properties that are relevant in thermal degradation. The chapter is concluded with a broad overview of the remainder of the dissertation.

1.2 HIGH-DENSITY POLYETHYLENE

High-density polyethylene (HDPE) has been chosen as an example material because of its simplicity, its widespread use, and because of the availability of experimental data. The standard definition for HDPE is a polyethylene with a density greater than around 0.94 g/cc (Cullis and Hirschler, 1981). In addition to being compositionally simple (containing only carbons and hydrogen), HDPE is structurally simple having a very low degree of branching. In its solid phase, HDPE is semi-crystalline, but the melt phase is amorphous. Since the melt temperature of HDPE (~120°C) is much lower than the temperatures at which significant pyrolysis occurs (~400°C), the material of interest is an amorphous fluid.

The bulk behavior of a material is controlled by its microscale character. For the case of polymers, the microscale can be characterized by its atomic composition and structure. The structural complexity of polymeric systems results in many modeling difficulties. The mathematical treatment of such systems depends upon the degree of networking. On one end of the spectrum are heavily cross-linked thermosets. Elastomers represent an intermediate degree of networking. Finally, thermoplastics have no, or very few, cross-links. Because of this, it is possible to model a thermoplastic system as a collection of distinguishable molecules. Within the class of thermoplastics there is a distinction to be made between branched and linear polymers.

Polyethylene is composed solely of hydrogen and carbon atoms. For all polyethylenes the dominant structural group is the backbone unit ($-CH_2-$). The ends of the

chains are either methyls (CH_3-R) or allyls (H_2C=CH-CH_2-R). Another structural feature is the branch point at which a chain branches off of a typically much longer chain. Due to this chemical simplicity, the pyrolysis gas is composed of a relatively small number of components.

For various HDPEs, the degree of branching can vary, but it is generally small. For example, Balta Calleja and Rueda (1974) measured the degree of branching (DoB) for several commercial polyethylenes using IR analysis. The DoB is equivalent to the probability (%) that a backbone carbon atom has a branch attached to it. As is shown in Figure 1.1, the DoB is strongly correlated to the density of the material. This data indicates that the average DoB for HDPE is around 0.97. For this reason, HDPE will be treated as a purely linear thermoplastic. One caveat should be mentioned. It is observed at intermediate temperatures in the range of $200 - 390°C$, that HDPE has a tendency to accumulate long chain branches (Kuroki et al., 1982). Therefore, if the system is held at an elevated temperature for a significant amount of time before the onset of pyrolysis, it is no longer accurate to describe it as a purely linear polymer.

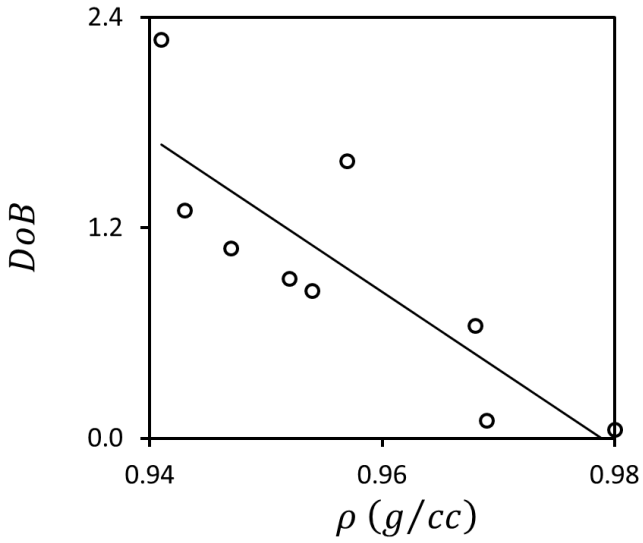

Figure 1.1: Degree of branching as a function of density.

Molecule size is another important aspect of the microscale description. Because polymers are composed of extremely large molecules, some of the physics will be independent of the molecules' sizes. That is, in a large chain molecule, events at one end of a chain will not significantly influence what happens at the other end of the chain. However, many material properties are strongly correlated to the average size of the chains. The size of a polymer chain is typically quantified in terms of the numbers of repeat units (monomers). A convenient measure of size for linear polyethylene molecules is the number of carbon atoms in the chain typically referred to as the carbon number.

Any given HDPE sample will be composed of a collection of chains of various lengths. The sample is therefore conveniently characterized by the molecular weight distribution (MWD). For many properties, it not necessary to know the full MWD, and several moments of the distribution are sufficient. For instance, the melt viscosity of

thermoplastics is a strongly correlated to the weight average molecular weight of the sample (Berry and Fox, 1968).

Different polymers have different MWDs, and the shape of the MWD is dependent largely upon the process by which the polymer was made. Polymers may be classified as being either step-growth or chain-growth polymers. This classification is similar to the distinction between condensation and addition polymers (Flory, 1953). Condensation (or step-growth) polymerization involves the combination of reactant polymers of all possible sizes. Examples of condensation polymers are polyesters, polyamides, and cellulose. By contrast, addition (or chain-growth) polymerization proceeds by the addition of monomers to active chains (e.g., free radicals) of various lengths. All vinyl polymers such as HDPE are addition polymers. Addition polymers tend to have much narrower MWDs than condensation polymers.

For condensation polymers, if it is assumed that all of the functional groups are equally reactive, then the MWD is the "most probable", or Schulz-Flory, distribution (Flory, 1953). It has been suggested by Peebles (1971) that the Schulz-Flory is also applicable to addition polymers in certain special cases and to systems that have undergone some degree of random scission. However, from looking at actual MWD data for HDPE, it does not appear that this is the case. Sezgi et al. (1998) measured the MWD for HDPE using high pressure liquid chromatography (HPLC) and gel permeation chromatography (GPC). Their data is plotted as the solid line in Figure 1.2. The number average MW of the experimentally measured distribution is 542 kg/mol. Choosing a

Schulz-Flory distribution with the same number average MW does not match the data. Flory (1940) reasoned that the MWD of addition polymers should be a Poisson distribution. His derivation assumed that there were no termination reactions. As is seen in Figure 1.2, the assumed Poisson distribution is too narrow. The Schulz-Flory and Poisson MWDs are both theoretical and seem to represent limiting cases for condensation and addition polymers. Neither of these is sufficient for modeling the MWD of real HDPE. It is therefore reasonable to assume a MWD that empirically matches the data. One such empirically reasonable function is the lognormal distribution. In Figure 1.2, a lognormal distribution is plotted that fairly well matches the MWD of Sezgi et al. (1998).

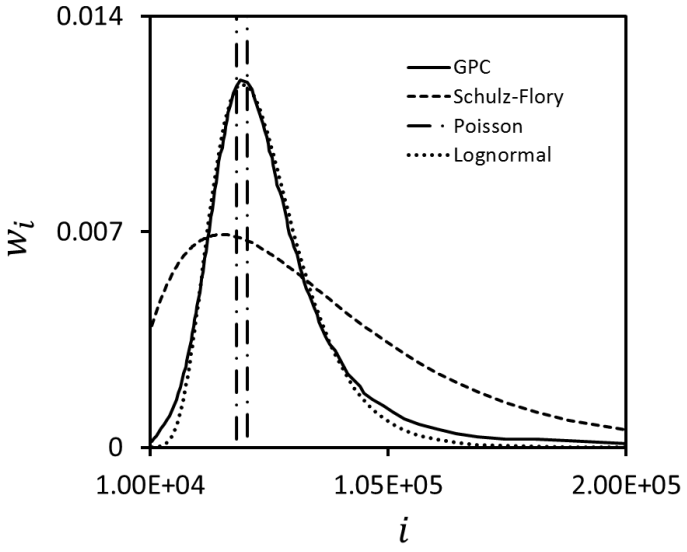

Figure 1.2: Molecular weight distributions for HDPE.

In summary, HDPE is a mostly linear polyethylene that can be modeled as being lognormal. In its solid state, HDPE is semi-crystalline, but since significant pyrolysis is

only observed at temperatures much higher than the melting temperature, the material of interest will be an amorphous liquid.

1.3 OUTLINE OF THE DISSERTATION

It is clear from the preceding discussion that much progress is needed before the details of the thermal degradation of thermoplastics can be predicted reliably. The purpose of this dissertation is to help lay the foundations upon which progress may be made. To this end, the modeling efforts were directed at several fronts. The second chapter addresses experimental data and proposes a multi-scale modeling framework for approaching thermal degradation problems. Chapter 3 focuses on pyrolysis chemistry. A survey of pyrolysis mechanisms is provided followed by the application of several methods for determining the corresponding rate constants. Initiation reactions are approximated qualitatively by gas phase pyrolysis reactions, and quantitatively by RMD. Kinetic parameters for three commonly used pyrolysis mechanisms are calibrated using optimization with TGA data. The fourth chapter presents and evaluates a numerical method for solving the kinetic equations for pyrolysis mechanisms. A bubbling loss model is derived in Chapter 5. This model is coupled with a simple pyrolysis model to predict isothermal TGA. The sixth chapter applies the loss and pyrolysis models of the previous two chapters to the prediction of piloted ignition and DSC for HDPE. Chapter 7 reviews the conclusions that were made and provides suggestions for future work.

2: Data and Modeling

Reliable modeling requires experimental data for calibration and validation. Conversely, interpreting experiments requires accurate models for data reduction. For these reasons, the relevant data and modeling tools for polymer thermal degradation are discussed in this chapter. Three thermal degradation experiments are described. This discussion will include a description of the experimental setup, an analysis of difficulties in interpreting the resultant data, and a brief survey of available literature data for HDPE. This information will provide a basis for subsequent model calibration and validation. In addition to this survey of literature data, observations were made of thermally degrading HDPE. The second part of this chapter presents the equations for modeling thermal degradation at three different length scales. These equations are presented in fairly general forms, and they will be referred to in the subsequent model development.

2.1 Thermal Degradation Experiments and Data

There is a significant amount of literature data relevant to the thermal degradation behavior of HDPE. In this section, three of the most common experiments are discussed and some of the associated literature data is presented. The data presented is not comprehensive, but it is meant to provide a validation base for subsequent modeling. The most detailed discussion is devoted to thermogravimetric analysis (TGA) since this is the most common of the experiments used to characterize the thermal degradation behavior of polymers. A fourth experiment that might be useful for measuring condensed phase

changes in degrading thermoplastics is gel permeation chromatography (GPC). GPC was used by Sezgi et al. (1998) to determine the MWD of an HDPE sample at several points in the thermal degradation process. Because of the relative scarcity of data, GPC will not be included in the following discussion.

2.1.1 Thermogravimetric Analysis

An obvious consequence of pyrolysis is mass loss. The mass loss rate of a pyrolyzing thermoplastic is easily measured. In thermogravimetric analysis (TGA), a small sample on the order of several milligrams is heated inside a furnace according to a prescribed temperature program, $T(t)$, and the normalized mass of the sample, $w(t) \equiv m(t)/m(t=0)$, is recorded continuously as a function of time. A diagram of a TGA apparatus and dynamic results for HDPE (Conesa et al., 1996) are shown in Figure 2.1. The heat input from the furnace, Q, is controlled based on input from a thermocouple under the sample to achieve the desired temperature program. In order to prevent oxidation, the furnace is usually purged with an inert gas such as nitrogen. Typical purge gas flow rates range from 60-150 cc/min (Conesa et al., 1996; Cozzani et al., 1995).

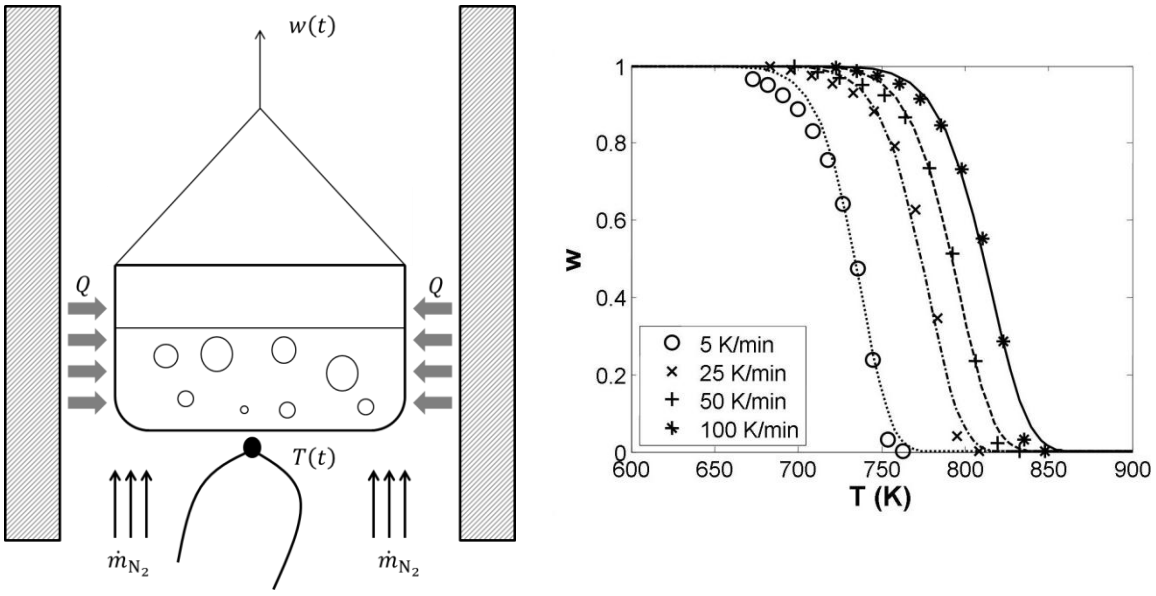

(a) (b)

Figure 2.1: Typical TGA setup (a) and dynamic data from Conesa et al., 1996 (b).

The fundamental assumption of TGA is that the sample is small enough so that heat and mass transfer effects within the condensed phase can be neglected. A typical sample pan diameter is on the order of 5 mm (Conesa et al., 1996). Cozzani et al. (1995) estimated a Biot number of 10^{-2} for their TGA experiments indicating that the sample may be thermally lumped. With respect to mass transfer, it seems less likely that the assumption of a spatially lumped sample is valid since the mass diffusivity of small alkanes in HDPE is relatively small, ~10^{-7} m^2/s (von Meerwall et al., 1999). However, as is discussed later, the loss from thermally degrading HDPE is controlled by a bubbling mechanism which tends to stir the melt thereby decreasing global concentration gradients.

The most common TGA temperature programs are either constant temperature or constant heating. Heating rates range from 1-100 K/s, although faster experiments are possible. The mass resolution is typically $\sim 0.1 - 1$ μg (Speyer, 1994) which is roughly 0.01% of the sample mass. The accuracy of TGA depends primarily on the accuracy of the temperature measurement which requires careful calibration. Extensive reviews of the TGA methodology are found in Brown (2001) and Speyer (1994).

There are several typical uses of TGA data. At its coarsest level, TGA data is useful for identifying the approximate temperature at which a reaction takes place. This is usually done by looking at the mass loss rate as a function of temperature for a constant heating rate experiment. Time derivative plots of TGA data are often called derivative or differential thermogravimetry (DTG), but DTG is not a separate experiment. A reaction temperature is typically identified with the location of a peak in the differential TGA plot. Some materials will show several peaks corresponding to multiple reactions. Even though these peaks are said to correspond to reactions, for polymeric materials they are generally associated with some complex network of reactions.

The primary use of TGA considered in this dissertation is for help in parameterizing models of thermal degradation. Predicting the mass loss rate is critical for modeling ignition and flame spread in fire and recession rate in thermochemical ablation. In such applications, the mass loss rate is usually modeled as an Arrhenius process (Quintiere, 2006; Amar et al., 2007). These models vary in complexity, but the most basic form is a first-order Arrhenius rate

$$\frac{dw}{dt} = -Aw \exp\left(-\frac{E}{RT(t)}\right) \tag{2.1}$$

Models such as Equation (2.1) can be fit with experimental data as is demonstrated in Figure 2.1 (b). There is a large body of literature on methods for fitting TGA data (Ozawa (1965); Vyazovkin (1996); Ferriol et al. (2003)). Unfortunately, there is no clear physical interpretation to Equation (2.1) as applied to thermal degradation. Lyon (2000) has demonstrated that the activation energy, E, can be approximated as the sum of the energy required to heat the sample to $T(t)$ plus the enthalpies of fusion, bond dissociation, and vaporization. However, this interpretation leaves the pre-exponential, A, undetermined, and the enthalpies of bond dissociation and vaporization must be based on assumptions of the composition of the pyrolysis gas. Furthermore, most applications involve heating conditions that are much more extreme than are attainable in the laboratory. In order to make reliable predictions in such extreme conditions, models based on real physical processes need to be developed.

One difficulty in fitting Arrhenius type models for TGA is the kinetic compensation effect. It has been observed (Ceamanos et al., 2002) that there is a large variance in the Arrhenius parameters, A and E, reported in the literature for TGA of HDPE. Furthermore, these parameters are found to lie along a line in a plot of $\log A$ versus E. This observation is a consequence of the trade-off between the pre-exponential and the activation energy in determining the kinetic rate. As a consequence of the kinetic compensation effect, different methods of TGA will result in different kinetic parameters to describe the pyrolysis behavior of the same material. In scenarios outside of TGA

operating conditions, these different kinetic parameters might result in significantly different predictions.

Even aside from the kinetic compensation effect there are a number of other factors that complicate the interpretation of TGA data. Not only does the literature report vastly different Arrhenius parameters, but there is also a significant difference in the reported TGA curves themselves. An example of this is given in Figure 2.2 in which isothermal TGA data for HDPE is plotted from two sets of authors (Conesa et al., 1996; Wallis and Bhatia, 2006) at several temperatures. There are several possible explanations for the disparity in these data sets. One possibility is the difference in the samples. Conesa et al. used 13 mg samples with unspecified form. Wallis and Bhatia used 10 mg samples of HDPE "fluff". The increased surface area could lead to faster mass loss rates in the Wallis and Bhatia data. Additionally, there could be significant differences in the molecular weight or degree of branching in the HDPEs used. The most likely explanation for the discrepancy in mass loss curves is the relatively slow heating rates used by Wallis and Bhatia to reach the experimental temperatures.

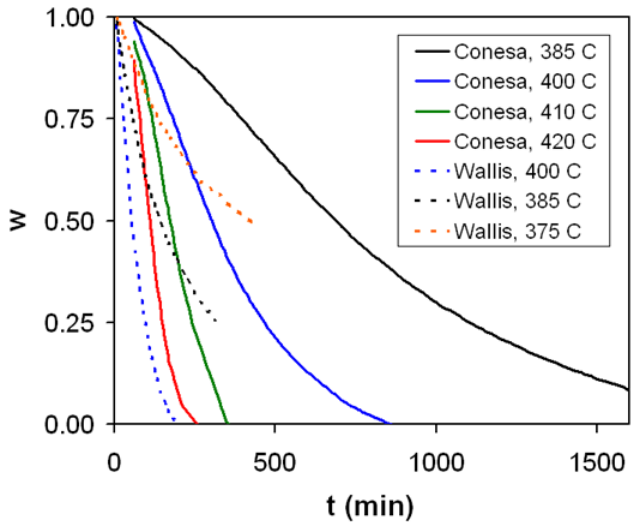

Figure 2.2: Experimental data for isothermal TGA of HDPE.

The reported data for dynamic (non-isothermal) TGA shows similar scatter. This is demonstrated in Figure 2.3 where data is compiled from three authors: Ceamanos et al. (2002) at heating rates of 5, 12, 25, and 50 K/min; Conesa et al. (1996) at heating rates of 5, 25, 50, and 100 K/min; and Cozzani et al. (1995) at a heating rate of 20 K/min. The data is presented in the form of an Arrhenius plot. The slopes of the linear fits are approximations to $-E/R$ and the intercepts are approximations to $\log A$. It is clear that the three different data sets indicate different kinetic pairs. Furthermore, within the data set of Conesa et al., it appears that different subsets of this data indicate significantly different kinetic parameters.

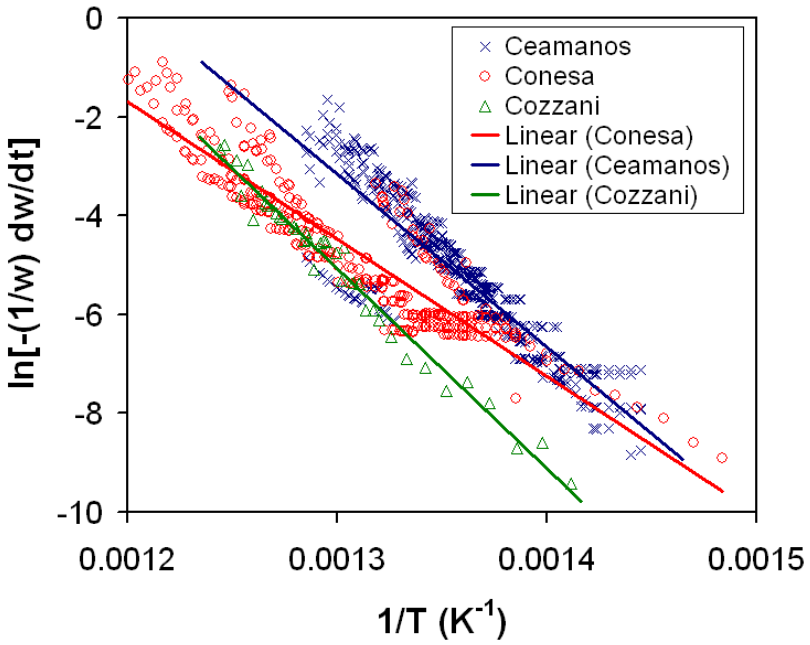

Figure 2.3: Arrhenius plot of dynamic TGA data for HDPE.

One conclusion of the preceding discussion is that the standard application of TGA is not sufficient for characterizing mass loss in thermally degrading polymers. In the next section, another relevant experiment is analyzed.

2.1.2 Differential Scanning Calorimetry

Differential scanning calorimetry (DSC) has a similar setup to TGA except that the quantity being measured is the heat absorbed by the degrading sample. Applications of DSC include the quantification of a variety of thermal events in condensed phase materials (Brown, 2001). Examples are glass transitions, crystallization, melting, and thermal degradation. Another application of DSC is to determine specific heats (O'Neill,

1966). In the domain or polymer degradation, DSC has been used to measure the heat of decomposition of various polymers (Frederick and Mentzer, 1975; Stoliarov, 2008).

A similar experiment is differential thermal analysis (DTA). Whereas DSC relies on heat input differences, DTA measures temperature differences. Generally, DTA requires a simpler apparatus, but the measured quantity is less informative. For this reason, attention will be directed towards DSC experiments.

A typical DSC apparatus is sketched in Figure 2.4. Two cells are heated in a furnace. In the sample cell is a pan containing a small amount of the material of interest. In the reference cell is an identical pan containing a small amount of some reference material. Ideally, the reference material is chosen to have a similar heat capacity to the sample without undergoing any thermal events. Both cells are heated so that their temperatures follow a prescribed temperature program, $T(t)$. Almost all DSC experiments use a constant heating rate program so that $dT/dt = \beta$ is a constant. The heat transfer into the sample and reference cells are measured as $\dot{Q}_s(t)$ and $\dot{Q}_r(t)$. The raw output from a DSC experiment is the difference in the two heat transfer rates, $\Delta\dot{Q}_I(t) \equiv \dot{Q}_{I,s} - \dot{Q}_{I,r}$. Several DSC curves for polyethylene are plotted in Figure 2.5(a) where $\Delta\dot{q} \equiv \Delta\dot{Q}_I/m(t=0)$. The data were taken from Conesa et al. (1996), Cozzani et al. (1995), Jinno et al. (2004), and Straka and Nahunkova (2004). Raw data from different heating rates should not be compared and so the data scaled by heating rate is plotted in Figure 2.5(b) where $\Delta c^* \equiv \Delta\dot{q}/\beta$.

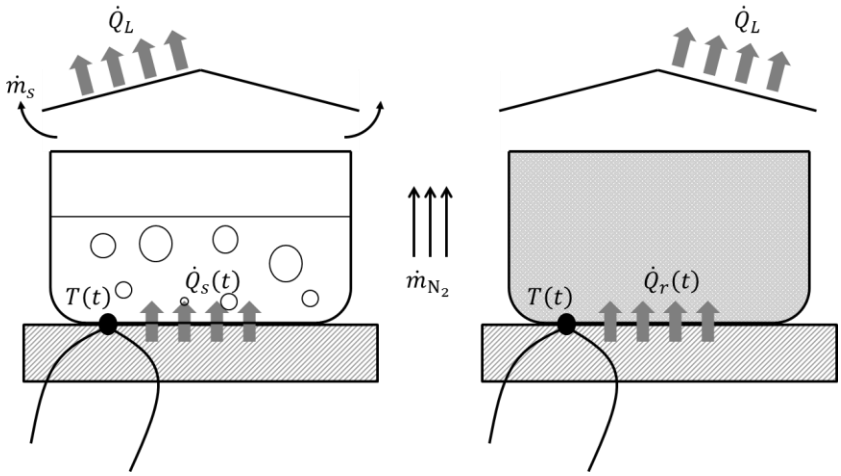

Figure 2.4: Typical DSC apparatus.

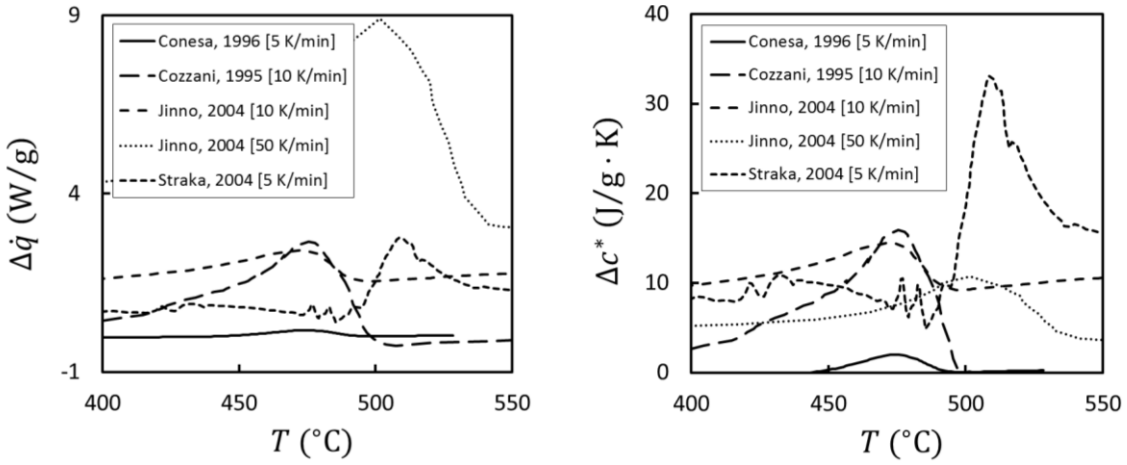

(a) (b)

Figure 2.5: DSC data for polyethylene normalized by mass (a) and by mass and heating rate (b).

The purpose of the reference cell is to isolate thermal events taking place in the sample material. Ideally, the heat losses and storage rates in both cells would be equal so that the DSC signal is only non-zero when a sample specific thermal event takes place.

The heat loss differences can be minimized by covering the pans so that the cell geometries and emissivities are identical. If the sample is thermally degrading, the pan covers should be pierced (Brown, 2001) or bent (Stoliarov, 2008) so that the pyrolysis gases can easily escape. The furnace is purged with an inert gas at flow rates similar to TGA (e.g., 30 cc/min (Jinno et al., 2004); 35 cc/min (Stoliarov, 2008). For thermally degrading samples, it is not possible to find a reference material that always has the same heat capacity as the sample without also undergoing mass loss. Because of this, there will always be some difference between the DSC output and the energy rate associated with the thermal events.

To better understand the difference between the DSC output and the quantity of interest, it is helpful to examine the experiment analytically. Neglecting any spatial variations, conservation of energy equations for the reference and sample cells are

$$(C_r + C_{PAN})\beta = \dot{Q}_{I,r} - \dot{Q}_{L,r}, \tag{2.2a}$$

$$(C_s + C_{PAN})\beta = \dot{Q}_{I,s} - \dot{Q}_{L,s} - \dot{Q}_D - \dot{m}_s RT/\widetilde{M}_s^g, \tag{2.2b}$$

where C_x are heat capacities, $\dot{Q}_{L,x}$ are the heat loss rates from the cells, $\dot{Q}_D$ is the energy absorption rate due to degradation, $\dot{m}_s$ is the mass loss rate from the sample cell, and $\widetilde{M}_s^g$ is the mass average molecular weight of the gases exiting the sample cell. Solving Equations (2.2a) and (2.2b) for the heat absorption rate, and assuming that $\dot{m}_s$ is relatively small, results in

$$\dot{Q}_D = \Delta\dot{Q}_I + \left((C_r - C_s)\beta - \Delta\dot{Q}_L\right), \tag{2.3}$$

where $\Delta\dot{Q}_L \equiv \dot{Q}_{L,s} - \dot{Q}_{L,r}$. Equation (2.3) shows that some correction must be applied to the DSC output, $\Delta\dot{Q}_I$, in order to compute the total heat of decomposition. Note that by the sign conventions chosen, $\dot{Q}_D > 0$ and $\Delta\dot{Q}_I > 0$ for endothermic processes such as pyrolysis and devolatilization. The heat of decomposition includes the heat of pyrolysis and the heat of devolatilization since these two processes cannot be distinguished in DSC. The heat of decomposition is sometimes referred to as the heat of volatilization (Frederick and Mentzer, 1975). A similar quantity is the heat of gasification which is the energy required to heat up, pyrolyze, and devolatilize a material (Lyon, 2000). An obvious consequence of Equation (2.3) is that the error is smaller for slow heating rates since all of the correction terms decrease with decreasing β.

The primary difficulty in analyzing DSC data is estimating these correction terms. The first term in parentheses in Equation (2.3), $C_r\beta$, is easily computed from the mass and specific heat capacity of the reference material. If no reference material is used, then $C_r = 0$. Ideally, the heat loss differential, $\Delta\dot{Q}_L$, should equal zero. The validity of this assumption can be tested by running a DSC experiment with two empty pans—in this scenario, $\Delta\dot{Q}_I = \Delta\dot{Q}_L$. Stoliarov (2008) ran empty pan DSC experiments with and found that the heat loss differential was not zero and varied "significantly" in different runs. Even so, an estimate of the differential heat loss can be made using empty pan experiments.

The heat capacity of the sample cell has a strong dependence on the mass loss behavior of the sample material. It is therefore advisable to perform coupled TGA/DSC

(Jinna et al., 2004). In the absence of mass loss rate information, simplifying assumptions must be made to obtain an estimate of the heat of degradation. The simplest approach is to establish a baseline for the endothermic peak. This can be done graphically by drawing a line under the peak and integrating between the peak and the line (Frederick and Mentzer, 1975).

From Figure 2.5 it is clear that there is a large variety in the reported DSC curves for polyethylene decomposition. This variation is only partially explained by the error terms. As with TGA, differences in the material might account for some of these differences. The other possibility is that there are significant differences in the accuracy and reliability of various DSC apparatuses. Despite these problems, DSC and TGA provide some information about global mass and energy evolution in a thermally lumped sample of degrading material. More modeling work is needed to make this global information useful. Before discussing modeling aspects, one final experiment is evaluated.

2.1.3 Evolved Gas Analysis

The final thermal degradation experiment to be considered is evolved gas analysis (EGA). The label EGA encompasses a broad range of technologies used to quantify the chemical composition of gases. The chemical composition of pyrolysis gas is important in flammability applications for predicting parameters such as the heat of combustion evolved gas and toxicity. In recycling applications, the pyrolysis gas composition in and

of itself is an important quantity of interest. Furthermore, gas composition data is necessary for the validation of detailed models of thermal degradation.

All EGA experiments have at least two components: a thermal analysis technique (usually thermogravimetry) and a gas analysis technique. This setup is diagramed in Figure 2.6. The pyrolysis process can be carried out in a variety of different devices, but it is most prudent to pyrolyze the sample with a thermal analysis technique that provides useful information. In fact some the first studies of evolved gases were largely motivated by a desire to better understand data from DTA. Ayres and Bens (1961) used gas thermal conductivity cells to detect the presence of evolved gases flowing out of a DTA apparatus. If a DTA peak was observed without a simultaneous peak from the gas detector, then it could be concluded that a phase transition, rather than a decomposition, was taking place in the material.

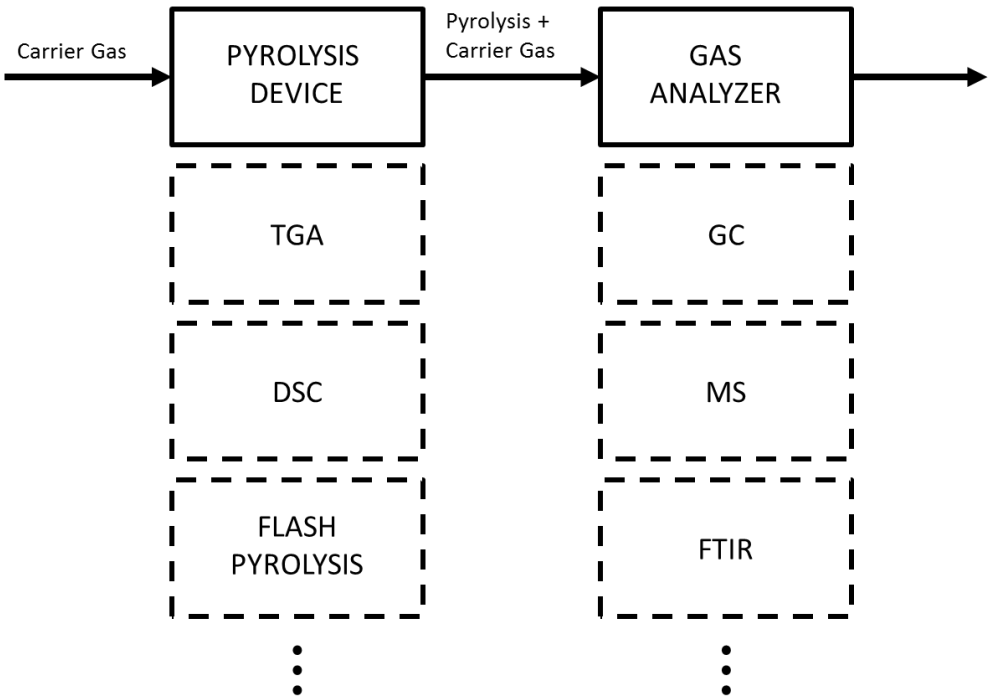

Figure 2.6: Setup for evolved gas analysis (EGA) showing several different alternatives for pyrolysis devices and gas analyzers.

There are many approaches used for gas analysis. Wendlandt (1986) lists 17 different alternatives. Several inherent difficulties in gas analysis should be mentioned. First, the gas analyzer will generally be calibrated to detect only a limited range of species. One possible solution is to use multiple devices for analyzing the pyrolysis gas. Second, the evolved species will continue to react after they have left the condensed phase but before they have entered the gas analyzer. The extent of these gas phase reactions can be limited by reducing the distance between the pyrolysis device and the gas analyzer or by increasing the flow rate of the carrier gas. In some cases, it might be necessary to model the gas phase chemistry of the pyrolysis gas in order to properly

interpret EGA data—an example of this approach is found in Sezgi et al. (1998). Another difficulty inherent in EGA, is condensation of the evolved gases as they are transported from the pyrolysis device to the gas analyzer. The condensation of pyrolysis gases can be limited by insulating or heating the pyrolysis gas outlet tube. None of these three difficulties are insurmountable, but they do present a problem for the analysis of literature data since many of the relevant factors affecting EGA measurements are not reported.

There is a large amount of evolved gas data for HDPE in the literature. A thorough review of pyrolysis gas data is provided by Poutsma (2003). Poutsma concludes that more work is needed in calibrating the various EGA techniques before reliable quantitative data can be presented across the entire range of volatile products. In Figure 2.7, GC-MS data for HDPE pyrolysis gas are plotted. The data comes from Michal et al. (1976), Murata et al. (2004), Breen et al. (2000), Uddin et al. (1997), and Faravelli et al. (1999). It is clear from Figure 2.7 that there is a significant amount of uncertainty with regards to the composition of the pyrolysis gas of thermally degrading HDPE. The composition will depend on the heating conditions which are typically more complex than constant temperature scenarios. Progress depends on improved modeling.

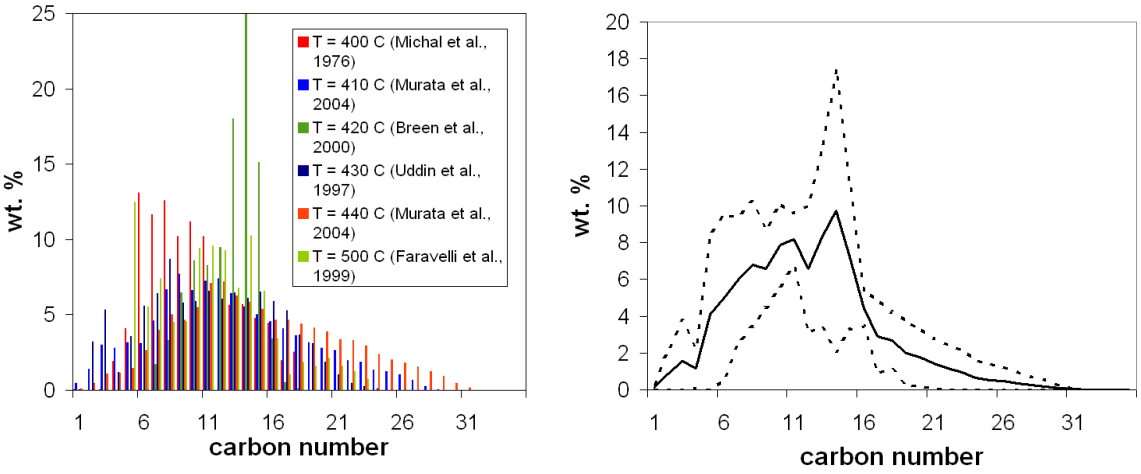

(a) (b)

Figure 2.7: (a) GC-MS data for HDPE pyrolysis gas. (b) Average and standard deviation of the same data.

2.1.4 Thermal Degradation Observations

Different polymers behave differently during thermal degradation. The most obvious example of this is the difference between charring thermosets such as wood and carbon phenolic as compared to many thermoplastics which do not typically produce large amounts of char. It is also possible that the mechanism of thermal degradation depends on the environmental conditions such as the presence of oxygen or the temperature. For these reasons it is helpful to observe what happens when the material of interest, HDPE, is pyrolyzed. The simple experiment described below is similar to work done by Sakata et al. (1996).

A sample of HDPE pellets was pyrolyzed in a test tube. The sample temperature was maintained between 390–420ºC. Figure 2.8 shows the sample before it was melted

and then at three times after it began to pyrolyze. At time t_0, the melted portions are clear, but there are still significant regions of solid phase HDPE. It was observed that there were relatively large gas voids formed during this time period possibly due to gas accumulating under solid material. The next snapshot was taken two minutes later. At this point the noticeable features are (1) many more bubbles, (2) increased bubble velocity, (3) a yellowish tint to the melt, and (4) the formation of a bubble 'fizz' layer at the surface of the melt. The change in color is believed to be due to a significant change in average MW of the material. This hypothesis was further confirmed by examining the re-solidified material which was waxy and opaque. The final snapshot was taken four minutes after t_0 and seems to be qualitatively similar to the previous picture. In fact the only noticeable differences are a decreased sample height and a further darkening of color. The vast majority of bubbles seemed to form at the bottom of the test tube. The bubbles are uniformly distributed in space and are mostly the same size.

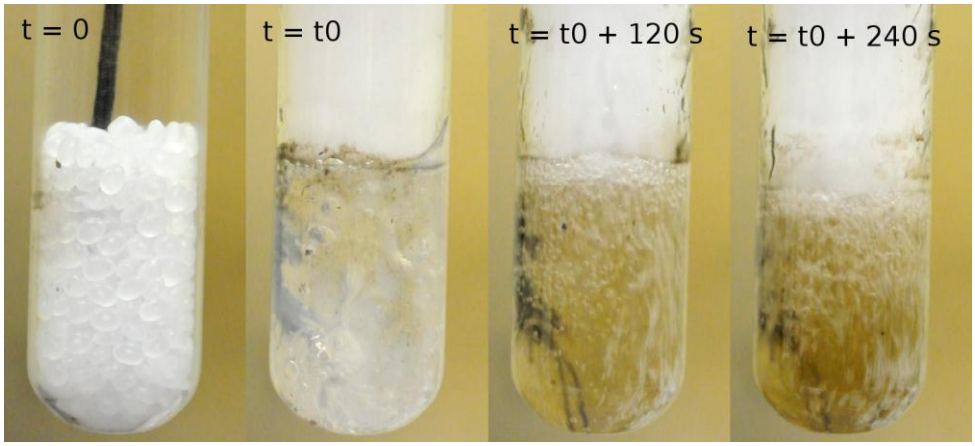

Figure 2.8: Pyrolysis of HDPE at $T \approx 400°C$.

The bubbles shown in Figure 2.8 are numerous and fast moving. In order to obtain data from this experimental setup, a high-speed camera was used to record the bubbling mass loss at 500 frames per second. The camera was a Kodak EktaPro 4540mx, and the setup is shown in Figure 2.9. The sample temperature was maintained at approximately 400°C, and images were analyzed at 380 s, 680 s, and 980 s after the onset of pyrolysis. The measured temperature versus experiment time is plotted in Figure 2.9(b). A sample image is shown in Figure 2.10.

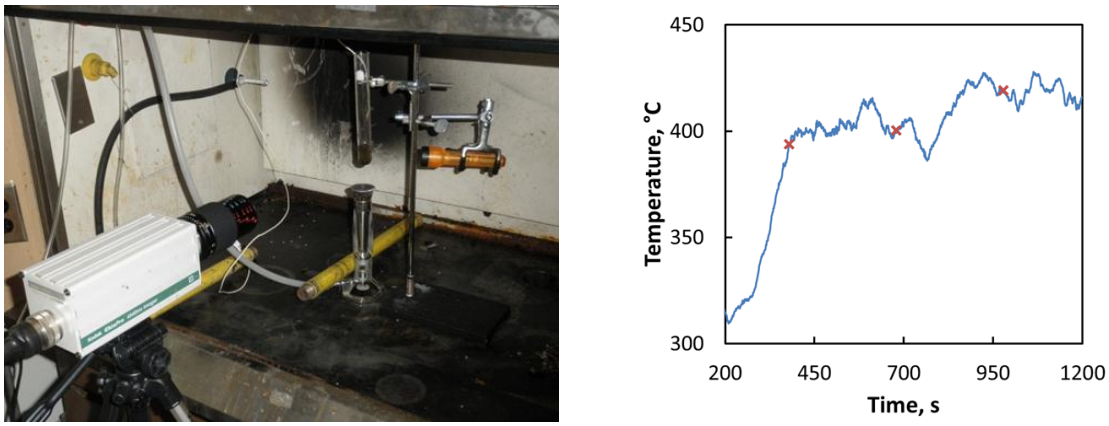

(a) (b)

Figure 2.9: Experimental setup for high speed HDPE pyrolysis observations (a) and time-temperature curve with 'x' markers for the times at which measurements were made (b).

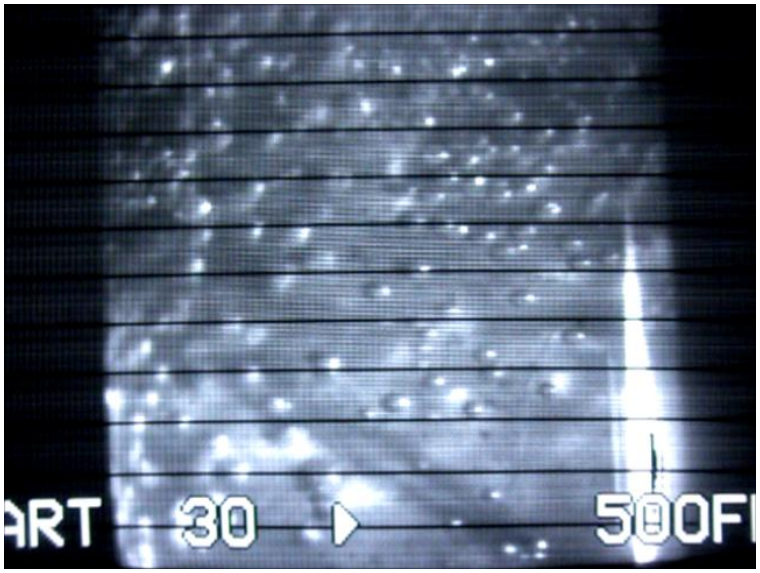

Figure 2.10: Example snapshot of bubble distribution in pyrolyzing HDPE at ~400°C.

From images such as Figure 2.10, approximate measurements can be made of bubble diameters. In Figure 2.11, the bubble number distribution (in terms of bubble diameter) is plotted for three different times. The average bubble diameter was seen to be around 0.7 mm which agrees HDPE pyrolysis bubble diameters found in the literature (Wichman, 1986). The average bubble diameters are plotted as a function of time in Figure 2.12. It was observed that bubble diameters decrease and the distribution narrows as pyrolysis proceeds.

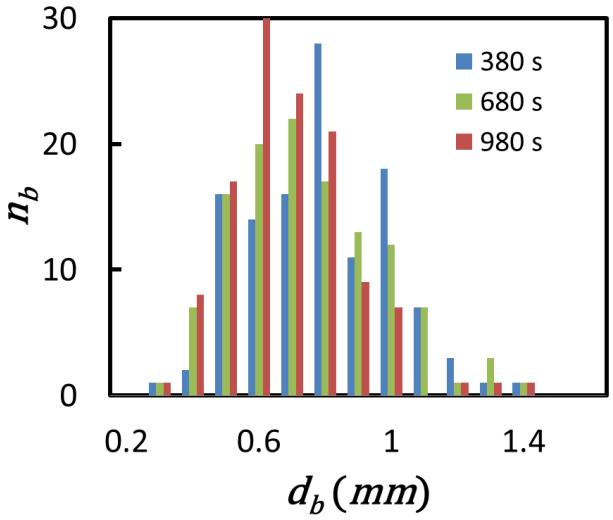

Figure 2.11: Bubble diameter histogram for HDPE pyrolysis at three different times.

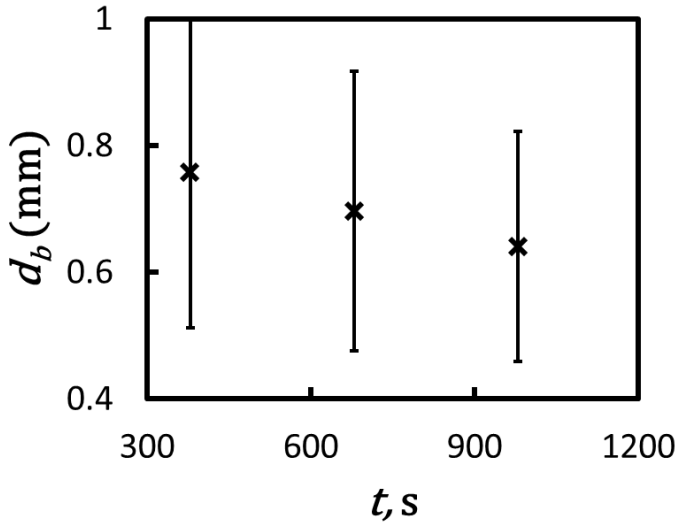

Figure 2.12: Average bubble diameter as a function of time in pyrolyzing HDPE.

Bubble velocities were also measured. This was somewhat more difficult since the bubbles did not tend to flow in perfectly straight lines. The bubble velocities averaged between 5-15 cm/s. It was observed that the bubble velocity initially increased and then

decreased as pyrolysis proceeds. This trend is evident in Figure 2.13. A possible explanation for this behavior is found by applying Stokes' law. Velocity is inversely proportional to viscosity and directly proportional to bubble diameter squared. Thus as the melt phase pyrolyzes and the viscosity decreases due to the decreasing MW of the polymer, the bubble should initially move faster. However, since the bubble diameters are seen to decrease with time, the velocity should ultimately decrease.

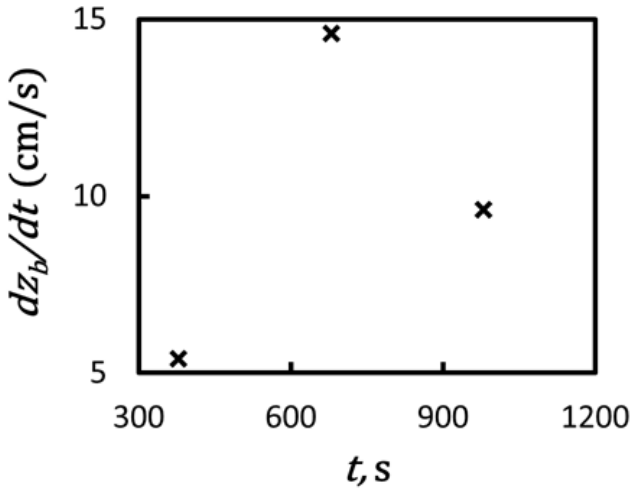

Figure 2.13: Average bubble velocities for HDPE as a function of time.

Other quantities of interest are bubble number density and the closely related nucleation rate. Neither of these quantities were measured because of limits in the resolution of the images. The most important observations of this simple experiment are that pyrolyzing HDPE vigorously bubbles and produces negligible char. Consequently, it is reasonable to assume that mass loss in vertically thick samples is dominated by bubble nucleation, growth, and buoyantly driven transport.

2.2 MODELING OF THERMOPLASTIC THERMAL DEGRADATION

Thermal degradation involves the conversion of a condensed phase material to pyrolysis gas and in many cases a carbonaceous char. The process of thermal degradation takes place over several length scales and multiple modeling domains. A schematic of a hypothetical thermal degradation system is provided in Figure 2.14. Gas phase physics has been relatively well-studied in the ablation and fire research communities. The condensed phase, however, is more difficult to model for several reasons. Many of the ideal gas approximations used in gas phase chemistry, thermodynamics, and transport are not valid in the condensed phase. Also, it is generally more difficult to experimentally study condensed phase phenomena.

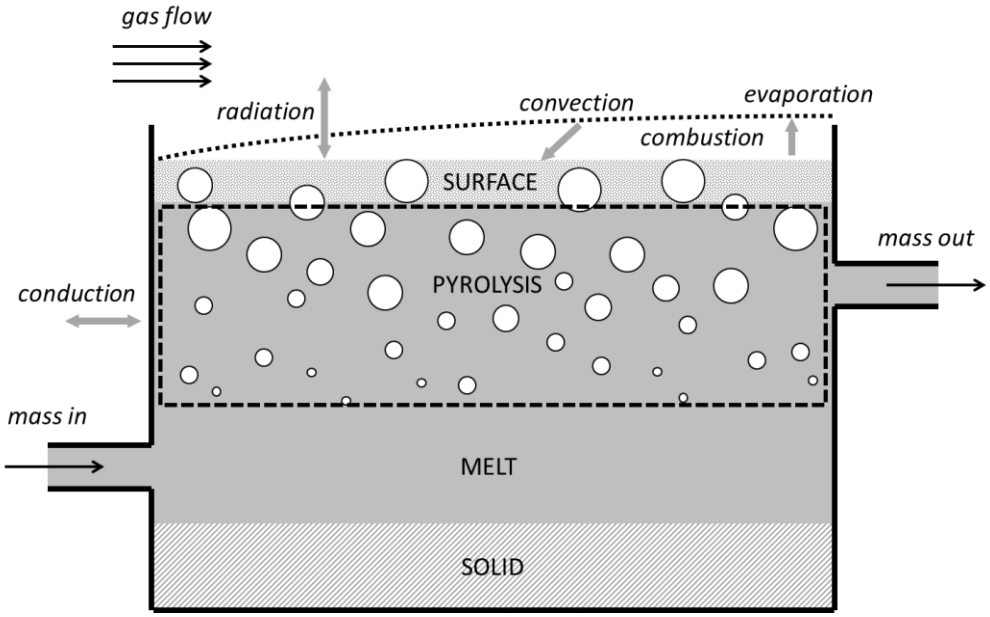

Figure 2.14: Engineering scale description of a hypothetical thermal degradation system. The pyrolysis zone is everything within the dashed line.

In Figure 2.14, the condensed phase is divided into four domains: solid, melt, pyrolysis, and surface. In the solid phase, the relevant physics are heat conduction and mass diffusion. Fluid mechanics becomes important in the melt phase. In the pyrolysis zone chemical reactions and bubble nucleation significantly alter the composition, temperature distribution, and flow field of the melt. The final condensed phase region is a thin surface layer in which gas phase species diffuse into and out of the melt phase. If the gas phase environment is air, surface oxidation becomes important. It is also possible that some char might develop in the pyrolysis zone and at the surface layer, but for HDPE char formation is minimal. The focus of this dissertation is on the pyrolysis zone.

The thermal degradation physics occurring in the pyrolysis zone can be described as follows. A linear polymeric system is composed of a large number of chemically similar but size-distributed macromolecules. Upon heating, the molecules will undergo pyrolysis reactions producing smaller molecules. These smaller molecules will diffuse and nucleate into bubbles. The bubbles are driven to the surface of the system by buoyant forces. Consequently, mass is lost from the system. The entire process is endothermic.

In this section, a modeling framework is proposed for the physics of the pyrolysis zone. At the *molecular scale*, the important questions involve pyrolysis chemistry. Specifically, what is the mechanism by which the long chain polymers form small volatile molecules? Once the proper mechanism is identified, the rate constants must be determined. Additionally, the physics of the molecular scale influences thermophysical material properties that control the bulk behavior of the system.

It is infeasible to treat a large sample of pyrolyzing HDPE with a molecular scale description, and so an intermediate layer of models is needed. The goal of a *mesoscale* analysis is to rationally reduce the complexity of the problem so that only the important molecular scale information is retained. Of primary importance in thermally degrading systems are the species population dynamics. The approach taken here is to assume that the polymer molecules can be modeled as a population of notional particles distributed according to their size. For the case of a pyrolyzing material, the local dynamics of this population are governed by a breakage and aggregation population balance equation.

The largest scale considered will be referred to as the *continuum scale*. At this scale, the governing equations are conservation of mass, momentum, and energy. The solution of these equations is a problem in the domain of numerical methods, but from the perspective of physics, the issue is primarily one of formulating the appropriate constitutive relations, estimating appropriate material properties, and modeling the physics of phase separation (i.e., bubble formation). In the remainder of this chapter, these three modeling domains are discussed in greater detail.

2.2.1 Continuum Scale

Ultimately, the modeling of real engineering systems requires a continuum scale description of the thermally degrading system. The pyrolysis zone is composed of a large number of species distributed between gas and melt phases. The presence of a significant gas phase (in the form of bubbles) is observed in many pyrolyzing thermoplastics such as HDPE. The ultimate goal of a continuum scale analysis is the prediction of heat and mass

fluxes across the boundary of the pyrolysis zone. These fluxes are then coupled to the other domains involved in the application. In order to determine these fluxes in a pyrolyzing thermoplastic, the multicomponent multiphase conservation equations are needed. The fluid dynamics of the melt phase is complicated by the vigorous bubbling present in the thermal degradation of HDPE. This bubbling, coupled with natural convection, tends to mix the fluid. In the following, it will therefore be assumed that the melt is well-mixed. It should be noted that detailed modeling of the fluid mechanics of the melt phase is difficult since polymer melts are non-Newtonian (Bird et al., 1987).

A schematic of an abstract pyrolysis zone control volume is shown in Figure 2.15. Since pyrolysis temperatures are typically much higher than melting temperatures, the presence of a solid phase will be neglected. The phase boundary, $I(t)$, corresponds to an abstract surface representing the sum of all bubble surfaces. The superscripts g and m refer to the gas and melt phases. For each conservation principle, there are integral equations for the gas phase, the melt phase, and the entire control volume. These equations are presented in their general integral form along with a differential form assuming some standard constitutive equations. The form of the equations is largely taken from Deen (1998) while the notation corresponds to Bird et al. (1960).

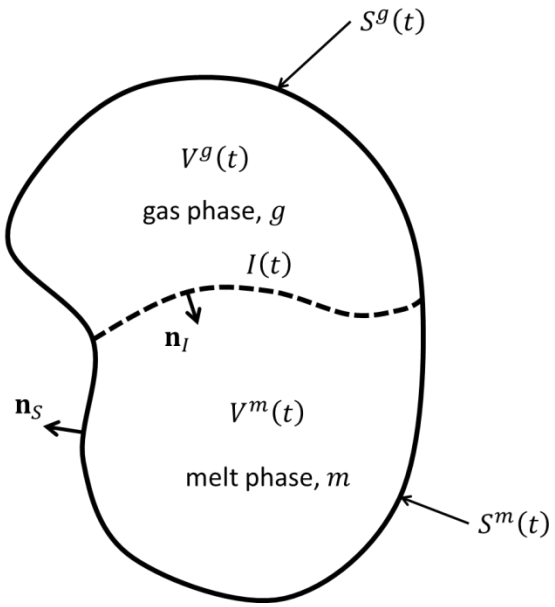

Figure 2.15: Characteristic control volume for an abstract pyrolysis zone.

The equations presented below are sufficient for describing the transport in the individual phases. However, a detailed analysis of the system will require modeling of the dynamics of the phase separation processes. In the pyrolysis zone, phase separation is due to gas phase bubble nucleation. The probability of a bubble nucleating at a particular point is proportional to the concentration of volatile species at that point. A detailed analysis would require modeling of the bubble surfaces, how they deform under the stresses of the flow field, and how they influence the flow field. Another difficulty is the accumulation of bubbles at a free surface. Because of these and other complexities, detailed multiphase modeling will not be considered. In Chapter 5, a simplified bubble model will be used to take into account some of the multiphase components of the

problem. The presentation of the conservation equations below is intended to provide a foundation for these analyses.

2.2.1.1 Conservation of Species Mass

Polymer systems are composed of an extremely large number of components. In general, it is infeasible to treat each of these components separately. The time rate of change of mass of species i in each phase is equal to the net flux across the phase and control volume boundaries plus the rate of production due to chemical reactions. The conservation of species mass in the gas and melt phases are written as

$$\frac{d}{dt}\int_{V^g}\rho_i dV = -\int_{S^g}[\mathbf{j}_i + \rho_i(\mathbf{v}-\mathbf{v}_S)]\cdot\mathbf{n}_S dS - \int_I [\mathbf{j}_i + \rho_i(\mathbf{v}-\mathbf{v}_I)]^g \cdot \mathbf{n}_I dS + \int_{V^g} r_i dV, \tag{2.4a}$$

$$\frac{d}{dt}\int_{V^m}\rho_i dV = -\int_{S^m}[\mathbf{j}_i + \rho_i(\mathbf{v}-\mathbf{v}_S)]\cdot\mathbf{n}_S dS + \int_I [\mathbf{j}_i + \rho_i(\mathbf{v}-\mathbf{v}_I)]^m \cdot \mathbf{n}_I dS + \int_{V^m} r_i dV, \tag{2.4b}$$

where ρ_i is the mass density of species i, $\mathbf{j}_i$ is the mass diffusion flux, $\mathbf{v}$ is the local mass average velocity, $\mathbf{v}_S$ and $\mathbf{v}_I$ are surface velocities, and r_i is the volumetric rate of mass production for species i. The mass diffusion velocities have the property that $\sum_i \mathbf{j}_i = 0$. At the melt-gas interface, assuming there are no surface reactions, conservation of mass is given by

$$[\mathbf{j}_i + \rho_i(\mathbf{v} - \mathbf{v}_I)]^g = [\mathbf{j}_i + \rho_i(\mathbf{v} - \mathbf{v}_I)]^m. \tag{2.5}$$

This relationship gives the surface velocity in terms of the diffusional velocities and densities at the interface. Summing Equations (2.4a) and (2.4b) and applying Equation (2.5) gives the continuity equation for species k for the entire control volume as

$$\frac{d}{dt}\int_V \rho_i dV = -\int_S [\mathbf{j}_i + \rho_i(\mathbf{v} - \mathbf{v}_S)] \cdot \mathbf{n}_S dS + \int_V r_i dV. \tag{2.6}$$

Finally, summing over all species gives the standard equation for conservation of total mass

$$\frac{d}{dt}\int_V \rho dV = -\int_S \rho(\mathbf{v} - \mathbf{v}_S) \cdot \mathbf{n}_S dS, \tag{2.7}$$

since $\rho \equiv \sum_i \rho_i$, $\sum_i r_i = 0$, and the diffusive velocities sum to zero.

Any application of these equations will require further information. The species production rates require a chemistry model which will depend upon the thermodynamic state of the system. If the control volume is large enough, there will be significant changes in the mass densities across the control volume, and it will be necessary to solve the differential form of the species mass conservation equations. The differential form for both the gas or melt phase is

$$\frac{\partial \rho_i}{\partial t} + \boldsymbol{\nabla} \cdot (\rho_i \mathbf{v}) = -\boldsymbol{\nabla} \cdot \mathbf{j}_i + r_i, \tag{2.8}$$

Equation (2.8) requires a constitutive equation for the diffusive flux.

Multicomponent diffusion in condensed phases is a difficult problem (Cussler, 1976). In most applications, the diffusional driving force is dominated by the species

concentration gradients. Even in this simplified case, the constitutive equation requires the specification of N^2 multicomponent diffusion coefficients. For $N > 2$, it is not usually possible to determine these coefficients. In low density gas phase diffusion, it is possible to equate the multicomponent diffusivities with their binary pair diffusivities. Diffusion in the melt phase is more difficult. For the special case of dilute mixtures, the diffusional flux constitutive equation simplifies to (Deen, 1998)

$$\mathbf{j}_i = -D_i^* M_i c_i \nabla_{T,p} \ln a_i, \tag{2.9}$$

where $D_i^* \equiv D_{i1}$ is the pseudo-binary diffusivity of species i in the pseudo-solvent species 1, M_i is molecular weight, c_i is molar concentration, and a_i is the activity. Since it has been assumed that the diffusing species are dilute it is possible to make the approximation (Merrill, 1996) $\ln a_i \approx \ln \phi_i + 1 + \chi_i$ where ϕ_i is volume fraction and χ_i is the Flory-Huggins interaction parameter for species i in the pseudo-species 1. Thus, since $\nabla \ln a_i \approx \nabla \ln \phi_i = (1/M_i c_i)\nabla \rho_i$, the diffusive flux can be approximated by

$$\mathbf{j}_i = -D_i^* \nabla \rho_i. \tag{2.10}$$

Unfortunately, there is not much data for the pseudo-binary diffusivity, D_i^*. However, the dilute assumption can again be called upon in order to use the relationship $D_i^* = D_i(1-\phi_i)^2(1-2\phi_i\chi_i)$ from Duda et al. (1982) where D_i is the self-diffusion coefficient of species i in the solvent. In the limit of small volume fractions ($\phi_i \to 0$), $D_i^* \approx D_i$. The differential form of the species conservation equation becomes

$$\frac{\partial \rho_i}{\partial t} + \boldsymbol{\nabla} \cdot (\rho_i \mathbf{v}) = \boldsymbol{\nabla} \cdot (D_i \nabla \rho_i) + r_i. \tag{2.11}$$

The simplified constitutive equation used Equation (2.11) assumes that the diffusing species are independently diffusing through a matrix that can be characterized independently of the concentrations of the diffusing species. The diffusing species can be identified with the volatile molecules, and the matrix can be identified with the polymer.

2.2.1.2 Conservation of Energy

Heat transfer into the system drives the pyrolysis reactions and is therefore of critical importance. The equations governing conservation of energy are largely analogous to those for species mass. The integral forms of conservation of energy for the gas and melt phases, neglecting gravitational potential, are

$$\frac{d}{dt}\int_{V^g} \rho e dV = -\int_{S^g} [\rho e(\mathbf{v}-\mathbf{v}_s) + \mathbf{q} - \mathbf{T}\cdot\mathbf{v}]\cdot \mathbf{n}_S dS - \int_I [\rho e(\mathbf{v}-\mathbf{v}_I) + \mathbf{q} - \mathbf{T}\cdot\mathbf{v}]^g \cdot \mathbf{n}_I dS \tag{2.12a}$$

$$\frac{d}{dt}\int_{V^g} \rho e dV = -\int_{S^g} [\rho e(\mathbf{v}-\mathbf{v}_s) + \mathbf{q} - \mathbf{T}\cdot\mathbf{v}]\cdot \mathbf{n}_S dS + \int_I [\rho e(\mathbf{v}-\mathbf{v}_I) + \mathbf{q} - \mathbf{T}\cdot\mathbf{v}]^m \cdot \mathbf{n}_I dS \tag{2.12b}$$

where $e \equiv u + v^2/2$ is the mass specific energy, u is the mass specific internal energy, $\mathbf{q}$ is the sum of all microscopic modes of energy transfer, and $\mathbf{T}$ is the stress tensor. At the interface,

$$[\rho e(\mathbf{v}-\mathbf{v}_I) + \mathbf{q} - \mathbf{T}\cdot\mathbf{v}]^m = [\rho e(\mathbf{v}-\mathbf{v}_I) + \mathbf{q} - \mathbf{T}\cdot\mathbf{v}]^g. \tag{2.13}$$

Summing Equations (2.12a) and (2.12b) and applying Equation (2.13) gives the conservation of energy equation for the entire control volume

$$\frac{d}{dt}\int_V \rho e dV = -\int_S [\rho e(\mathbf{v}-\mathbf{v}_s) + \mathbf{q} - \mathbf{T}\cdot\mathbf{v}]\cdot\mathbf{n}_S dS. \tag{2.14}$$

Equation (2.14) is very similar to the control volume conservation of mass equation except for the microscopic energy transport which unlike the sum of diffusional velocities is not necessarily zero.

As with the conservation of species equations, the appropriate constitutive equations must be introduced to make use of Equations (2.12)-(2.14). Using Fourier's law, neglecting the Dufour effect, and assuming the Fickian diffusion used in the previous section, the microscopic energy transfer vector may be expressed as $\mathbf{q} = -k\boldsymbol{\nabla}T - \sum_i h_i D_i \boldsymbol{\nabla}\rho_i + \mathbf{q}_{\mathrm{rad}}$ where h_i is the mass specific enthalpy of species i and $\mathbf{q}_{\mathrm{rad}}$ is the radiant flux vector. The negative of the divergence of the radiant flux vector is equal to the volumetric heating of the medium by radiation. This quantity is equal to the radiation absorbed minus the radiation emitted by the material. Various methods are available for approximating $-\boldsymbol{\nabla}\cdot\mathbf{q}_{\mathrm{rad}}$ (Siegel and Howell, 2002). Molten HDPE is translucent but may absorb radiation in the infrared region. At the high temperatures associated with thermal degradation radiation is likely to be important.

The differential form of conservation of thermal energy is similar to conservation of species mass. The thermal energy equation can be expressed in terms of temperature as

$$\rho c_p \frac{DT}{Dt} = \boldsymbol{\nabla} \cdot (k \boldsymbol{\nabla} T) - \nabla \cdot \mathbf{q}_{\text{rad}} + \beta T \frac{Dp}{Dt} + \sum_i h_i [\boldsymbol{\nabla} \cdot (D_i \boldsymbol{\nabla} \rho_i) + r_i], \qquad (2.15)$$

where $D(\cdot)/Dt$ denotes the material derivative and β is bulk expansion coefficient. Viscous heating has been neglected.

In the absence of bulk flow and radiation, a constant pressure systems is governed by

$$\frac{\partial \rho_i}{\partial t} = \boldsymbol{\nabla} \cdot (D_i \nabla \rho_i) + r_i, \qquad i = 1, \dots, N \qquad (2.16a)$$

$$\rho c_p \frac{\partial T}{\partial t} = \boldsymbol{\nabla} \cdot (k \boldsymbol{\nabla} T) + \sum_i h_i [\boldsymbol{\nabla} \cdot (D_i \boldsymbol{\nabla} \rho_i) + r_i], \qquad (2.16b)$$

Equations (2.16) have several unknown material properties (D_i, c_p, k, and h_i) as well as the unknown reaction rates, r_i. All of these parameters depend on the rapidly changing chemical composition of the system. For the gas phase physics, there are relatively few species and it is possible to solve equations such as Equations (2.16). Condensed phase polymeric systems, on the other hand, are composed of a large number of species (N is large). Alternative methods must be identified. In the next section, a framework is described for characterizing the evolution of the chemical composition of polymeric systems.

2.2.2 Mesoscale

The connection between molecular scale physics and the transport physics of the continuum scale is modeled at what will be referred to as the mesoscale. Mesoscale modeling involves identifying a simplified model of the chemical composition and

deriving the equations that govern the dynamics of the reduced model. In addition to the modeling polymer chemistry, it is important to quantify how material properties relate to the mesoscale model. The approach taken in the remainder of this dissertation is to treat the system of linear polymer chains as a population of notional particles distributed according to their chain length. The population referred to here is the collection of polymer molecules making up the condensed phase of a thermally degrading material. Such molecules share a structural similarity even though they may be of vastly different sizes. Furthermore, the bulk properties of the material, which are needed for simulating the continuum mechanics, are strongly dependent on the size distribution of the polymer chains. For these reasons, it is reasonable to characterize the condensed phase as a number density function. The evolution of this number density function is governed by the chemical kinetics of depolymerization.

Kinetic modeling of polymer pyrolysis is relatively well-developed (Grassie and Scott, 1985). It is generally assumed that linear thermoplastics degrade by a radical depolymerization mechanism, but many of the details of this mechanism are uncertain and vary among different materials. To test the validity of various possible mechanisms and rates it is helpful to have a general mathematical formalism for describing the evolution of a system of polymer chains. Such a formalism is provided by population balance equations (PBEs) (Ramkrishna, 2000). The underlying idea for PBEs is that the system may be treated as notional particles that are distributed according to some small set of internal coordinates such as size or conformation coordinates. This reduction is

sketched in Figure 2.16, and it amounts to the representation of the polymer melt as a number density function.

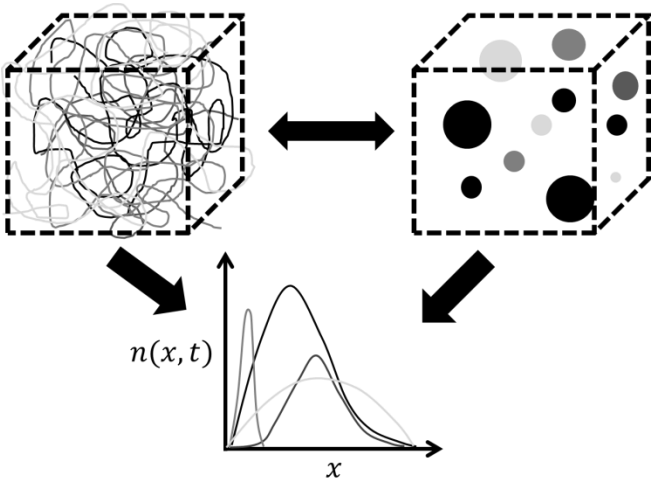

Figure 2.16: Representation of a polymer melt in the PBE formalism.

For polymeric systems, although the population is in fact discrete, the chains are distributed across a very large domain in the internal coordinate (carbon number) space. In many scenarios, it is possible to represent the number density function as continuous with respect to the size of the molecules. The continuous number density function is denoted $f(x,t)$, where $f(x,t)dx$ is the expected number of polymer chains with sizes in the interval $[x, x+dx]$. This is the approach taken by Ziff and McGrady (1986) and McCoy and Madras (1997). The relationship between the discrete representation of the number density versus the continuous representation is expressed as

$$f(x,t) \equiv \lim_{\Delta x \to 0} \frac{1}{\Delta x} \sum_{i \in [x, x+\Delta x]} \frac{\rho_i}{M_i}. \tag{2.17}$$

Also important is the inverse approximation

$$\rho_i \approx \frac{M_i}{x_2 - x_1} \int_{x_1}^{x_2} f(x) dx. \tag{2.18}$$

The validity of Equation (2.18) breaks down if $f(x)$ is rapidly varying in the interval $[x_1, x_2]$.

Since the chemical reactions involved in pyrolysis may be characterized as either breakage or aggregations, the population dynamics are governed by the PBE

$$\begin{aligned} \frac{\partial f}{\partial t} = 2 \int_x^\infty b(x') P(x|x') f(x') dx' - b(x) f(x) \\ + \frac{1}{2} \int_0^x a(x - x', x') f(x - x') f(x') dx' \\ - f(x) \int_0^\infty a(x, x') f(x') dx', \end{aligned} \tag{2.19}$$

where $b(x)$ is the specific breakage rate, $P(x|x')$ is the probability that a chain of size x' breaks to form at least one chain of size x, and $a(x, x')$ is the rate at which molecules of size x and x' aggregate. The material properties a, P, and b depend upon the mechanism and the rates for a particular polymer. In practice, the value of introducing a PBE to model species population dynamics is that it is a generalized formalism (and so it may be rapidly modified to incorporate additional chemical reactions) and it allows for problem-specific solution methods. The form of PBE presented in Equation (2.19) does not include species diffusion or convection. In typical problems, these processes occur on larger length scales than the chemistry. Therefore, it is possible to apply Equation (2.19) as a subgrid-scale chemistry model that may be coupled with a PDE such as Equation (2.16a) to account for spatial variations in the chemical composition.

As will be discussed in the next chapter, polymer melts are composed of several populations. These populations correspond to a small number of different types of polymer chains. Although the structural differences in these types of polymer chains are minor, they can lead to significantly different breakage and aggregation parameters in Equation (2.19). Taking these several populations into account requires several equations of the general form of Equation (2.19).

Two problems remain. First, a general numerical procedure for solving Equation (2.19) is needed. An approximate method is introduced and evaluated in Chapter 4. The second remaining problem is parameterizing Equation (2.19) with the appropriate reaction rates. This problem is addressed in the following section.

2.2.3 Molecular Scale

Consideration of molecular scale physics is necessary in modeling thermal degradation processes due to the complex evolving molecular structure of the system. The chemical composition varies greatly as pyrolysis proceeds, and this change in composition results in vastly different bulk material properties as the polymer melt is converted to wax and then to oil and ultimately to gas. Therefore, detailed models need to take into account the pyrolysis chemistry. This involves two components: the pyrolysis mechanism and the pyrolysis reaction rate constants. In this section, the relationship between the chemical mechanism and the PBE framework is clarified. In particular, it is demonstrated that the continuous PBE of Equation (2.19) is an approximation of a

discrete PBE. This discrete PBE can be directly derived from a reaction template formalism.

A chemical mechanism is a set of reactions that control the transformation of the species in the system. Each reaction in the mechanism has a chemical equation with a connectivity and a rate associated with it. The reaction mechanism is described by the set of chemical equations

$$\sum_{i=1}^{N} \nu'_{ij} \mathrm{X}_i \xrightarrow{k_j} \sum_{i=1}^{N} \nu''_{ij} \mathrm{X}_i \,, \qquad j = 1, \ldots, J \tag{2.20}$$

where X_i is a label for species i, k_j is the rate constant of reaction j, ν'_{ij} are the stoichiometric coefficients of the reactants, ν''_{ij} are the stoichiometric coefficients of the products, and J is the total number of reactions in the mechanism. Reverse reactions will be treated as a separate reactions. The reaction rates are computed as

$$R_j = k_j \prod_{i=1}^{N} c_i^{\nu'_{ij}} \,, \qquad j = 1, \ldots, J \tag{2.21}$$

where $c_i = \rho_i / M_i$ is the molar concentration of species i. Finally, the net rate of change of mass per unit volume of species i is found by summing the rates over all reactions

$$r_i = M_i \sum_{j=1}^{J} \nu_{ij} R_j \,, \qquad i = 1, \ldots, N \tag{2.22}$$

where $\nu_{ij} \equiv \nu''_{ij} - \nu'_{ij}$. Equations (2.20)-(2.22) present a formal way to determine the chemical generation terms in the species conservation of mass equations. Determining the pyrolysis mechanism is a matter of specifying the set of Equations (2.20). This is a task

for analytical chemists and is largely a matter of narrowing the list of all possible reactions to those that are most important. The proposed mechanism is then validated by comparison of predictions to experimental data.

The primary difficulty in modeling polymer pyrolysis mechanisms is that the number of reactions, J, is extremely large. Fortunately, since a given type of thermoplastic molecule is internally homogeneous, it will participate in a family of similar reactions. If it is assumed that this family of reactions has a kinetic rate constant that can be represented as a function of the sizes of the molecules involved, then it is possible to construct a *reaction template* to concisely describe that reaction family. A reaction template is just a chemical equation that describes a large family of elementary reaction. Templates express all of the information necessary to determine the rates of change of all species that take part in the associated family of reactions.

It is assumed that the system evolves due to *elementary* bimolecular and unimolecular reactions in which no more than two product molecules are formed. All such reactions can be expressed in one of four general forms: isomerizations, dissociations, additions, and disproportionations. Isomerizations and disproportionations require consideration of at least two types (or populations) of polymer chains. For purposes of simplicity, only the single population reaction templates for dissociations (breakages) and additions (aggregations) are considered below.

It is convenient to work on a molar basis. The species population is characterized by molar concentrations, and time rates of change of molar concentrations are $\bar{r}_i = r_i/M_i$.

The templates and rates for dissociation and addition reactions are listed in Table 2.1. Similar templates and rates exist for isomerization and disproportionation reactions, but their specification requires additional notation to account for the multiple populations.

	Reaction Template	Rates (contribution to $\bar{r}_i$)
Dissociation	$\mathrm{X}_i \xrightarrow{k_{ji}^d} \mathrm{X}_j + \mathrm{X}_{i-j}, \qquad i > j \geq 1$	$-c_i \sum_{j<i} k_{ji}^d + \sum_{j>i} \left(k_{ij}^d + k_{(j-i)j}^d\right) c_j$
Addition	$\mathrm{X}_i + \mathrm{X}_j \xrightarrow{k_{ij}^a} \mathrm{X}_{i+j}, \qquad \forall i, j$	$-c_i \sum_j \left(k_{ij}^a + k_{ji}^a\right) c_j + \sum_{j<i} k_{j(i-j)}^a c_j c_{i-j}$

Table 2.1: Reaction templates and associated rates for a single population.

Dissociation and addition reactions for polymers typically have helpful symmetric properties for their rate constant functions. For dissociations of symmetric polymer chains, $k_{ji}^d = k_{(i-j)i}^d$. For additions of symmetric polymer chains, $k_{ij}^a = k_{ji}^a$. Assuming these symmetries, the discrete form of the population balance equation is

$$\frac{dc_i}{dt} = 2\sum_{j>i} b_j P_{ij} c_j - b_i c_i + \frac{1}{2}\sum_{j<i} a_{j(i-j)} c_j c_{i-j} - c_i \sum_j a_{ij} c_j, \tag{2.23}$$

where $b_j \equiv \sum_{j<i} k_{ji}^d$, $P_{ij} \equiv k_{ij}^d / b_j$, and $a_{ij} \equiv 2k_{ij}^a$. Equation (2.23) is the discrete analog to the continuous PBE of Equation (2.19). Since the polymer chemistry does in fact involve discretely distributed polymer chains, the continuous PBE is in fact an approximation of the discrete form. The kinetic properties in the continuous form may be approximated by interpolating between the exact rates.

The rate constants assume an Arrhenius form, $k = A \cdot \exp(-E/RT)$. A full specification of the rate constant function for dissociation, for instance, would require the determination of $N \times N$ kinetic pairs. In practice, because of symmetries and other assumptions, the rate constant functions may be characterized by a small number of parameters. More will be said about the rate constants and Arrhenius parameters in the next chapter.

3: Modeling Pyrolysis Chemistry

Pyrolysis experiments, such as TGA, are simple and inexpensive. Unfortunately, since thermal degradation involves many coupled physical processes, the analysis of these experiments is difficult. The relationship between the observables and the underlying physics is complex. If experimental results are to be useful, they must be related to fundamental physical properties as opposed to fitted, non-physical model parameters. The link between experimental observables and material properties is obtained by realistic modeling of the governing physics. In this chapter, the modeling of pyrolysis in thermally degrading thermoplastics is discussed.

As mentioned in Chapter 1, attention is focused on linear thermoplastics because of their structural simplicity. Although the following discussion is relevant to all linear thermoplastics, it was necessary to limit the examples to HDPE. This chapter is divided into three sections. First, the mechanisms and rates of linear thermoplastics are presented. This section is primarily a survey of the literature. Second, reactive molecular dynamics (RMD) is used to study the initiation reaction in HDPE pyrolysis. Finally, TGA data is fit using two reasonable pyrolysis mechanisms and a simple model of volatile loss.

3.1 Review of Pyrolysis Mechanisms

Much of literature on thermal degradation assumes greatly simplified mechanisms. The most basic mechanism couples chemistry and devolatilization into a single step process represented by the reaction

$$\text{Polymer} \xrightarrow{k} \text{Gas}. \tag{3.1}$$

This is the mechanism assumed by Equation (2.1). Such a simple description neglects the details of the pyrolysis chemistry and mass loss. Additionally, this model provides no information about the chemical composition of the pyrolysis gas, and it is therefore unhelpful for many applications.

In reality, polymers degrade in reaction steps with intermediate species playing an important role. Lyon (1998) proposed a slightly more detailed mechanism in which polymers were converted to intermediate species, and the intermediates are converted to gas, char, or back to polymers. The intermediate species is treated as a transition state, and so its concentration is in a quasi-steady state. This model allows for the prediction of char formation, and by including the intermediate species, it adds some of the complexity of real pyrolysis reactions. However, it is not truly mechanistic. The reaction rates must be found by fitting the model to data, and it provides no information about the composition of the melt or gas phases.

A drawback of the two preceding descriptions of pyrolysis chemistry is that they both require fitting the model to data. They are not founded on elementary reactions with well-defined rate constants. For this reason, they are not generally useful for extrapolation to scenarios outside of those in which the experimental data was obtained. Prediction of behavior in experimentally inaccessible scenarios requires rational, physics-based modeling of the pyrolysis mechanism.

A physically reasonable model is the random scission mechanism

$$\mathrm{P}_i \xrightarrow{k} \mathrm{P}_j + \mathrm{P}_{i-j}, \tag{3.2}$$

where P_i denotes a linear polymer chain of size i. The mechanism is called random since the rate constant is the same for all bonds. This model has been used in much of the polymer pyrolysis modeling literature (Montroll and Simha, 1940; Simha, 1941; Ziff and McGrady, 1986; McCoy and Wang, 1994; Staggs, 2002). This mechanism has an analytical solution (Simha, 1941) if k is constant in time (i.e., for isothermal scenarios). However, Equation (3.2) is not chemically valid since the products of a homolytic scission are always radicals with much higher reactivities as compared to the stable polymer chains.

The determination of chemically feasible mechanisms for polymer pyrolysis is largely driven by analogy to gas phase pyrolysis. To a first approximation, realistic thermoplastic pyrolysis can be modeled as a radical depolymerization process. This mechanism is essentially the reverse of addition polymerization (Flory, 1953). Many authors have utilized this mechanism in modeling pyrolysis (Inaba and Kashiwagi, 1986; Staggs, 2007). The radical depolymerization mechanism is

$$\mathrm{P}_i \xrightarrow{k^i} \mathrm{R}_j + \mathrm{R}_{i-j}, \tag{3.3a}$$

$$\mathrm{R}_i \xrightarrow{k^d} \mathrm{R}_{i-1} + \mathrm{P}_1, \tag{3.3b}$$

$$\mathrm{R}_i + \mathrm{X}^* \xrightarrow{k^{t1}} \mathrm{P}_i + \mathrm{X} \tag{3.3c}$$

$$\mathrm{R}_i + \mathrm{R}_j \xrightarrow{k^{t2}} \mathrm{P}_{i+j}, \tag{3.3d}$$

$$R_i + R_j \xrightarrow{k^{t3}} P_i + P_j, \tag{3.3e}$$

where P_i and R_i denote stable polymers and primary radicals of length i. The superscripts on the rate constants refer to initiation (i), depropagation (d), and termination (t). Three types of termination reactions are listed: first-order ($t1$), second-order recombination ($t2$) and second-order disproportionation ($t3$). The depropagation reaction is often referred to as β-scission since the breakage is of the β-bond which is the second bond from the radical chain end. A flowchart of the radical depolymerization mechanism is provided in Figure 3.1. The key characteristic of the radical depolymerization mechanism is that $k^d \gg k^i$ and so the chains will tend to unzip to produce mostly monomers.

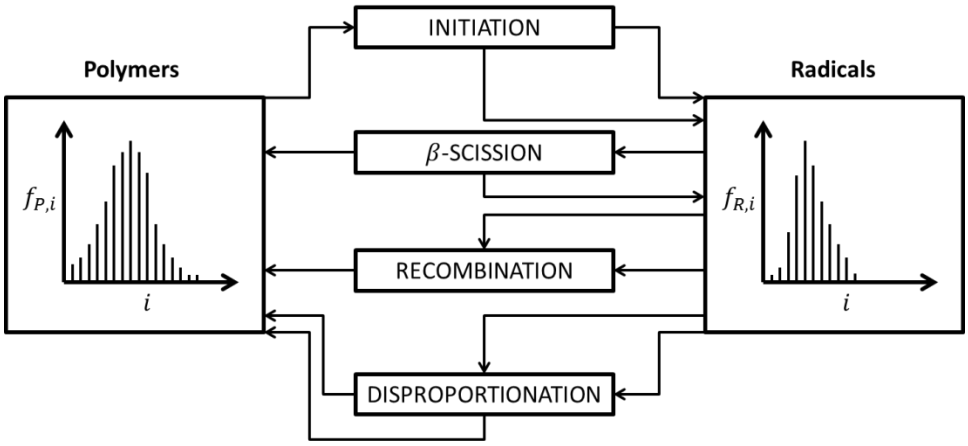

Figure 3.1: Flowchart of mass transfer in radical depolymerization.

Monomer yield is a measure of the degree to which the pyrolysis mechanism is dominated by radical depolymerization. For various vinyl polymers, the monomer yield can vary from more than 99% of the gas yield weight for poly(methyl atropate) to 42-45% for polystyrene to 0.03% for polyethylene (Cullis and Hirschler, 1981). These

differences are thought to be due to differences in the steric hindrance of different substituent groups. Specifically, it is believed that large substituent groups tend to block hydrogen transfer reactions. The general rule is that the larger the substituent groups on a vinyl polymer the more dominant is pure radical depolymerization. Polyethylene has the smallest possible substituents (hydrogen atoms), and therefore has the lowest monomer yield. The low monomer yield of polyethylene pyrolysis implies that pure radical depolymerization is not the dominant mechanism—other reactions must be taken into account.

More accurate results for polyethylene pyrolysis have been obtained by adding the isomerization reactions found in the Kossiakoff-Rice mechanism (Kossiakoff and Rice, 1943). This mechanism takes into account the "back-biting" reactions that transfer an unpaired electron site from the end of the radical molecule (primary radical) to one of the near-end carbon atoms (secondary radical). This mechanism was originally proposed for the gas phase pyrolysis of small paraffins. This same mechanism has been applied to polymer pyrolysis for many years with several simplifying assumptions such as a quasi-steady radical concentration (Simha et al., 1950; Simha and Wall, 1951; Simha and Wall, 1952). Comprehensive reviews are provided by Boyd (1970) and Jellinek (1978). Recently, more detailed implementations of the radical depolymerization plus hydrogen transfer mechanism have been implemented (Ranzi et al., 1997; Faravelli et al., 1999; Mastral et al., 2007).

A detailed survey of the mechanisms and rates in polyethylene pyrolysis is provided by Poutsma (2003), but several complicating factors will be mentioned here. It is typically assumed that there is no branching. As was discussed in Chapter 1, this is not exactly true for HDPE. The initiation activation energy at a branch point has been estimated to be around 1.6 kcal/mol less than the initiation activation energy at an unbranched backbone bond in polyethylene (Ranzi et al., 1997). Thus at a temperature of 400˚C, the bonds at branch points should break more than three times as fast as the typical backbone bonds. One approach for taking this effect into account is to include a certain number of randomly distributed "weak links" in any given polymer chain (Jellinek, 1978). Conversely, carbon-carbon double bonds are effectively unbreakable at the temperatures and timescales of pyrolysis. Most of the GC-MS data for HDPE pyrolysis reports a significant presence of double bonds associated with unsaturated carbon atoms. These double bonds are associated with the production of various alkenes (olefins) and dialkenes during radical depolymerization. The theoretical ratio of alkanes:alkenes:dialkenes is 1:2:1 (Poutsma, 2003) although this is rarely observed. In general, a large amount of alkenes are produced but the relative amount tends to vary with temperature. Another relatively strong bond is between carbon and hydrogen atoms. As temperature increases, though, hydrogen stripping becomes increasingly important.

The relative strengths of the various bonds can be examined by looking at ethane and ethylene pyrolysis. For ethane, the homolytic C—C scission reaction has an activation energy of around 84 kcal/mol (Kunugi et al., 1969). For comparison, the

double bond in an ethylene molecule has an activation energy of scission of around 167 kcal/mol, and so double bond breakages are very unlikely and can safely be neglected. Hydrogen stripping of ethane has an activation energy of approximately 98 kcal/mol and is only significant at relatively high temperatures.

One consequence of assuming unbreakable C—H bonds is that there will be no molecular hydrogen in the system. Experiments generally confirm that the amount of H_2 is small in HDPE pyrolysis gas. Even at relatively high temperatures ($\sim 640^{\circ}C$), the yield of H_2 is around 0.09% of the weight of the HDPE pyrolysis products (Mastral et al., 2003). Breaking C—H bonds in polyethylene is a special case of chain stripping in which substituent groups are removed. Chain stripping generally leads to aromatization and charring. The fact that minimal charring occurs in HDPE pyrolysis (see Chapter 1 and Sakata et al. (1996)) indicates that C—H bond breakage is not significant. Similarly, aromatization will be neglected in subsequent modeling in this dissertation. Small amounts of aromatic species have been detected in HDPE pyrolysis experiments, but at typical temperatures, the amount of aromatics produced by pyrolysis seems to be negligible—0.06 weight percent at $450^{\circ}C$ (Ng et al., 1995). As temperature increases, the amount of aromatics increase—1.5 weight percent at $640^{\circ}C$ (Mastral et al., 2003). This trend is due to the increased likelihood of hydrogen stripping at higher temperatures.

The discussion above involves qualitative descriptions of pyrolysis in the form of several chemical mechanisms. If a mechanism is to be used, the reaction rates must be

quantified. In the next section, the Arrhenius parameters for the chain initiation reaction are estimated using several approaches.

3.2 CHAIN INITIATION RATES

The most common approach for estimating condensed phase pyrolysis kinetic parameters is to use experimental data from TGA or GC-MS, and then calibrate the rate constants to fit the experimental data. Most often in the pyrolysis literature, this calibration has been carried out assuming the lumped mechanism of Equation (3.1). Reviews of the large body of literature taking this approach can be found in Westerhout et al. (1997) and Ceamanos et al. (2002). This traditional approach will be applied at the end of this chapter. In this section, two fundamental approaches are applied for estimating the chain initiation reaction rate: (1) approximation by gas phase rates and (2) reactive molecular dynamics simulations. The advantage of fundamental approaches is that they avoid the complications associated with calibration. Specifically, they do not require new data or data reduction models. Additionally, since they are fundamental, they are more likely to be reliable for predictions in untested scenarios.

Another possible approach is to use group additivity principles (Benson, 1976; van Krevelen and te Nijenhuis, 2009) to estimate the bond dissociation energy which is closely related to the activation energy. In Chapter 6, group additivity is used to estimate thermodynamic properties including the energy absorbed during the initiation reaction.

3.2.1 Gas Phase Rates

Condensed phase reaction rates can be estimated using analogous gas phase reaction rates of smaller molecules. One problem with this approach is that it neglects the cage effects of the surrounding condensed phase. To account for condensed phase effects, Ranzi et al. (1997) made corrections to the gas phase activation energies based on estimates of the heat of vaporization of the polymer chains. This correction resulted in a decrease in the gas phase activation energy for carbon-carbon backbone scission of 5.3 kcal/mol, a reduction that Poutsma (2003) argues does not agree with the experimental data. Furthermore, it is believed that the rate constants decrease significantly with chain length, and this dependency cannot be fully captured by the pyrolysis kinetics of a few small species.

Despite these concerns, it is helpful to look at the gas phase kinetics of low carbon number analogs to HDPE. Literature values for these reactions are listed in Table 3.1. The label "allyl" refers to the scission of the second bond away from the double bond. To see the relative importance of these reactions at pyrolysis temperatures, the rate constant is computed at 400°C. Activation energies are in units of kilocalories per mole of bonds.

Initiation Reaction	Ref.	$\log A(1/\mathrm{s})$	E, kcal/mol	$k(T = 400°C) \times 10^{12}$, 1/s
Backbone	(a)	14.9	82.1	1.67
Allylic	(a)	13.5	71.5	185
Ethane	(b)	16.6	87.5	1.47
	(c)	18.1	84.0	637
	(d)	17.0	89.0	1.20
Propane	(b)	16.3	84.5	6.95
	(d)	16.9	86.0	9.00
Butane (mid)	(b)	16.2	82.1	33.2
	(d)	16.7	83.0	53.6
	(e)	15.7	81.0	23.9
	(f)	17.4	86.3	22.7
Butane (end)	(b)	17.0	85.4	17.8
	(e)	15.7	85.0	1.20
Propene	(b)	17.9	95.0	0.107
	(c)	16.0	95.0	0.00135
1-butene (allyl)	(c)	16.9	74.0	71,400
1-pentene (allyl)	(f)	16.4	73.1	44,300

Table 3.1: Gas phase initiation reaction kinetics; (a) Ranzi et al. (1997), (b) Sundaram and Froment (1978), (c) Kunugi et al. (1969), (d) Dente and Ranzi (1983), (e) Powers and Corcoran (1974), (f) Poutsma (2003).

Several observations can be made from the data in Table 3.1. The data from Kunugi et al. (1969) disagrees significantly with data from other sources. It is also surprising that the "typical" propene bond breaks so much slower than the "typical" propane bonds. The two butane rates indicate that the end bonds break faster than mid-chain bonds. This would lead to the production of a large number of methyl radicals formed upon initiation. Also, rates seem to increase with chain length—butane breaks faster than propane which breaks faster than ethane. The allylic scissions are much faster than other bond breakages. This could explain the relatively large amount of propane and propene in HDPE pyrolysis gas. Finally, it is observed that bonds next to double bonds break relatively slowly.

These observations are helpful for understanding the qualitative behavior of the chain initiation reaction, but there is no clear methodology for translating these quantitative rates into their condensed phase values. Fortunately, simulation is becoming increasingly feasible for studying condensed phase chemistry.

3.3 REACTIVE MOLECULAR DYNAMICS

Molecular dynamics (MD) may be used to investigate a variety of microscale phenomena. The focus of this section is limited to using MD for the determination of the HDPE chain initiation rates, but classical MD might also be useful for predicting various thermophysical properties at experimentally unattainable conditions.

Reactive MD (RMD) accounts for the changes in electronic structure accompanying a reaction. In RMD, the classical equations of motion are integrated to

predict atomic trajectories under the influence of a reactive forcefield. Such a forcefield is defined by its ability to estimate the forces on atoms as they undergo the electronic changes associated with the breaking and forming of bonds. The advantage of RMD is its ability to be used to study reaction kinetics in complex environments such as the condensed phase. RMD has been used to examine the effects of chain length on the backbone scission rate in linear polyethylene molecules (Knyazev, 2007). The primary difficulty of RMD is determining the reactive forcefield.

One class of reactive forcefields is based on empirical bond order potentials. This class includes the reactive empirical bond order (REBO) and the adaptive intermolecular REBO (AIREBO) potentials (Brenner, 1990) as well as the ReaxFF forcefield (van Duin et al., 2001). These empirical methods involve a large number of parameters, and it is unclear whether they generalize to scenarios beyond those in which the parameters were obtained.

An alternative approach has been developed by Nyden et al. resulting in the reactive forcefield MD_REACT (Nyden et al., 1992) and RMDff (Smith et al., 2007). Rather than using heavily parameterized bond order functions, these forcefields employ a switching function to smooth the transition between the forcefields for reactants and products. The switching function is parameterized by a fit to *ab initio* (density functional theory) calculations for small scale analogous reactions. The more recent forcefield, RMDff is built upon the MM3 forcefield and is implemented in a free-standing, open-source C++ code RxnMD (Smith et al., 2011).

RxnMD was used to study the initiation reaction in condensed phase linear alkane molecules of varying lengths. The primary goals were to determine Arrhenius parameters for the molecules as a function of chain length and bond location. The simulations were performed with periodic boundary conditions, and the structures were annealed by non-reactive MD and minimization using the commercial MD code Hyperchem. The annealing was done to achieve an approximate mass density of 0.80-0.85 g/cc. A typical structure for an *n*-alkane with 50 carbon atoms is shown in Figure 3.2.

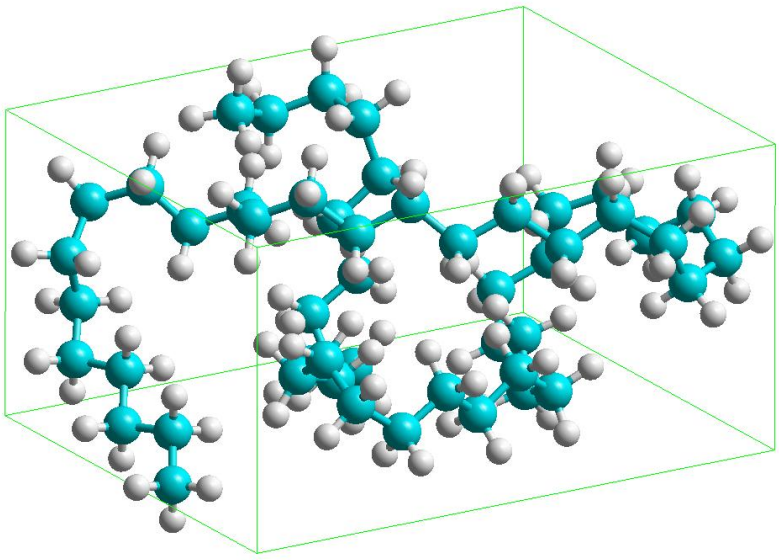

Figure 3.2: An annealed *n*-alkane with 50 carbon atoms used as an initial structure for RMD simulations.

For a given structure, many simulations were run using randomly chosen initial conditions for the velocities. The randomly seeded systems were allowed to equilibrate using non-reactive MD for 10 ps of simulation time. Only carbon-carbon scission reactions were allowed in the RMD simulations. Simulations were performed at constant

volume and energy (NVE) with temperatures ranging from 1800-4800 K. These temperatures are unrealistically large but necessary for the observance of a chain initiation within a reasonable amount of CPU time (up to several days for the larger systems). Several systems were considered, and their labels and descriptions are listed in Table 3.2.

Structure Label	Description
PE-1	25 single unit "chains", C_2H_4
PE-5	6 five-unit chains, $C_{10}H_{12}$ (*n*-decane)
PE-25	1 25-unit chain, $C_{50}H_{102}$
PE-50	1 50-unit chain, $C_{100}H_{202}$

Table 3.2: Simulated structures used in RMD study.

The recorded observables from a given simulation were the simulation temperature and the time to the first reaction. These observables were plotted in an Arrhenius plot so that the slope and intercept of the linear fit provided the activation energy and pre-exponential for a given molecule. An Arrhenius plot containing the data for the PE-1 and PE-25 structures is given in Figure 3.3. The rate constants ($1/t_s$) were normalized by the number of C—C bonds in the system. The location of the broken bond was also recorded. A histogram of this data for the PE-25 structure is shown in Figure 3.4. It appears from this histogram that the RMD simulations indicate that the chain initiation reaction is random.

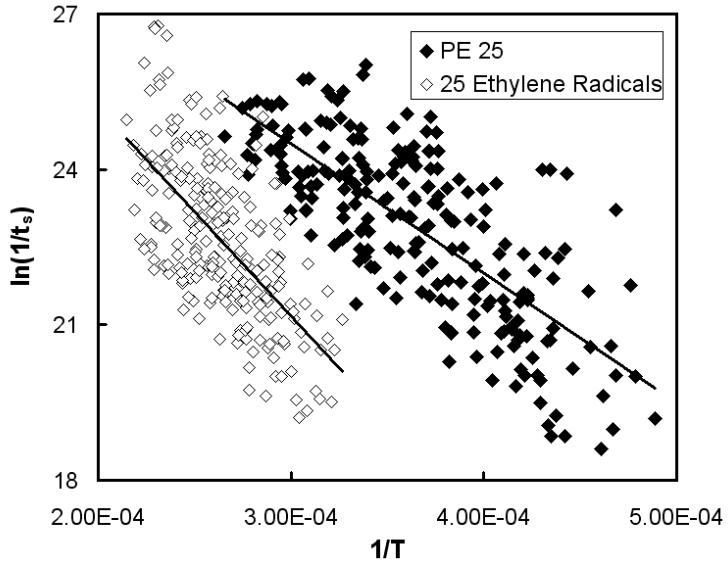

Figure 3.3: Arrhenius plot of RMD results for PE-1 and PE-25 structures.

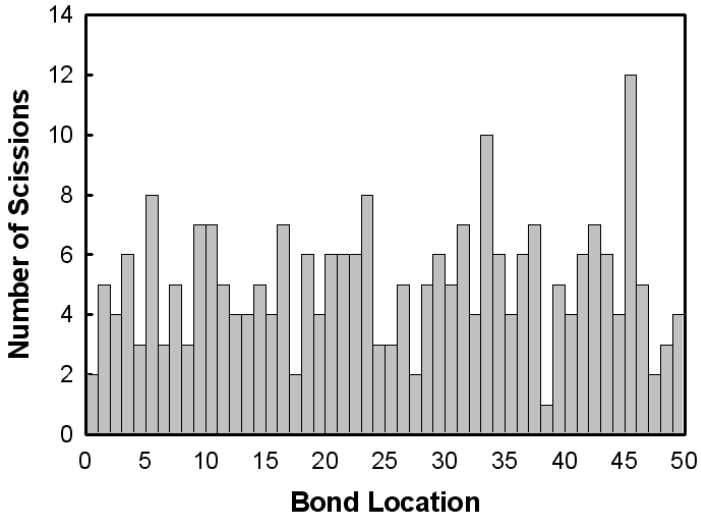

Figure 3.4: Histogram of broken bond location for RMD simulations of the PE-25 structure.

The RMD results presented here were combined with additional simulations performed by a collaborator (Dr. K.D. Smith) for a similarly prepared $C_{200}H_{402}$ chain. The results were binned in terms of temperature, and the combined Arrhenius plot is provided in Figure 3.5. The resultant pre-exponentials for all structures were approximately the same ($\sim 10^{15}$). The activation energies are plotted in Figure 3.6 as a function of carbon number, i. Also included in Figure 3.6 is condensed phase initiation activation energy estimated by Ranzi et al. (1997) of 321 kJ/mol. This estimate was based on correcting the gas phase value using thermodynamic arguments and the heat of vaporization. While Poutsma (2003) claims that this is an over-reduction in activation energy, the RMD simulations indicate that the reduction is not large enough.

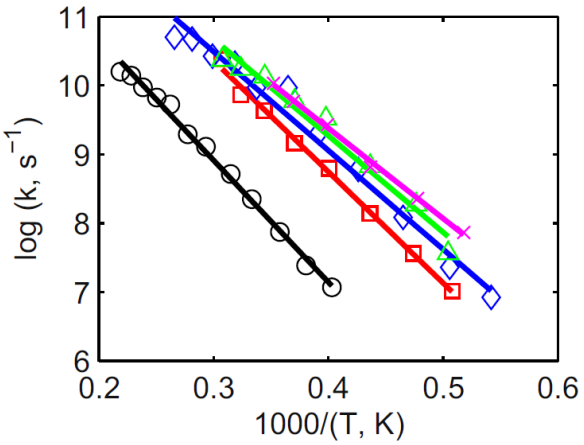

Figure 3.5: Binned Arrhenius plot for all structures studied in RMD: PE-1 (○), PE-5 (□), PE-25 (◊), PE-50 (Δ), and PE-100 (×) (from Smith et. al 2011).

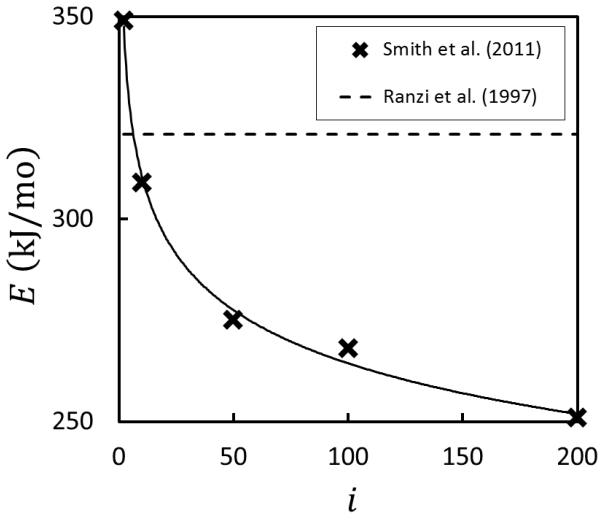

Figure 3.6: Predicted activation energy from RMD simulations as a function of carbon number i. Dashed line is the predicted condensed phase initiation rate of Ranzi et al. (1997).

It is appears as though the activation energies in Figure 3.6 are converging for large molecules. Unfortunately, simulations of larger molecules were too expensive to confirm this hypothesis. There is reason to believe, however, that the activation energy converges as the chains approach their entanglement, or critical, chain length. The entanglement chain length represents the length over which a section of a polymer chain is affected by the dynamics of another section. Van Krevelen and te Nijenhuis (2009) report a entanglement MW for polyethylene of 3,500 g/mol which corresponds to a carbon number of 250. It is therefore reasonable to assume that the limiting value of $E = 251$ kJ/mol at $i = 200$ is approximately the maximum value.

In this section, two methods for approximating HDPE chain initiation kinetic parameters were applied. The gas phase analogy provides only qualitative information about the kinetics of the condensed phase. While RMD is promising, further work is

needed for validation of the methodology. Furthermore, RMD is time-consuming, and results were only determined for one step in the pyrolysis process. In the next section, calibration with TGA data is used to determine kinetic parameters for several reactions assuming several different pyrolysis mechanisms.

3.4 CALIBRATION WITH TGA

In this section, several simple models of thermal degradation are calibrated using TGA data for HDPE and poly(methyl methacrylate) (PMMA). PMMA was chosen because of the availability of literature data and because PMMA pyrolyzes by simple radical depolymerization. That is hydrogen transfer reactions are not believed to take place at significant rates in PMMA pyrolysis. Evolved gas data indicates that this is true since the measured pyrolysis gas composition is mostly ($\sim 91-98\%$ by weight) methyl methacrylate monomers (Cullis and Hirschler, 1981). The models are: (1) a single-step Arrhenius model, (2) a random scission PBE, and (3) a radical depolymerization PBE. The two PBE models are solved using a simple application of the quadrature method of moments (QMOM) (McGraw, 1997). The model parameters are calibrated by optimization to minimize the sum of squared errors between the model prediction and the data. The results presented in this section can be found in Bruns et al. (2009).

3.4.1 Models

The most commonly applied model of degradation takes the form of a sum of Arrhenius terms. Since polymer degradation is driven by chemical reactions, an

Arrhenius model form is reasonable as a first approximation. For this study, the Arrhenius model considered is a single-term variable-order form equation

$$\frac{dw}{dt} = -Aw^{\psi} \exp\left(-\frac{E}{RT}\right). \tag{3.4}$$

A less arbitrary alternative to the global Arrhenius model is to derive PBEs from physical descriptions of the degradation mechanism. The random scission mechanism of Equation (3.2) is governed in its approximate continuous form by

$$\frac{\partial f}{\partial t} = -kxf(x) + 2k\int_x^{\infty} f(x')dx', \tag{3.5}$$

where k is the bond-specific scission rate or the rate of breakage for any single bond. Equation (3.5) is a special case of Equation (2.19) in which $a(x, x') = 0$, $b(x) = kx$, and $P(x|x') = 1/x'$. Other models allow for more general forms for the breakage rate and probability (McCoy and Wang, 1994).

The random scission model provides a reasonable physical description of how the polymer chains degrade, but it is not chemically precise. The final model considered in this section is the chemically reasonable radical depolymerization mechanism described by Equations (3.3). Radical depolymerization is governed by the coupled PBEs

$$\frac{\partial f_p}{\partial t} = k^{t1} f_r(x) - k^i x f_p(x), \tag{3.6a}$$

$$\begin{aligned}\frac{\partial f_r}{\partial t} = 2k^i \int_x^{\infty} f_p(x')dx' + k^d \int_x^{\infty} f_r(x')\delta\big(x - (x' - x_1)\big)dx' \\ - (k^d + k^{t1}) f_r,\end{aligned} \tag{3.6b}$$

where δ is the delta function, f_p is the number density of polymers, and f_r is the number density of radicals. The form of Equations (3.6) is different for the monomer, $x = x_1$, since monomers cannot break. This complication is neglected since it will be assumed that monomers are devolatilized immediately upon formation.

Equations (3.5) and (3.6) are models of pyrolysis only. In order to compare to TGA data, mass loss must be accounted for. The first-order approach for accounting for mass loss in pyrolysis PBEs is to postulate a critical size, l. All species smaller than l are immediately devolatilized from the sample. That is $f(x < l) = 0$.

3.4.2 Solution Methods

The Arrhenius model of Equation (3.4) is easily simulated using standard numerical integration methods. The solution of the PBEs requires more sophisticated techniques. In the following, the method of moments is applied to Equations (3.5) and (3.6). Moment methods neglect details of the number density function, but they provide sufficient information for simulating TGA. Specifically, the only quantity of interest for TGA is the normalized mass, $w(t)$, of the system which is fully determined by the first moment of the total population of polymer chains. The k^{th} moment of the population is defined as

$$\mu^{(k)} \equiv \int_0^\infty x^k f(x)dx = \int_l^\infty x^k f(x)dx, \tag{3.7}$$

where the second equality holds because of the assumed critical size mass loss mechanism. For the case of the radical depolymerization mechanism, the total number density function is $f = f_p + f_r$. The normalized mass is

$$w(t) = \frac{\mu^{(1)}(t)}{\mu^{(1)}(t=0)}, \tag{3.8}$$

for both PBE models where the first moment, $\mu^{(1)}$, is the mass of the population per unit mass of x.

Applying the moment operator in Equation (3.7) to Equations (3.5) and (3.6) results in differential equations governing the moments of the number density function. For the random scission model, the resultant equations are

$$\frac{d\mu^{(0)}}{dt} = k\left(\mu^{(1)} - 2l\mu^{(0)}\right), \tag{3.9a}$$

$$\frac{d\mu^{(1)}}{dt} = -kl^2\mu^{(0)}. \tag{3.9b}$$

If mass loss is not allowed, then the critical size, l, equals zero, and so $d\mu^{(1)}/dt = 0$. A large critical size allows for more molecules to devolatilize, leading to a faster mass loss rate. It can be shown that the number average size of the devolatilized molecules is $l/2$. For isothermal TGA, k is constant, and the analytical solution of Equations (3.9) gives a normalized mass of

$$w(t) = \left[\frac{kl(i_0 - l)}{M_0}t + 1\right]\exp(-klt), \tag{3.10}$$

where i_0 is the initial number average size of the polymer.

Unlike the random scission model, the moment equations for radical depolymerization are unclosed—that is, the differential equations for the first two moments are in terms the second moment. The quadrature method of moments (QMOM) is an approach for closing moment equations in terms of low order moments. In the QMOM, Gaussian quadrature is used to approximate the moment integrals so that

$$\mu^{(k)} = \sum_{p=1}^{M} w_p x_p^k, \tag{3.11}$$

where M is the number of quadrature points (or the order of the approximation), w_p are quadrature weights, and x_p are referred to as quadrature points or nodes. The right-hand side of Equation (3.11) contains $2M$ unknowns. Therefore, if $2M$ moments are known, Equation (3.11) may be solved for the unknown quadrature weights and nodes. For the one point case ($M = 1$), the solution in terms of the first two moments is $w_1 = \mu^{(0)}$ and $x_1 = \mu^{(1)}/\mu^{(0)}$. The second moment is then approximated as $\mu^{(2)} \approx w_1 x_1^2 = \left[\mu^{(1)}\right]^2/\mu^{(0)}$.

Under the one-point quadrature approximation, the moment equations for the radical depolymerization mechanism are

$$\frac{d\mu_p^{(0)}}{dt} = k^{t1}\mu_r^{(0)} - k^i \mu_p^{(1)}, \tag{3.12a}$$

$$\frac{d\mu_p^{(1)}}{dt} = k^{t1}\mu_r^{(1)} - k^i \frac{\left[\mu_p^{(1)}\right]^2}{\mu_p^{(0)}}, \tag{3.12b}$$

$$\frac{d\mu_r^{(0)}}{dt} = 2k^i\left(\mu_p^{(1)} - l\mu_p^{(0)}\right) - k^{t1}\mu_r^{(0)}, \tag{3.12c}$$

$$\frac{d\mu_r^{(1)}}{dt} = k^i\left(\frac{\left[\mu_p^{(1)}\right]^2}{\mu_p^{(0)}} - l^2\mu_p^{(0)}\right) - k^d l\mu_r^{(0)} - k^{t1}\mu_r^{(1)}, \tag{3.12d}$$

where $\mu_p^{(k)}$ and $\mu_r^{(k)}$ denote moments of the polymer and radical populations. Solution of these equations requires specification of the initial conditions and Arrhenius parameters for all four rate constants. Equations (3.12) are typically stiff and so all time integrations were performed using Gear's method (Gear, 1971).

3.4.3 Optimization-Based Calibration

In this section, all three pyrolysis models are fit to dynamic TGA data for HDPE and PMMA using optimization to minimize the sum of squared errors. The optimization problem is to minimize the sum of squared errors computed as

$$E_2 \equiv \sum_i \left[w_{e,i} - w_m(T_i|\mathbf{K})^2\right], \tag{3.13}$$

where $(T_i, w_{e,i})$ is an experimental data point, w_m is a model prediction, and $\mathbf{K}$ is a vector containing the kinetic parameters. The solution, $\mathbf{K}^*$, is defined as the kinetic parameters that minimize the sum of squared errors. Solutions were found using sequential quadratic programming (SQP). The kinetic compensation effect presents a challenge for finding unique solutions. As with any optimization problem the question of local minima arises. When using gradient-based algorithms like SQP, there is no test for determining whether the solution is indeed the global minimum. The first two models are first-order linear

systems so their solutions will be well-behaved. Furthermore, because both models are in a three-dimensional parameter space, it is possible to explore the behavior of the objective function to some extent. The radical depolymerization model is more difficult since it is higher dimensional and nonlinear. In an attempt to overcome these difficulties, a genetic algorithm was employed towards the solution of the radical depolymerization optimization problem. Global search heuristics such as genetic algorithms allow one to find the minimum of several local minima. The solutions generated by the genetic algorithm failed to find a smaller E_2 than was found using SQP.

In order to check for the uniqueness of the SQP solutions, two starting points were taken for each case. It was found that different starting points led to different solutions indicating either the existence of local minima or an objective function that is relatively flat for large regions of the parameter space.

TGA data for the degradation of PMMA were obtained from Ferriol et al. (2003). The material was from Aldrich with an initial weight-averaged molecular weight of 350,000 g/mol. The data were obtained at heating rates of 2, 5, 8, and 10 K/min.

In order to better understand the behavior of the objective function for the random scission model, the sum of squared errors was plotted versus A and E in Figure 3.7. It was assumed that the critical size corresponded to a monomer. The region computed was limited somewhat because of the high computational cost of integrating the differential equations for fast kinetics.

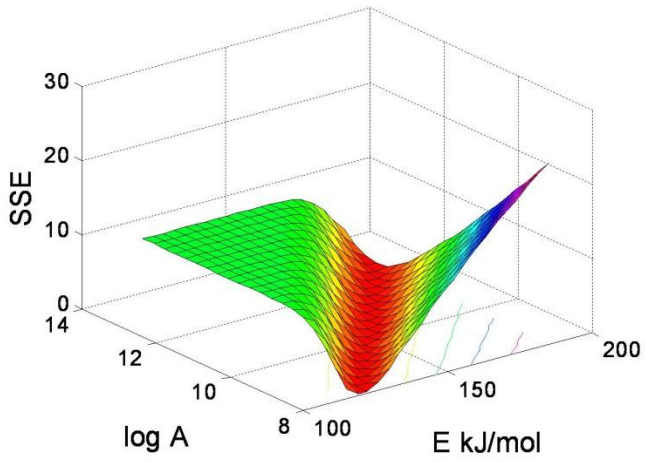

Figure 3.7: The sum of squared errors for PMMA as a function of the Arrhenius parameters A and E assuming a critical size of $l = 1$ in the random scission pyrolysis model.

Figure 3.7 is interesting for several reasons. First, the graph clearly shows the kinetic compensation effect: there is a distinct valley in the surface along which the model closely predicts the experimental data. It was found that although the objective function is relatively flat along this kinetic compensation line, there is a distinct but shallow minimum at $A = 5.495e9\ \mathrm{s}^{-1}$ and $E = 130\ \mathrm{kJ/mol}$. A second interesting feature of Figure 3.7 is the flat region for large *A* and small *E*. This is due to the fact that the experimental data points are taken only over a limited range of temperatures. The diagram in Figure 3.8 helps explain this effect. The plot shows experimental (×) and predicted (lines) TGA data. The "good" solution represented by '⋯' will have a small value error (E_2). However, even though the '— ·· ' solution is better than the '— —' solution, both will have the same E_2 equal to the sum of squared errors between the data

with the $w = 0$ axis. Although it is not plotted in Figure 3.8, there is a similarly flat region corresponding to simulation results with very slow kinetics—the model completely overshoots the experimental data.

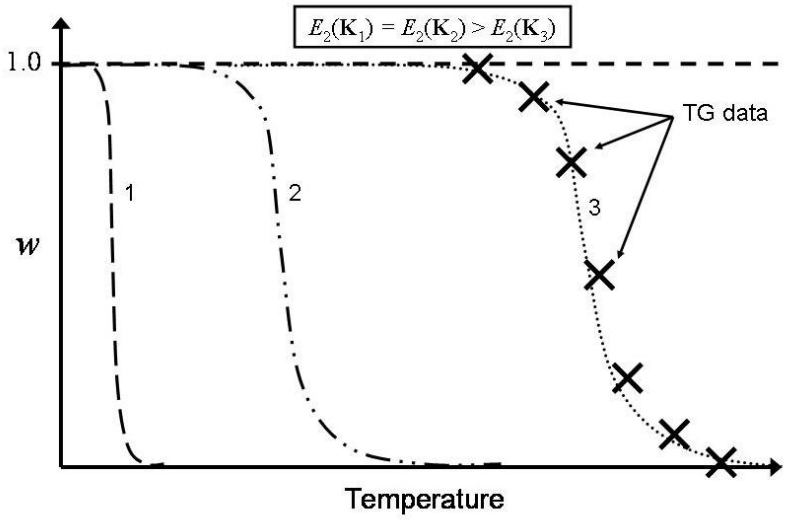

Figure 3.8: Diagram showing the independence of E_2 to **K** for fast kinetics.

The point of plotting the objective function is to see if it is well-behaved for optimization. This is the case with respect to A and E as is shown in Figure 3.7. A similar plot was made of the variation of E_2 with respect to the critical size, l, and this plot was similarly smooth. This is evidence that a gradient-based optimization algorithm should perform well. The only difficulty is the flatness of the objective function in three regions. In the too fast and too slow regions, the objective function is perfectly flat. Therefore, if a starting point is chosen in one of these regions, the optimality conditions will be satisfied, but the value of E_2 will be large. Consequently, care must be taken to start the

optimization algorithm at a point in parameter space where the numerical solution is close to the experimental data. In other words, the algorithm must be started somewhere in the valley seen in Figure 3.7. The third region that might present difficult to an optimization algorithm is the kinetic compensation line at the bottom of this valley. Although there are differences in E_2 along this line, for some regions of the parameter space, the differences might be too small to numerically differentiate.

For a three-dimensional space, this type of mapping of the parameter space is not difficult. For the seven-dimensional parameter space corresponding to the radical depolymerization model, this type of mapping is infeasible. There will be a kinetic compensation effects for this model, both *within* each reaction, and *between* the three reactions. It is therefore possible that several local minima exist throughout the parameter space. As was mentioned previously, a genetic algorithm was attempted, but it failed to find a better solution than the SQP algorithm.

A summary of the optimization results for PMMA is provided in Table 3.3. For each model, two starting points were attempted, denoted by $\mathbf{K}_{0,1}$ and $\mathbf{K}_{0,2}$. Different starting points resulted in different solutions for each model. For the Arrhenius and random scission models this is most likely due to the relative flatness of the objective function along the kinetic compensation line. For the radical depolymerization model, it is possible that distinct local minima are being found. In addition to E_2 and $\mathbf{K}^*$, Table 3.3 also includes the zip length for the radical depolymerization solution at a temperature of

600 K—approximately the middle of the reaction. The zip length, $Z \equiv k^d/k^{t1}$, is a measure of the degree to which degradation is dominated by depolymerization.

Arrhenius	$\mathbf{K}_{0,1}$	$\mathbf{K}_1^*$	$\mathbf{K}_{0,2}$	$\mathbf{K}_2^*$
E_2	N/A	0.103	N/A	0.075
A	3.00E+11	4.54E+11	1.00E+15	1.32E+09
E	1.00E+05	1.87E+05	2.50E+05	1.46E+05
ψ	2	1.56	2	1.23
Random Scission	$\mathbf{K}_{0,1}$	$\mathbf{K}_1^*$	$\mathbf{K}_{0,2}$	$\mathbf{K}_2^*$
E_2	N/A	0.189	N/A	0.436
A	5.00E+09	1.43E+08	1.00E+15	5.79E+15
E	1.30E+05	1.12E+05	2.50E+05	2.21E+05
l	0.100	0.100	1.000	5.915
Radical Depoly.	$\mathbf{K}_{0,1}$	$\mathbf{K}_1^*$	$\mathbf{K}_{0,2}$	$\mathbf{K}_2^*$
E_2	N/A	0.138	N/A	0.213
A^i	1.00E+06	1.99E+06	1.32E+13	4.77E+13
E^i	1.01E+05	1.03E+05	2.15E+05	2.19E+05
A^d	4.14E+08	7.62E+08	3.45E+14	2.45E+15
E^d	5.28E+04	4.51E+04	1.65E+05	1.61E+05
A^{t1}	1.04E+14	2.17E+14	1.47E+13	1.44E+13
E^{t1}	9.95E+04	1.04E+05	1.90E+05	1.88E+05
l	1.000	1.092	0.452	0.451
Z ($T = 600$ K)	0.046	0.450	3.52E+03	4.23E+04

Table 3.3: Summary of optimization results for PMMA.

The best solution was found with the Arrhenius model. The numerical simulation of this solution is plotted in Figure 3.9. Evolved gas analysis indicates that PMMA

degrades by the radical depolymerization mechanism. Therefore, it is surprising that this mechanism does not produce a better fit to the data. The fact that PMMA degrades by radical depolymerization should also be evidenced in a large kinetic chain length, Z. The first radical depolymerization solution has a small value for Z. For these reasons, it seems likely that the optimization is only finding local minima.

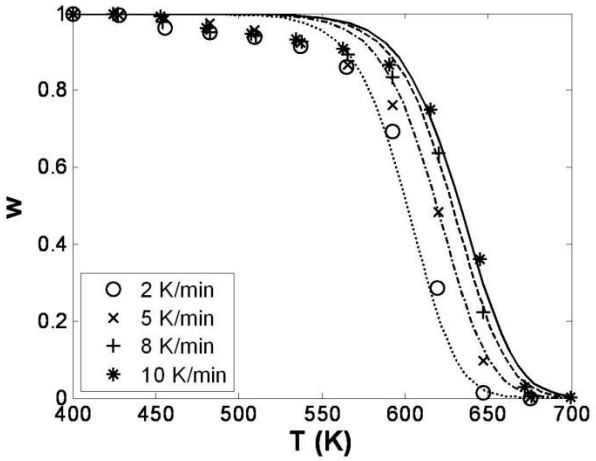

Figure 3.9: Optimal simulation of PMMA dynamic TGA with Arrhenius model and solution $\mathbf{K}_2^*$.

TGA data for the degradation of HDPE were obtained from Conesa et al. (1996). The material had an initial weight-averaged molecular weight of 22,000 g/mol. The data were from dynamic experiments at heating rates of 5, 25, 50, and 100 K/min.

The optimization results are compiled in Table 3.4. The best solution was found using the random scission model. This solution is plotted in Figure 3.10. As with PMMA, changing the starting point resulted in different solutions. Polyethylene is also thought to degrade by the radical depolymerization mechanism, but unlike PMMA, the

depropagation reaction is less dominant due to significant hydrogen transfer rates. Therefore, it should be expected that the random scission and radical depolymerization models perform equally well, and Z should be small. Again, the optimization results do not support these hypotheses.

Arrhenius	$\mathbf{K}_{0,1}$	$\mathbf{K}_1^*$	$\mathbf{K}_{0,2}$	$\mathbf{K}_2^*$
E_2	N/A	0.207	N/A	0.214
A	3.00E+11	3.84E+11	1.00E+18	1.36E+12
E	1.00E+05	2.00E+05	2.75E+05	2.08E+05
ψ	2	1	2	1
Random Scission	$\mathbf{K}_{0,1}$	$\mathbf{K}_1^*$	$\mathbf{K}_{0,2}$	$\mathbf{K}_2^*$
E_2	N/A	0.045	N/A	0.254
A	2.00E+12	9.25E+11	1.00E+18	7.03E+14
E	1.80E+05	1.77E+05	2.75E+05	2.20E+05
l	0.028	0.028	0.140	0.032
Radical Depoly.	$\mathbf{K}_{0,1}$	$\mathbf{K}_1^*$	$\mathbf{K}_{0,2}$	$\mathbf{K}_2^*$
E_2	N/A	0.151	N/A	0.114
A^i	6.00E+13	3.09E+13	1.00E+10	1.06E+13
E^i	2.05E+03	2.06E+05	1.50E+05	2.20E+05
A^d	2.00E+14	9.92E+14	1.00E+10	2.72E+10
E^d	2.00E+05	3.36E+05	1.50E+05	1.18E+05
A^{t1}	2.00E+13	5.07E+15	1.00E+13	4.37E+12
E^{t1}	2.00E+05	2.03E+05	1.50E+05	1.64E+05
l	0.112	0.079	0.280	1.428
Z ($T = 800$ K)	10	4.23E-10	0.001	6.78

Table 3.4: Summary of optimization results for HDPE.

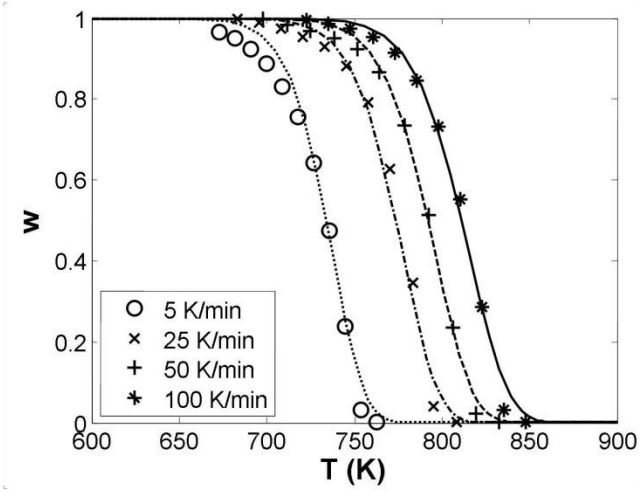

Figure 3.10: Optimal simulation of HDPE dynamic TGA with random scission model and solution $\mathbf{K}_1^*$.

3.4.4 Conclusions

The results of the optimization problem were inconclusive. Although it was found that the calibrated PBE models can accurately predict dynamic TG experiments, unique optimal kinetic parameters were not found. The optimization problem is complicated by the flatness of the objective function in the kinetic compensation regions of the parameter space, and the high dimensionality of the parameter space in the case of the radical depolymerization model. For these reasons, it seems clear that TGA calibrated models are not reliable tools for predicting pyrolysis in a thermally degrading system.

It is worthwhile to compare the results obtained in this chapter for the chain initiation rate of HDPE. The Arrhenius parameters for chain initiation are provided in Figure 3.11 and Table 3.5. The results from this chapter are represented as large markers in Figure 3.11 whereas the remainder of the data was compiled by Ceamanos et al.

(2002). It is found that the corrected gas phase rates determined by Ranzi et al. (1997) seem to lie well off the kinetic compensation line. The estimate of Ranzi et al. seems to be too slow to match typical TGA data. These authors corrected the gas phase activation energy, but it seems that it might also be necessary to make a correction to the gas phase pre-exponential. The RMD and TGA calibrated estimates fall well within the cluster representing the kinetic compensation effect. Despite this, the estimated activation energies differ by 45 kJ/mol. This disparity gives further justification for the need for improved models of pyrolysis mechanisms and rates.

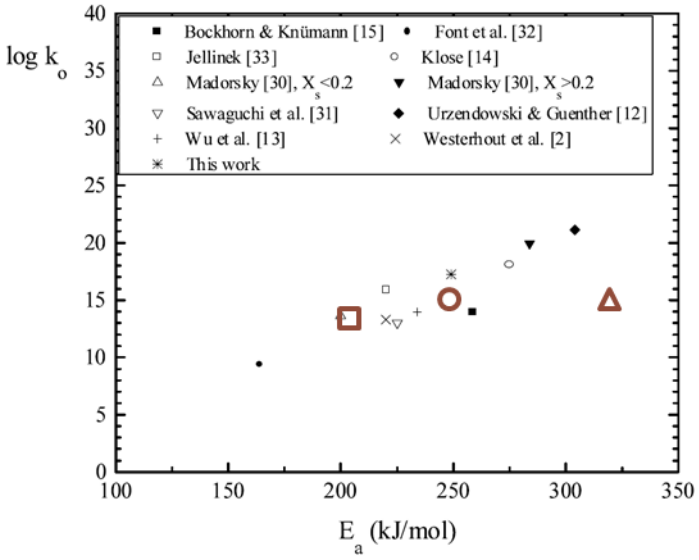

Figure 3.11: Chain initiation parameters for HDPE. The plot is from Ceamanos et al. (2002). The small markers represent Arrhenius parameters estimated from various literature sources. The large markers represent estimates based on a gas phase analogy (Δ), RMD with $i = 200$ (○), and calibration with TGA data (□).

	$\log A\ (\mathrm{s}^{-1})$	$E\ (\mathrm{kJ/mol})$
Ranzi et al. (1997) (Δ)	14.9	321
RMD, $i = 200$ (○)	14.6	251
TGA Calibration (□)	13.5	206

Table 3.5: Chain initiation kinetic parameters for HDPE obtained by three different methods.

The rest of this dissertation is directed towards improving physics-based modeling of thermal degradation. In the next chapter, approximate numerical methods for solving PBE equations are discussed.

4: Numerical Solutions to Kinetic Equations

One value of using the PBE formalism for modeling the mesoscale population dynamics is that it provides a framework for rapidly testing pyrolysis mechanisms. Another advantage is that there are several methods available for rapidly solving PBEs. In the previous chapter, moment methods were used to solve PBEs. Moment methods are fast and useful for scenarios such as TGA in which only global information is needed. When more complex physical processes, such as those encountered in DSC and ignition, detailed information about the chemical composition of the melt and pyrolysis gas is needed.

4.1 BACKGROUND

Numerical solutions of population balance equations (PBEs) are typically obtained by moment methods or Monte Carlo simulations (Ramkrishna, 2000). The first approach is fast, but it results in a coarse description of the number density function. The second approach provides detailed information about the evolution of the number density function, but it can be prohibitively expensive.

Many quantities of interest are directly proportional to integer moments of the number density function. For problems in which the moments are global (over the entire size domain), the method of moments (MOM) is appropriate. The standard MOM is obtained by applying the moment operator to the PBE to obtain a set of ODEs in terms of some small number of global moments. In most problems the resultant equations are

unclosed. To overcome this limitation, the quadrature method of moments (QMOM) was introduced by McGraw (1997). In the QMOM, the unclosed terms are approximated by Gaussian quadrature. The quadrature weights and nodes are derived from the moments being evolved. The direct quadrature method of moments (DQMOM) (Fox, 2003) is similar to the QMOM. In the DQMOM, the quadrature weights and nodes are the dependent variables of the system of ODEs. In addition to being more computationally tractable, the DQMOM has the distinct advantage of being more readily extendable to multivariate PBEs.

A promising alternative to these approaches are discrete methods. Discrete methods partition the internal coordinate domain into sections. The PBE is then transformed to a set of ODEs describing the evolution of sectional quantities such as the total mass within each section. The primary advantage of discrete methods is that they allow the user to focus computational effort on specific properties within specific regions of the internal coordinate domain.

Kumar and Ramkrishna (1996a) provide a thorough overview and comparison of various discrete methods. Many of the proposed methods are *ad hoc* and limited to specific grids or specific forms of the PBE. The moving pivot technique of Kumar and Ramkirhsna (1996b) evolves any two arbitrary distribution properties for each section—e.g., number and mass. The moving pivot technique was a natural extension of their fixed pivot technique (Kumar and Ramkrishna, 1996a). Underlying both pivot approaches is a representation of the number density function as a delta function within each section. The

pivot refers to the location of the delta function within the section in the size domain. It was found that by allowing the pivot to move, more accurate results could be obtained for problems in which the number density function was heavily weighted towards one end of some of the sections.

A more recent review of discrete methods is found in Vanni (2000). The author compared many of the methods produced in the literature on 10 test cases with varying models for breakage and aggregation. Only discrete distributions, in which all particles are integer multiples of the smallest particle, were considered. Consequently, they were unable to test the moving pivot technique of Kumar and Ramkrishna. Nevertheless, it was concluded that the fixed pivot method was the most robust, versatile, and easily implemented of all of the approaches considered.

In this chapter, a generalization of the moving pivot technique is presented. Specifically, it is shown how to include any number of arbitrary distribution properties, as opposed to just two, within each section. The generalization is achieved by using the ideas of the DQMOM. A similar method derived from the QMOM is possible, but it was found to be relatively slow and numerically unstable. In addition, the DQMOM is more readily extended to multivariate distributions than QMOM. Because it combines elements of sectional and moment algorithms, the method presented in this chapter will be referred to as the hybrid sectional MOM (HySMOM).

The development is limited to PBEs for breakage and aggregation, but the framework is general enough to include convection and diffusion within the internal

coordinate space. Many engineering problems are dominated by the dynamics of breakage and aggregation such as polymerization-depolymerization, liquid drop coalescence and breakup, soot evolution, and the colloidal suspensions. Other source terms such as nucleation could be included. The purpose here is to present and verify the HySMOM for a fairly general class of PBEs. After discussing the form of the breakage/aggregation PBE, the HySMOM technique is derived. Finally, numerical results are presented for four test cases.

It will be convenient to rewrite the PBE of Equation (2.19). In the case of binary breakage and aggregation, the PBE is

$$\frac{\partial f}{\partial t} = B[x, f(x,t)] + A[x, f(x,t)], \tag{4.1}$$

where the breakage and aggregation terms are defined by

$$B[x, f(x,t)] \equiv 2\int_x^\infty dx'\, b(x')P(x|x')f(x') - b(x)f(x), \tag{4.2a}$$

$$\begin{aligned} A[x, f(x,t)] = \frac{1}{2}\int_0^x dx'\, a(x-x', x')f(x-x')f(x') \\ - f(x)\int_0^\infty dx'\, a(x,x')f(x'). \end{aligned} \tag{4.2b}$$

Solution of Equation (4.1) requires the specification of the initial number density function, $f_0(x)$. Analytical solutions are available for only a small number of cases with simple functional forms for the breakage rate, breakage probability, aggregation rate, and initial distribution. For realistic problems these simplified forms will not be valid. It is

therefore necessary to have a robust, and preferably fast, approximate method that accurately predicts the critical properties of the number density function.

4.2 DEVELOPMENT OF THE METHOD

In this section, a numerical approach is presented for solving Equation (4.1). The structure of this method can be outlined as follows. First, attention is focused on the distribution properties that are of most interest to the user. This focus is achieved by discretizing the domain into N arbitrary sections. Within each section, the number density function is represented by a small number of delta functions. The PBE is then transformed to a set of ODEs governing the location and magnitude of the delta functions within each section. A brief comparison between the HySMOM and similar methods is included. The error associated with the proposed method is primarily due to Gaussian quadrature error. Some general remarks about this error are made, and the specific case of error for pure random breakage is examined in detail.

4.2.1 Quantities of Interest

The ideal numerical method for solving PBEs would predict the entire number density function at all times. This is the motivation for using Monte Carlo simulations to solve PBEs. Since Monte Carlo is prohibitively expensive in many applications, effort should be focused on the properties of the system that are of most interest to the user. These properties will be referred to as quantities of interest. Many quantities of interest are integrals of the number density function. In experimental science, transducers have

limited resolution and so what is actually measured is an average of some property over many particles (or events). In engineering, integral quantities are typically used to quantify performance. Often, the integrated quantities of interest are global such as the total mass or total number of particles present in some control volume. In many situations, however, the quantities of interest are integrated over a limited region of the internal coordinate space. For instance, an air quality specialist might be interested in the total mass of particles within a hazardous size range.

A general principle for numerical solutions of PBEs is to *find a sufficiently accurate estimate of the quantities of interest with minimal computational time*. This principle suggests a discretization of the domain that is fine in the regions of the quantities of interest but coarse everywhere else. In other words, the numerical method should be tailored to the quantities of interest. To this end, many authors (e.g., Gelbard et al., 1980; Kumar and Ramkrishna, 1996a) begin their development of discrete methods by introducing integral quantities of interest of the form

$$Q_i(t) \equiv \int_{I_i} q(x) f(x,t) dx, \tag{4.3}$$

where $q(x)$ is the value of some extensive property associated with a single particle of size x. As a concrete example, suppose that x denotes a spherical particle radius. If one is interested in the mass of particles in a hazardous radius interval (r_L, r_U) then the primary quantity of interest is

$$Q(t) = \int_{r_L}^{r_U} \left[\frac{4}{3}\pi x^3 \rho\right] f(x,t)dx, \tag{4.4}$$

where ρ is the mass density of the particles. Of course $Q(t)$ will depend on the dynamics of the number density function in other size ranges, but it is not necessary to resolve these size ranges any more finely than is necessary to obtain an accurate prediction of $Q(t)$.

Note that the quantity of interest in Equation (4.4) is directly proportional to the third moment of the distribution within the interval. Quantities of interest can often be specified to depend on sectional moments. Therefore, in this chapter, attention is limited to sectional moments as the quantities of interest. In the next section, the sectional notation is introduced.

4.2.2 Domain Discretization

The following conventions will be used in the remainder of this paper. The size domain is partitioned into the intervals, $I_i \equiv [X_i, X_{i+1})$ for $i = 1, \ldots, N$. A section's width will be denoted $\Delta_i \equiv X_{i+1} - X_i$. The smallest section bound must be positive since particles must have positive mass. Furthermore, mass conservation requires that $X_1 = 0$, otherwise particles being generated of size $x < X_1$ would be incorrectly removed from the population. Additionally, X_{N+1} must be sufficiently large so that there is negligible mass in the region $x \geq X_{N+1}$ at all simulation times.

Two grid schemes, uniform and geometric, will be used in the following. The uniform grid is characterized by $\Delta_i = constant$ for all i or $X_{i+1} = iX_2$ for $i > 1$. This description requires the specification of the section width and the number of sections. For

geometric grids, the section boundaries are computed by $X_{i+1} = gX_i$ for $i > 2$. The two geometric grid parameters are the expansion rate, g, and the width of the first section, $\Delta_1 = X_2$.

4.2.3 Discretized Form of the Number Density Function

A discretized description of the number density function is needed that preserves the integral quantities of interest. A convenient representation arises from Gaussian quadrature. The integral for the quantity of interest can be approximated by Gaussian quadrature using the relation

$$\int_I q(x)f(x,t)dx = \sum_{p=1}^{M} w_p q(x_p) + E, \tag{4.5}$$

where x_p and w_p are the quadrature nodes and weights. The selection of the nodes and weights depend upon the weighting function which in this case is the number density function. As the number density function evolves, so will the nodes and weights. For a given number density function and interval, the weights and nodes can be computed using orthogonal polynomials (Press and Teukolsky, 1990).

Unfortunately, the orthogonalization algorithms used for Gaussian quadrature cannot be used if the weight function, in this case $f(x,t)$, is unknown. The usefulness of the approximation in Equation (4.5) is through its equivalence with the assumption that the number density function is represented by a sum of delta functions. Thus, if M pivots are allowed within each section, then the total distribution can be approximated by

$$f(x) \approx \sum_{p=1}^{N\times M} w_p \delta(x - x_p). \tag{4.6}$$

Each quadrature node remains in a single section for all times: $x_p \in I_i$ where $i = \lceil p/M \rceil$—the notation $\lceil \cdot \rceil$ represents the ceiling function. Alternatively, each section will contain the same nodes for all times. The nodes in section i are the set $\{x_{(i-1)M+1}, \ldots, x_{Mi}\}$. This delta function approximation can be thought of as representing a continuous function with a set of infinitely sharp peaks as in Figure 2.

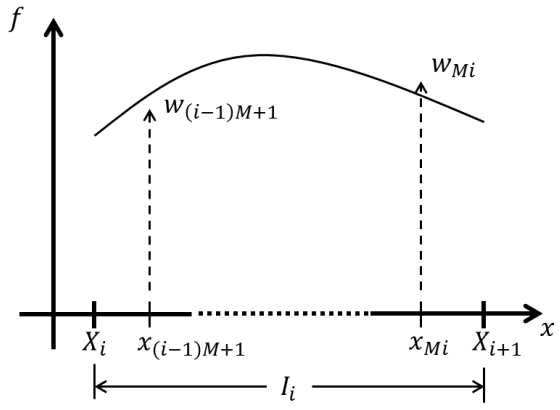

Figure 4.1: The first and last quadrature points in the discrete representation of the number density function within interval i.

The influence that each quadrature node has on the overall PBE is independent of which section it is located in. The sectional location of any node is important only in the relationship between each node and the quantity of interest that it influences. This does not mean that the section boundaries are unimportant, though. In fact, without the constraint of the section boundaries, the numerical solution would not generally give accurate estimates of the local quantities of interest. In effect, the section boundaries

force the numerical solution to focus its limited resources on the regions that are of most interest to the user. For this reason, the approach presented here has many advantages over the standard DQMOM.

By substituting Equation (4.6) into Equations (4.1) and (4.2), the integral terms are replaced by summations resulting in

$$\frac{\partial f}{\partial t} \approx \sum_p \left[\delta(x - x_p) + \delta'(x - x_p)x_p\right]\frac{dw_p}{dt} - \sum_p \delta'(x - x_p)\frac{d\xi}{dt}, \tag{4.7a}$$

$$B(x) \approx 2\sum_{p:x_p>x} w_p b(x_p) P(x|x_p) - b(x)\sum_p w_p \delta(x - x_p), \tag{4.7b}$$

$$\begin{aligned} A(x) \approx \frac{1}{2}\sum_{p:x_p<x}\sum_q w_p w_q a(x - x_p, x_p)\delta(x - x_p - x_q) \\ - \sum_p \sum_q w_p w_q a(x, x_p)\delta(x - x_q), \end{aligned} \tag{4.7c}$$

where $\xi_p \equiv w_p x_p$ and $\delta' \equiv d\delta/dx$. The quantities ξ_p are weighted quadrature nodes, and they are introduced because they result in a simpler form in the final ODEs.

These equations are unhelpful until the delta functions are integrated out. This is accomplished by introducing the integral quantities of interest. As will be shown in the next section, these properties are associated with integral operators that can be applied to Equations (4.7) to obtain a closed form of the approximate PBE in terms of the quadrature points and weights.

4.2.4 HySMOM

In this section, it is shown how the DQMOM can be applied to discretized solutions of PBEs. First, note that moment methods can be generalized by considering *sectional moments*. Sectional moments are moments over a subspace of the internal coordinate domain defined by

$$\mu_i^{(k)}(t) \equiv \int_{I_i} x^k f(x,t) dx. \tag{4.8}$$

Applying the operation used in Equation (4.8) to Equations (4.7) gives the following closed system of ODEs

$$(1-k) \sum_{p:x_p \in I_i} x_p^k w_p' + k \sum_{p:x_p \in I_i} x_p^{k-1} \xi_p' = \sigma_i^{(k)}, \tag{4.9}$$

where w_p' and ξ_p' are the time derivatives of the quadrature weights and weighted nodes, and $\sigma_i^{(k)} \equiv \beta_i^{(k)} + \alpha_i^{(k)}$ is the net rate of production of the k^{th} moment in section i. This production is distributed between the time derivatives according to the left-hand side of Equation (4.9).

The moment weighted breakage and aggregation rates are computed by

$$\begin{aligned} \beta_i^{(k)} &\equiv \int_{I_i} x^k B(x) dx \\ &\approx 2 \sum_{p:\, x_p \geq X_i} \Pi_i^{(k)}(x_p) w_p b(x_p) - \sum_{p:\, x_p \in I_i} x_p^k w_p b(x_p). \end{aligned} \tag{4.4.10}$$

where

$$\Pi_i^{(k)}(x_p) \equiv \begin{cases} \int_{I_i} x^k P(x|x_p)dx, & x_p \geq X_{i+1} \\ \int_{X_i}^{x_p} x^k P(x|x_p)dx, & x_p \in I_i \end{cases}. \tag{4.11}$$

Similarly, for aggregation

$$\begin{aligned} \alpha_i^{(k)} &\equiv \int_{I_i} x^k A(x)dx \\ &\approx \sum_{\substack{p,q:\, x_p \geq x_q \\ x_p + x_q \in I_i}} \left(1 - \frac{1}{2}\delta_{pq}\right) w_p w_q a(x_p, x_q) \left(x_p + x_q\right)^k \\ &- \sum_{p,q:\, x_q \in I_i} w_p w_q a(x_p, x_q)\, x_q^k, \end{aligned} \tag{4.12}$$

where δ_{pq} is the identity matrix. The computations involved in evaluating the source terms are straightforward with the exception of the integrals in Equation (4.11). Integrals of this type appear in all discretized methods. Fortunately, for many forms of the breakage probability, the integrals can be evaluated analytically.

It is important to verify that these approximations obey conservation of mass. Mass is conserved if the summation over all sections of the moment weighted rates both sum to zero. Summing Equation (4.4.10) over the index i with $k = 1$ gives

$$\sum_i \beta_i^{(1)} = \sum_p w_p b(x_p) \left(2\int_0^{x_p} xP(x|x_p)dx - x_p\right). \tag{4.13}$$

Mass conservation requires that

$$x_p = 2\int_0^{x_p} xP\left(x\middle|x_p\right)dx. \tag{4.14}$$

This equation is a standard constraint on the breakage probability for binary breakage (Ramkrishna (2000)), and so mass is conserved for breakage. Conservation of mass for the aggregation processes can be confirmed by summing Equation (4.12) over all values of i with $k = 1$, changing orders of summation and using the symmetry property of the aggregation rate, $a\left(x_p, x_q\right) = a\left(x_q, x_p\right)$.

Evolution of the sectional weights and weighted nodes requires solving Equation (4.9) for the time derivatives of these quantities. Since there are $2M \times N$ unknowns, w_p' and ξ_p', it is necessary to have $2M$ moment sources per section. Using the first $2M$ moments requires evaluation of the sequence $\sigma_i^{(0)}, \ldots, \sigma_i^{(2M-1)}$. The algebraic problem can be formulated as a $2M \times 2M$ linear system for each section. That is, for a given section (or fixed i), the left-hand side of Equation (4.9) contains $2M$ unknowns. For each moment order, k, there exists an independent equation relating these unknowns. Thus, a system of $2M$ moment equations in terms of these $2M$ unknown quadrature weights and weighted nodes may be written in matrix form as

$$\mathbf{D}_i(\mathbf{w}, \boldsymbol{\xi}) \begin{bmatrix} \mathbf{w}_i' \\ \boldsymbol{\xi}_i' \end{bmatrix} = \boldsymbol{\sigma}_i(\mathbf{w}, \boldsymbol{\xi}), \tag{4.15}$$

where $\mathbf{w}_i \equiv \left[w_{M(i-1)+1} \cdots w_{Mi}\right]^T$, $\boldsymbol{\xi}_i \equiv \left[\xi_{M(i-1)+1} \cdots \xi_{Mi}\right]^T$, $\mathbf{w} \equiv [\mathbf{w}_1 \cdots \mathbf{w}_N]$, $\boldsymbol{\xi} \equiv [\boldsymbol{\xi}_1 \cdots \boldsymbol{\xi}_N]$ and $\boldsymbol{\sigma}_i \equiv \left[\sigma_i^{(0)} \cdots \sigma_i^{(2M-1)}\right]^T$. The matrix on the left-hand side of Equation (4.15) accounts for the coefficients on the left-hand side of Equation (4.9) and effectively

distributes the source between the time derivatives of the quadrature weights and nodes. For a one-point quadrature, this matrix is

$$\mathbf{D}_i = \begin{bmatrix} 1 & 0 \\ 0 & 1 \end{bmatrix}. \tag{4.16}$$

For a two-point quadrature,

$$\mathbf{D}_i = \begin{bmatrix} 1 & 1 & 0 & 0 \\ 0 & 0 & 1 & 1 \\ -x_{2i-1}^2 & -x_{2i}^2 & 2x_{2i-1} & 2x_{2i} \\ -2x_{2i-1}^3 & -2x_{2i}^3 & 3x_{2i-1}^2 & 3x_{2i}^2 \end{bmatrix}. \tag{4.17}$$

The quadrature points are evolved by inverting Equation 18 at each time step

$$\begin{bmatrix} \mathbf{w}_i' \\ \boldsymbol{\xi}_i' \end{bmatrix} = \mathbf{D}_i^{-1} \boldsymbol{\sigma}_i. \tag{4.18}$$

If $N = 1$, Equation (4.18) reduces to the standard DQMOM for breakage and aggregation. One difficulty of the DQMOM is that $\mathbf{D}_i$ becomes singular if two or more quadrature points come together. For the test cases considered in this chapter, this was not a problem. Marchisio and Fox (2005) suggest that perturbations to the quadrature points can be used to overcome this difficulty if it arises.

4.2.5 Comparison to Other Discrete Methods

All discrete methods require applying sectional integration operators to the PBE. Kumar and Ramkrishna (1996a) make a helpful distinction between two classes of discrete methods. The distinction results from different applications of the mean value theorem to the integral terms arising in the integrated PBE. For example,

$$\int_{I_i} g(x)f(x,t)dx = \begin{cases} g(x_a)\int_{I_i} f(x,t)dx\,, \\ f(x_b,t)\int_{I_i} g(x)dx\,, \end{cases} \tag{4.19}$$

where $x_a, x_b \in I_i$. The advantage of using the first line of Equation (4.19) is that the integral is just the number of particles within the section, which is likely to be a quantity of interest. The difficulty in this class of methods is determining the pivot x_a. The advantage of using the second line of Equation (4.19) is that the remaining integral term is constant with time. The difficulty in this approach is approximating $f(x_b,t)$ since the number density function is unknown.

A survey of the literature on discrete methods before 1996 is provided by Kumar and Ramkrishna (1996a). The authors make three conclusions from this body of literature. First, methods based on the first line of Equation (4.19) are computationally more efficient. Second, accuracy increases with grid resolution. And third, methods that evolve both numbers, $\mu_i^{(0)}$, and mass, $\mu_i^{(1)}$ are more accurate. Improvements in this body of literature have generally been toward including additional physics, allowing for more general grids, and increasing accuracy. The moving pivot technique of Kumar and Ramkrishna (1996b) is fast and general, but it is limited to solutions in which only two properties (e.g., mass and number) per section are evolved. The method presented in this paper is a generalization of the moving pivot technique.

The HySMOM is based on a generalization of the first line of Equation (4.19) in which an arbitrary number of properties (in this case, moments) can be evolved. This

generalization is a consequence of noting that the first line of Equation (4.19) is a one point Gaussian quadrature. For a M point Gaussian quadrature, the integral approximation has the form of Equation (4.5) which is the approximation that has been employed in this paper. Gaussian quadrature is exact for polynomials of degree $2M-1$ or less, a class that includes the first $2M$ integer moments. The case of $M=1$, corresponds to the moving pivot technique of Kumar and Ramkrishna with sectional numbers and weights as the evolved quantities. Before continuing to some numerical results, a few words on numerical errors are in order.

4.2.6 Errors in HySMOM

The discretization errors for the approximate solution of the PBE can be broken into two parts. First, there is the error associated with the time integration that is primarily controlled by the time step size. The second source of error is the error associated with computing the right-hand side of the system of ODEs. This error is due to the quadrature rule used to approximate the integral terms in Equations (4.2). In the following, some remarks are made on this quadrature error.

4.2.6.1 Gaussian Quadrature Error

Any Gaussian quadrature can be written as Equation (4.5). The quadrature nodes (or abscissas), x_p, are the zeros of an M^{th} degree polynomial from a sequence of mutually orthogonal (with respect to the weight function, $f(x)$) polynomials

$\{p_0, p_1, \ldots, p_M\}$. If the sequence of polynomials is monic (the leading coefficient is one), then the error in Equation 22 is (Ralston and Rabinowitz, 2001)

$$E = \frac{\gamma_M}{(2M)!} \left. \frac{d^{2M} q}{dx^{2M}} \right|_{\eta}, \tag{4.20}$$

where $\eta \in I$, and

$$\gamma_M \equiv \int_I f(x) p_M^2(x) dx. \tag{4.21}$$

From Equations (4.5) and (4.20) it is clear that the quadrature is exact if $q(x)$ is a polynomial of degree less than or equal to $2M - 1$. Since the integrands associated with moment methods for solutions of PBEs are often not low order polynomials, there will be some error associated with the curvature of the integrand $q(x)$.

In addition to the quadrature error due to the curvature of the integrand is the error due to the discrete representation of the number density function. This error is the ratio $\varepsilon_M \equiv \gamma_M/(2M)!$. In order to better understand this term, it is helpful to see how it relates to the moments of the distribution. For the case of $M = 1$, the orthogonal polynomials are related to the moments through (Press and Teukolsky, 1980)

$$p_1 = x - \mu^{(1)}/\mu^{(0)}, \tag{4.22}$$

and so

$$\gamma_1 = \mu^{(2)} - \left[\mu^{(1)}\right]^2/\mu^{(0)}. \tag{4.23}$$

Note that γ_1, and thus the error, is zero if all of the particles in the distribution are the same size. In this case, the exact distribution is equal to its delta function approximation.

To better see this, observe that $\gamma_1 = 0$ when $\mu^{(2)}/\mu^{(1)} = \mu^{(1)}/\mu^{(0)}$—the weight average size equals the number average size. Also the error estimate depends on a quantity, $\mu^{(2)}$, that is outside of the space of exactly predicted polynomials since a one point quadrature is exact for polynomials of degree less than or equal to one. This class includes the first moment but not the second. In other words, the error estimate depends on information not available in the approximate solution.

For higher order quadratures, it is apparent from Equation (4.21) that $\gamma_M = 0$ if and only if the number density function is only non-zero at the quadrature nodes since these are the zeros of p_M. The distribution error, ε_M, is minimized if the number density function is small in regions away from the quadrature nodes. Thus errors will be large in cases where $f(x)$ has more peaks than quadrature nodes. Also, ε_M will decrease with M since the function $p_M^2(x)$ will be close to zero over a larger portion of the domain of integration.

If the number density function is approximately constant over the interval, $f(x) = \tilde{f}$, then the quadrature is directly proportional to Gauss-Legendre quadrature ($f(x) = 1$) for which (Ralston and Rabinowitz, 2001)

$$\varepsilon_M = \frac{2^{2M+1}(M!)^4}{(2M+1)[(2M)!]^3}\tilde{f}. \tag{4.24}$$

The case of constant $f(x)$ over the interval is the case that will be approached as the number of sections becomes large. Thus in regions where the number density function is

constant, the error decreases rapidly with M. For first, second, and third order quadratures, $\varepsilon_1 = \tilde{f}/3$, $\varepsilon_2 = \tilde{f}/135$, $\varepsilon_3 = \tilde{f}/15{,}750$, and $\varepsilon_4 = \tilde{f}/3{,}472{,}875$.

4.2.6.2 Approximate Error Bounds for Pure Random Breakage

For certain special cases, it is possible to estimate error bounds for the HySMOM. The focus of the following will be on predicting the errors in the time rate of change of the sectional moments. This error is magnified by errors in the time integration, but it is ultimately the quadrature that introduces error into the approximate solution. The error of interest is found by applying the sectional moment operator to the right-hand side of Equation (4.2a). Similar analysis could be performed for the approximation to the aggregation terms in Equation (4.2b). For the case of pure breakage,

$$\frac{d\mu_i^{(k)}}{dt} = 2\int_{X_i}^{\infty} b(x')\Pi_i^{(k)}(x')f(x')dx' - \int_{I_i} x^k b(x)f(x)dx. \tag{4.25}$$

By comparison with Equation (4.4.10), it is apparent that two Gaussian quadratures are being applied, the first associated with production and the second with loss

$$E_{1,i}^{(k)} \equiv 2\left[\int_{X_i}^{\infty} b(x')\Pi_i^{(k)}(x')f(x')dx' - \sum_{p:\, x_p \geq X_i} \Pi_i^{(k)}(x_p)b(x_p)w_p\right], \tag{4.26a}$$

$$E_{2,i}^{(k)} \equiv \left[\int_{I_i} x^k b(x)f(x)dx - \sum_{p:\, x_p \in I_i} x_p^k w_p b(x_p)\right]. \tag{4.26b}$$

The errors depend on the integrands

$$q_{1,i}^{(k)}(x) \equiv b(x)\Pi_i^{(k)}(x), \tag{4.27a}$$

$$q_{2,i}^{(k)}(x) \equiv x^k b(x). \tag{4.27b}$$

For the case of pure random breakage, $b(x) = b_o x$ and $P(x|x') = 1/x'$. For convenience, the breakage rate constant will be subsumed into the time variable so that the error bounds will correspond to $d\mu_i^{(k)}/d\tau$ where $\tau \equiv b_o t$.

The weighted breakage probability has the analytical form

$$\Pi_i^{(k)}(x) = \frac{1}{x}\int_{X_i}^{\min(x,X_{i+1})} x'^k dx' = \frac{1}{x}\frac{[\min(x, X_{i+1})]^{k+1} - X_i^{k+1}}{k+1}, \tag{4.28}$$

and so the integrands associated with the quadrature error due are

$$q_{1,i}^{(k)}(x) = \frac{1}{k+1}\left\{[\min(x, X_{i+1})]^{k+1} - X_i^{k+1}\right\}, \tag{4.29a}$$

$$q_{2,i}^{(k)}(x) \equiv x^{k+1}. \tag{4.29b}$$

The next step in estimating the error is to compute the curvature of the integrands. The $2M^{th}$ derivatives of Equations (4.29) are

$$\left.\frac{d^{2M} q_{1,i}^{(k)}}{dx^{2M}}\right|_x = \begin{cases} \dfrac{1}{k+1} C_{M,k} x^{k-2M+1}, & x < X_{i+1}, \\ 0, & x > X_{i+1} \end{cases} \tag{4.30a}$$

$$\left.\frac{d^{2M} q_{2,i}^{(k)}}{dx^{2M}}\right|_x = C_{M,k} x^{k-2M+1}, \tag{4.30b}$$

where the coefficients are defined as

$$C_{M,k} \equiv \prod_{r=1}^{2M}(k - r + 2). \tag{4.31}$$

Finally, in order to estimate error bounds, it is necessary to find the maximum and minimum values of Equations (4.30) in the appropriate domains of integration. For the production term, the integral is over the interval $[X_i, \infty)$, and so the minimum error will always be zero according to the second line in Equation (4.30a). The maximum error for the low order moments ($k < 2M - 1$) will always be zero due to the product coefficient, Equation (4.31). Since the product coefficient and the exponent on x are both positive, the maximum error will always correspond to $x = X_{i+1}$ so that the error bounds associated with the first term (production) in the breakage equation are

$$0 \leq E_{1,i}^{(k)} \leq \frac{\varepsilon_{M,i}}{k+1} C_{M,k} X_{i+1}^{k-2M+1}, \qquad k \geq 2M-1, \tag{4.32a}$$

$$E_{1,i}^{(k)} = 0, \qquad k \leq 2M-2. \tag{4.32b}$$

Similar bounds can be obtained for the error associated with the second term (loss) in the breakage equation. Again, from Equations (4.30b) and (4.31), the quadrature is exact if $k \leq 2M - 2$. Unlike the error associated with the production term, the lower bound for the loss error is not necessarily zero. The bounds are found by considering the maximum and minimum values of Equation (4.30b) over the domain of integration. In this case, the domain of integration is I_i. Equation (4.30b) is always increasing with increasing x. Therefore, the error bounds associated with loss due to breakage may be summarized as

$$\varepsilon_{M,i} C_{M,k} X_i^{k-2M+1} \leq E_{2,i}^{(k)} \leq \varepsilon_{M,i} C_{M,k} X_{i+1}^{k-2M+1}, \qquad k \geq 2M-1, \tag{4.33a}$$

$$E_{2,i}^{(k)} = 0, \qquad k \leq 2M-2. \tag{4.33b}$$

The total sectional quadrature error associated with random breakage is $E_i^{(k)} \equiv E_{1,i}^{(k)} + E_{2,i}^{(k)}$ so adding Equations (4.32) and (4.33) yields

$$\varepsilon_{M,i} C_{M,k} X_i^{k-2M+1} \leq E_i^{(k)} \leq \left(\frac{k+2}{k+1}\right) \varepsilon_{M,i} C_{M,k} X_{i+1}^{k-2M+1}, \qquad k \geq 2M-1, \quad (4.34a)$$

$$E_i^{(k)} = 0, \qquad k \leq 2M-2. \quad (4.34b)$$

These bounds increase with moment order, k, and decrease with quadrature order, M. The total sectional error also depends on the sectional boundaries.

In order to better grasp these error dependencies, a special case is considered. It is assumed that the number density function is approximately constant within each section so that $f(x) = f_i$ for all $x \in I_i$. The exact sectional moments are then given by

$$\mu_i^{(k)} = \frac{f_i}{k+1}\left(X_{i+1}^{k+1} - X_i^{k+1}\right). \quad (4.35)$$

If the errors in time derivatives of the sectional moment are normalized by the sectional moments, then the upper bound on the relative error is given by the inequality

$$\tilde{E}_i^{(k)} \equiv \frac{E_i^{(k)}}{\mu_i^{(k)}} \leq \frac{(k+2)\varepsilon_{M,i} C_{M,k} X_{i+1}^{-2M}}{f_i\left(1-\chi_i^{k+1}\right)}, \quad (4.36)$$

where the new parameter $\chi_i \equiv X_i / X_{i+1}$ measures the relative section width—that is, $\chi_i \ll 1$ for large sections, and $\chi_i \to 1$ for small sections. For a geometric grid with expansion parameter g, all of the sections have the same relative width, $\chi_i = 1/g$. Since it is assumed that the number density function is approximately uniform within the sections, Equation (4.24) may be used for the distribution error, $\varepsilon_{M,i}$. The maximum

relative errors in the time derivatives of the sectional moments for a geometric grid with $g = 2$ are written in Table 4.1.

Moment Order	Quadrature Order			
	$M = 1$	$M = 2$	$M = 3$	$M = 4$
$k = 0$	0	0	0	0
$k = 1$	$2.67X_{i+1}^{-2}$	0	0	0
$k = 2$	$9.14X_{i+1}^{-2}$	0	0	0
$k = 3$	$21.3X_{i+1}^{-2}$	$0.948X_{i+1}^{-4}$	0	0
$k = 4$	$41.3X_{i+1}^{-2}$	$5.51X_{i+1}^{-4}$	0	0
$k = 5$	$71.1X_{i+1}^{-2}$	$19.0X_{i+1}^{-4}$	$0.325X_{i+1}^{-6}$	0
$k = 6$	$113X_{i+1}^{-2}$	$50.2X_{i+1}^{-4}$	$2.58X_{i+1}^{-6}$	0
$k = 7$	$169X_{i+1}^{-2}$	$112X_{i+1}^{-4}$	$11.6X_{i+1}^{-6}$	$0.105X_{i+1}^{-8}$
$k = 8$	$240X_{i+1}^{-2}$	$224X_{i+1}^{-4}$	$38.5X_{i+1}^{-6}$	$1.05X_{i+1}^{-8}$

Table 4.1: Maximum relative errors for random breakage on a geometric grid with $g = 2$.

Inspection of Table 4.1 reveals the advantage of using higher order methods within a section. Not only are the number of exactly predicted rates increased with M, but also the approximate rates are increasingly accurate with quadrature order. Another interesting feature of Table 4.1 is the exponential dependence of the maximum error on

the sectional upper bound. Larger sections are relatively more accurate. This is likely an artifact of the assumption of constant number density within each section.

4.3 NUMERICAL RESULTS

In order to validate the HySMOM algorithm, numerical results were compared to four analytical solutions from the literature. The four cases are: (1) pure breakage, (2) constant kernel aggregation, (3) additive kernel aggregation, and (4) combined constant breakage and constant aggregation. The section will conclude with an example comparing the standard DQMOM to the HySMOM.

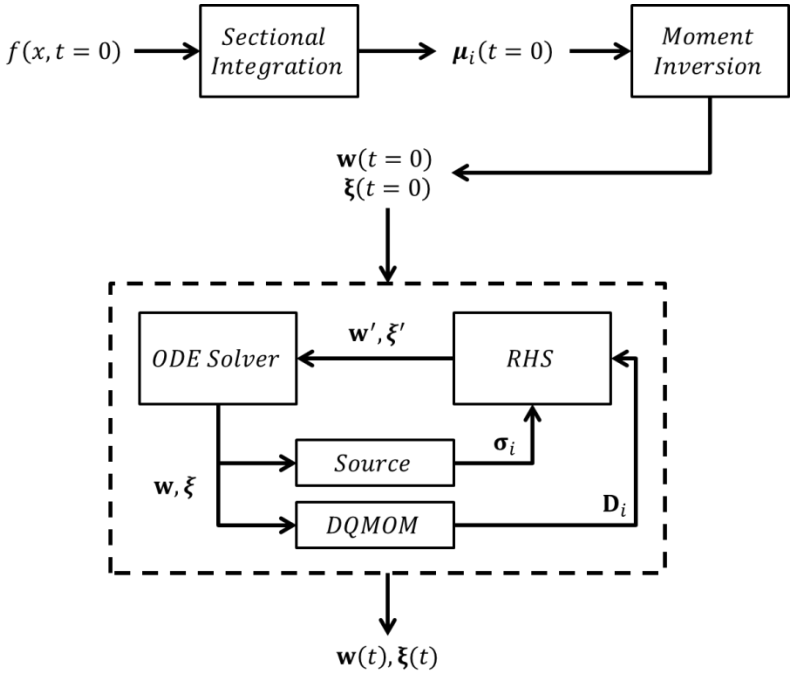

Figure 4.2: Schematic of the HySMOM code structure. The code elements within the dashed line represent the core of the algorithm.

The algorithm was implemented according to the computational procedure sketched in Figure 4.2. Since the ODEs of Equation (4.18) are in terms of the quadrature weights and weighted nodes, the initial values of these quantities must be computed from the initial distribution. This process is done in two steps. First, the sectional moments are computed by piecewise integration of the initial number density function. Second, the initial quadrature weights and weighted nodes are derived from the sectional moments. For one and two point quadratures, there are simple analytical expressions for this calculation. For higher-order quadratures, the weights and nodes can be determined from the eigenvalues and eigenvectors of the Jacobi matrix (Press and Teukolsky, 1990) whose elements can be computed by the product-difference algorithm (Gordon, 1968). In this chapter, only one and two point quadratures are used. Once the initial quadrature weights and weighted nodes are known, the core of the HySMOM algorithm is implemented. The algorithm is contained within the dashed line in Figure 4.2. For given values of $\mathbf{w}$ and $\boldsymbol{\xi}$, the source, $\boldsymbol{\sigma}_i$, and the DQMOM matrix, $\mathbf{D}_i$, may be computed for each section. These quantities allow for the solution of the time rates of change of the weights and weighted nodes. The preceding procedure, relating $\mathbf{w}$ and $\boldsymbol{\xi}$ to $\mathbf{w}'$ and $\boldsymbol{\xi}'$, is then coupled to an ODE solver so that the evolution of the quadrature points may be solved over time. In the following results, the ODE solver used is based on a Rosenbrock formula of order two (Shampine and Reichelt, 1997).

For all cases, the initial number density function is assumed to be exponential

$$f_0(x) = C \exp(-\lambda x). \tag{4.37}$$

For most cases, the simple form with $C = \lambda = 1$ will be used. This case corresponds to a distribution normalized by the total number of particles, and the initial number average size is one. The method is sufficiently general to handle any piecewise integrable initial distribution, but the exponential distribution was chosen because of the availability of exact solutions.

Comparisons between exact and numerical solutions will be made in terms of the number density function, $f(x,t)$, and the mass density function, $xf(x,t)$, at several points. These quantities were approximated from the numerical solution by

$$f(\bar{x}_i, t) \approx \frac{1}{\Delta_i} \sum_{p:x_p \in I_i} w_p, \tag{4.38a}$$

$$\bar{x}_i f(\bar{x}_i, t) \approx \frac{1}{\Delta_i} \sum_{p:x_p \in I_i} \xi_p, \tag{4.38b}$$

where

$$\bar{x}_i \equiv \frac{\sum_{p:x_p \in I_i} \xi_p}{\sum_{p:x_p \in I_i} w_p}, \tag{4.39}$$

is the number average size in section i. Equations (4.38) are approximations and therefore introduce additional uncertainties into the analysis, but they are also a convenient way to compare solutions across various grids and quadrature orders.

4.3.1 Pure Random Breakage

In systems with negligible aggregation, the only process affecting the population is breakage. Over time, the number density function will shift to smaller sizes. It is

therefore important to have a sufficiently fine grid to distinguish the smaller particles that are produced in time.

For particles that break at a rate directly proportional to their size and whose products are uniformly distributed, the breakage rate and probability are given by $b(x) = b_0 x$ and $P(x|x') = 1/x'$. For the initial condition of Equation (4.37) with $C = \lambda = 1$, Ziff and McGrady (1985) found the exact solution to be

$$f(x,\tau) = (\tau^2 + 2\tau + 1)\exp[-(\tau + 1)x], \tag{4.40}$$

where $\tau \equiv b_0 t$.

The evolution of the quadrature points and weights is demonstrated in Figure 4.3 for the case of a uniform grid with one and two point quadratures. These results were obtained with 100 sections between $x = 0$ and $x = 20$. The dashed vertical lines represent section boundaries. For the one point quadrature Figure 4.3(a), there is a slight migration of the quadrature points towards the lower bound of their section as time evolves. This movement reflects the change in shape of the distribution to be more heavily weighted towards the smaller particles within each section. With two quadrature points, it is observed that there is very little movement of the quadrature points due to the fact that the distribution within each section is sufficiently smooth to be approximated by two delta functions.

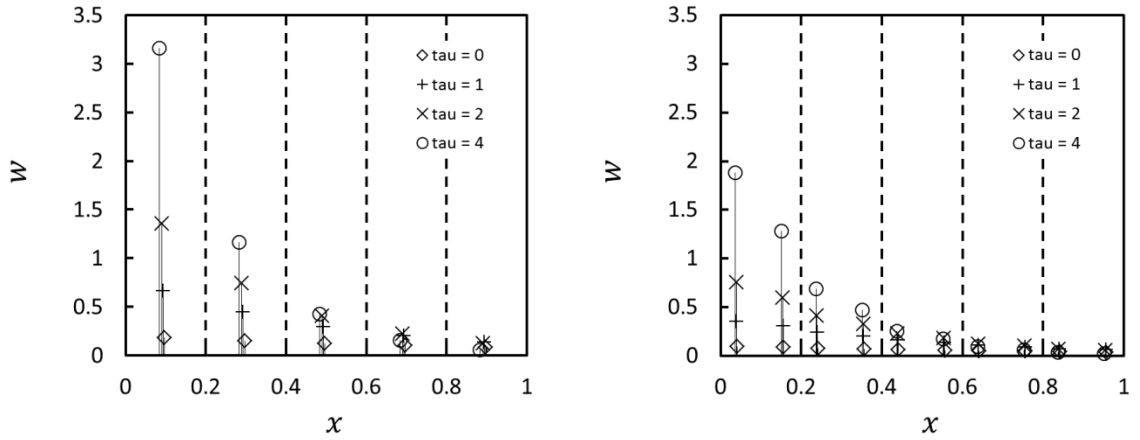

Figure 4.3: Quadrature weights and nodes for pure random breakage: (a) one-point quadrature, (b) two-point quadrature.

Another way of looking at the results is to compare sectional moments. This was done for the one point quadrature HySMOM, and the results are plotted in Figure 4.4. Since one point Gaussian quadrature preserves the first two moments, it is expected and observed that the method accurately predicts the analytical solution for sectional numbers and mass. The results are plotted on both linear (left column) and semi-logarithmic (right column) axes. The semi-log plots demonstrate that the numerical results are accurate over approximately seven decades of the numbers and masses.

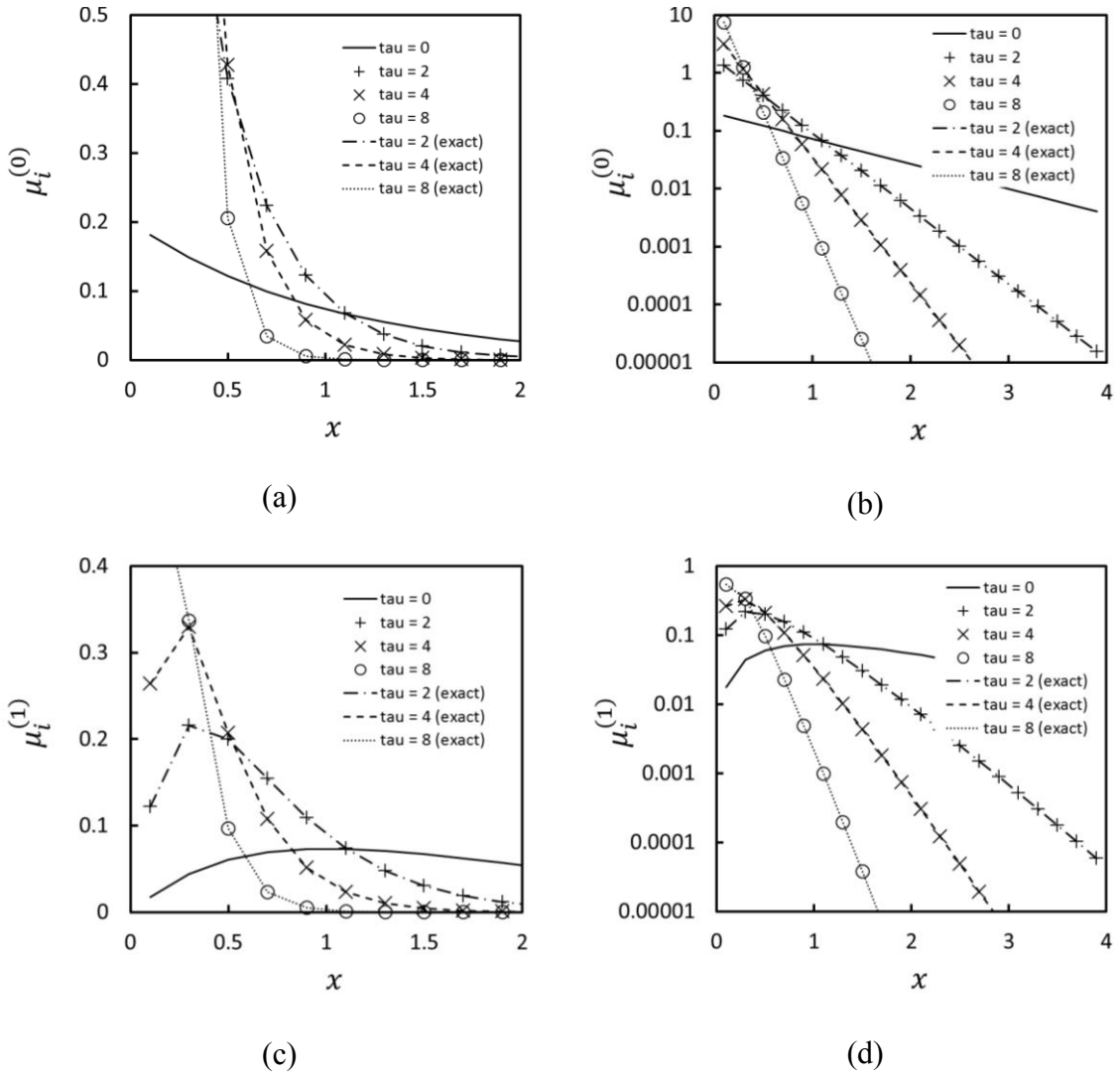

Figure 4.4: First two sectional moments from HySMOM with $M = 1$ compared to exact solutions on linear (left column) and semi-logarithmic (right column) scales.

Using a two point per section quadrature ($M = 2$) should result in accurate predictions of the first four moments. To demonstrate this, the global second and third moments are plotted versus time in Figure 4.5 on logarithmic axes. Results are given for several uniform grids, and it is seen that even very coarse grids ($N = 8$) result in accurate

predictions of these global moments at least up to $\tau = 100$ or an average of 101 breaks per particle.

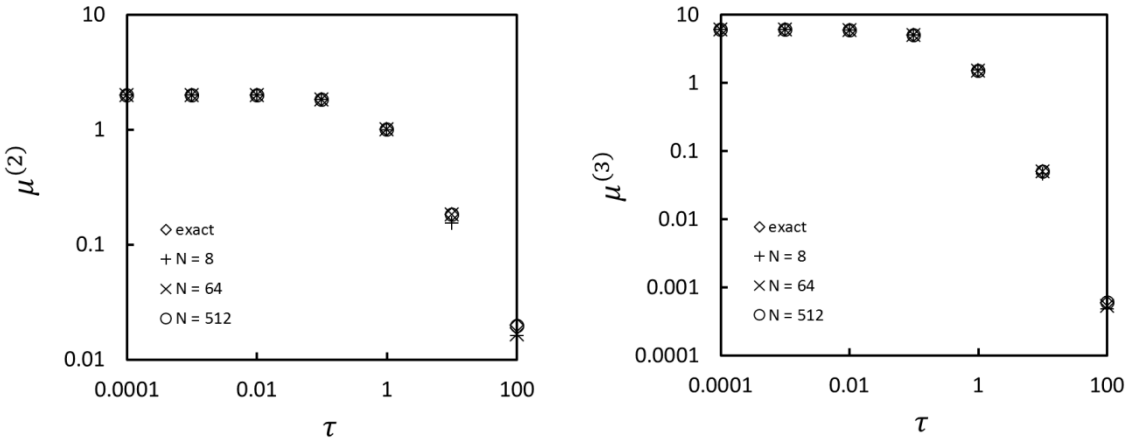

(a) (b)

Figure 4.5: Second and third global moments for pure random breakage with a two-point quadrature and a uniform grid.

Finally, the number and mass densities for $M = 1$ and $M = 2$ were compared for pure random breakage using a geometric grid. The results are plotted in Figure 4.6 on semi-logarithmic axes. When choosing a geometric grid, an important decision is the width of the first section. The first section must be small enough so that major features of the distribution are resolved at all times of interest. For the case of pure breakage with an initial exponential distribution, it is necessary that the first section be small enough that the distribution peak is still outside of it at the largest time of interest. It was found that choosing $\Delta_1 = 1e - 5$ was sufficient for the final simulation time of $\tau = 100$. It was observed that nearly identical results were obtained for both one and two point quadratures. In fact the differences are not observable in Figure 4.6 as the data points

overlap. The finer grid, $g = 2$, gives accurate predictions for both the number and mass densities. The coarser grid, $g = 4$, does fairly well except for several points on the right side of the peak. With $g = 4$, the grid is very coarse as compared to the grids used in much of the discretized PBE literature (compare to Hounslow et al., 1988; Hill and Ng, 1995; Kumar and Ramkrishna, 1996a;1996b).

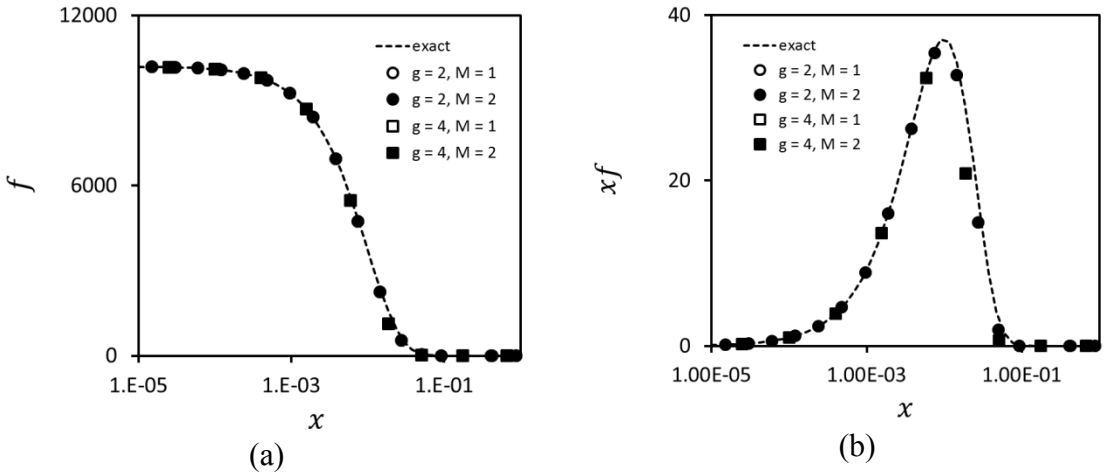

Figure 4.6: Number (a) and size (b) distributions for constant rate breakage on geometric grids at $\tau = 100$ and $\mu^{(0)}/\mu^{(0)}(\tau = 0) = 101$.

Since the one point quadrature performed very well for all grids, no other pure breakage problems were considered. In order to see significant differences between the one and two point quadratures, it was necessary to simulate aggregation.

4.3.2 Pure Aggregation

Many systems are dominated by aggregation or coagulation processes. Two special cases are considered in the following: (1) constant kernel aggregation, $a(x, x') =$

a_0, and (2) additive kernel aggregation, $a(x, x') = a_0(x + x')$. In both cases, the multiplicative constant will be absorbed into the time constant so that $\tau \equiv a_0 t$.

It has long been observed that uniform grids perform poorly for aggregation problems, and so only geometric grids will be used in the following. For both the constant and additive kernels, the smallest section was chosen to be $\Delta_1 = 0.001$. The total number of sections was varied so that the distribution was fully captured at the final simulation time.

4.3.2.1 Constant Kernel

Smoluchowski (1917) observed that Brownian motion aggregation is well approximated by constant kernel aggregation over much of the particle size range, and so constant kernel aggregation is widely used in processes such as crystallization. The analytical solution for the exponential initial distribution with $C = \lambda = 1$ was derived by Scott (1968):

$$f(x, \tau) = \frac{4}{(\tau + 2)^2} \exp\left[-\frac{2x}{(\tau + 2)}\right]. \tag{4.41}$$

Results for the number and mass density functions are plotted in Figure 4.7 on semi-logarithmic axes. These results correspond to time $\tau = 500$ when the number of particles is 0.004 times the original number. There is a consistent under prediction of the number density for the smaller particles, but this is most noticeable for the coarse grid ($g = 4$) with a one point quadrature. Even the coarse two point quadrature ($g = 4, M =$

2) does better than the fine grid with one point quadrature ($g = 2, M = 1$) in this region. These differences are less noticeable in the mass density plot (Figure 4.7(b)), but the results for constant kernel aggregation indicate that a two point quadrature allows for accurate predictions with a coarser grid.

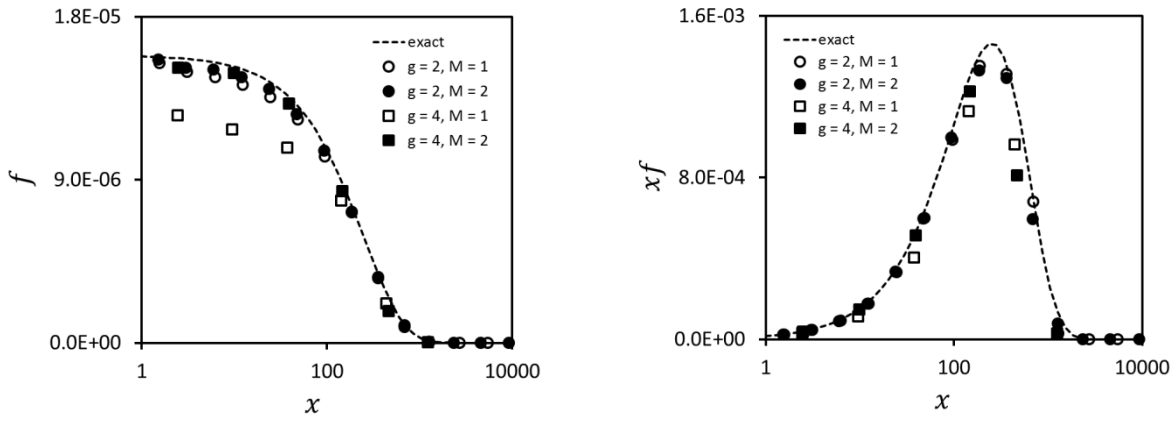

(a) (b)

Figure 4.7: Number (a) and size (b) distributions for constant kernel aggregation at $\tau = 500$ and $\mu^{(0)}/\mu^{(0)}(\tau = 0) = 0.004$.

4.3.2.2 Additive Kernel

Although differences are observed between one and two point quadratures for constant kernel aggregation, it is necessary to examine the differences in a more rapidly aggregating system. The sum kernel is sometimes used as an approximation to the kernel arising due to fluid stresses (the hydrodynamic kernel) (Vanni, 2000). The analytical solution for the exponential initial distribution is provided by Scott (1968):

$$f(x,\tau) = \exp(-\tau - (2 - e^{-\tau})x) \sum_{k=0}^{\infty} \frac{(1 - e^{-\tau})^k x^{2k}}{(k+1)!\,\Gamma(k+1)}. \tag{4.42}$$

Comparisons of the HySMOM results with this exact solution are plotted in Figure 4.8. The results correspond to a time of $\tau = 2$ when the number of particles is 0.1353 of the original number. The number density plot (Figure 4.8(a)) does not show significant differences between any of the solutions, but significant deviations are observed in the mass density plot (Figure 4.8(b)). It is observed that the one point quadrature on both grids significantly over predicts the mass density at larger sizes. This tendency towards over prediction was not observed for either of the two point quadrature results.

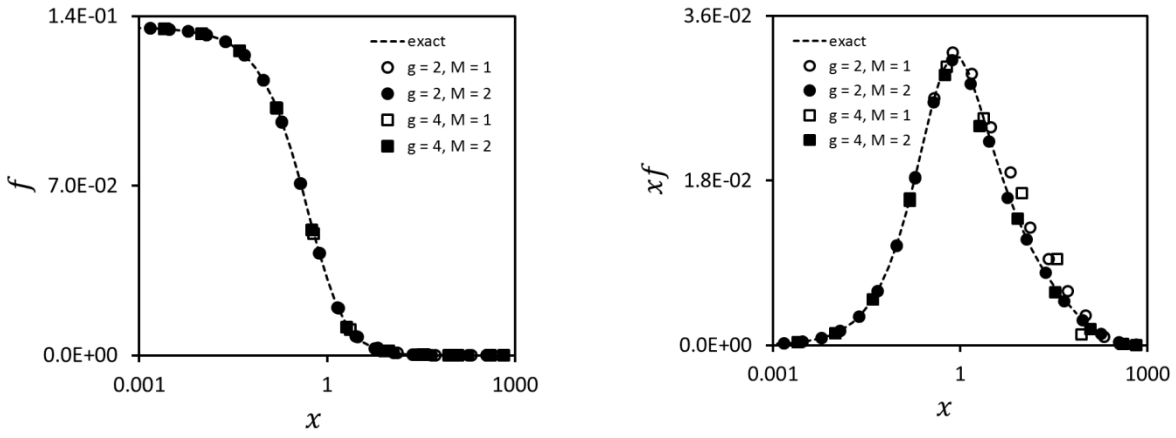

(a) (b)

Figure 4.8: Number (a) and size (b) distributions for additive kernel aggregation at $\tau = 2$ and $\mu^{(0)}/\mu^{(0)}(\tau = 0) = 0.1353$

Both sets of aggregation results indicate an advantage in using a two point quadrature, especially on coarser grids. In the next section, the robustness of the method is tested by a combined breakage and aggregation problem.

4.3.3 Combined Random Breakage and Constant Kernel Aggregation

Verification of the HySMOM method is limited by the number of available analytical solutions. Fortunately, there is an exact solution for at least one special case of combined breakage and aggregation. The case considered assumes random breakage and constant kernel aggregation where $b(x) = b_o x$, $P(x|x') = 1/x'$, and $a(x,x') = a_o$. The solution of this problem for an initially exponential number density function is provided by McCoy and Madras (2003):

$$f(x,\tau) = \frac{\mu^{(0)}(0)\phi^2(\tau)}{\bar{x}(0)} \exp\left(-\frac{\phi(\tau)}{\bar{x}(0)} x\right), \tag{4.43}$$

where $\tau \equiv a_o \mu^{(0)}(0) t$, $\bar{x} \equiv \mu^{(1)}/\mu^{(0)}$ is the number average size of the distribution, and

$$\phi(\tau) = \frac{\phi(\infty)\left[1 + \phi(\infty)\tanh\left(\frac{\phi(\infty)\tau}{2}\right)\right]}{\phi(\infty) + \tanh\left(\frac{\phi(\infty)\tau}{2}\right)}, \tag{4.44}$$

where $\phi(\infty) = \sqrt{2b_o/a_o}$ corresponds the relative number of particles in the steady-state distribution. For the special case where $\mu^{(0)}(0) = \mu^{(1)} = 1$, the solution is just

$$f(x,\tau) = \phi^2(\tau)e^{-\phi(\tau)x}. \tag{4.45}$$

Numerical results were obtained for the case of $a_o = 10b_o = 1$ or $\phi(\infty) = 0.4472$. A case dominated by aggregation was chosen since this seems to be the more difficult problem numerically. The progress of an aggregation dominated problem can be tracked by the quantity

$$\zeta_a \equiv \frac{1-\mu^{(0)}(\tau)}{1-\mu^{(0)}(\tau\to\infty)}. \tag{4.46}$$

The results are plotted in Figure 4.9 for $\tau = 3$ corresponding to a progress fraction of $\zeta_a = 0.82$. The number density plot shows little difference between the various numerical solutions. The mass density plot shows that both solutions at the coarser grid under predict the exact solution at larger sizes. However, it appears that again the two point quadrature performs better, if only slightly so, in this case.

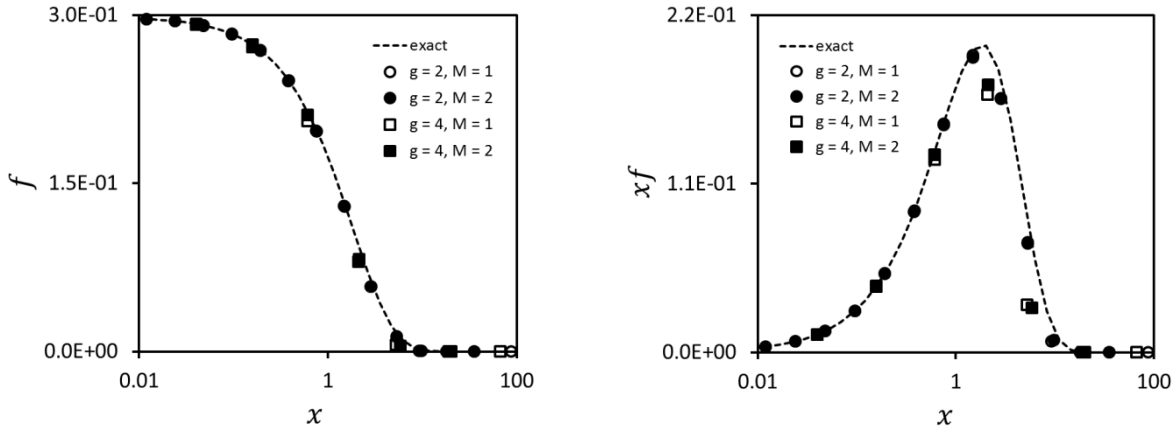

(a) (b)

Figure 4.9: Number (a) and size (b) distributions for combined random breakage and constant kernel aggregation at $\tau = 3$ and $\zeta_a = 0.8205$.

4.3.4 HySMOM Compared to Global DQMOM

As mentioned previously, the HySMOM can be thought of as either a generalization of the moving pivot technique for solving discretized PBEs or as a generalization of the global DQMOM. A comparison between sectional and global DQMOMs was made for the case of combined random breakage and constant kernel aggregation. The coefficients were chosen so that the system would be dominated by breakage: $a_o = 0.5b_o = 1$. The steady state number of particles is thus $\mu^{(0)}(\tau \to \infty) = \phi(\infty) = 2$. The progress of an aggregation dominated problem can be tracked by the variable

$$\zeta_b \equiv \frac{\mu^{(0)}(\tau) - \mu^{(0)}(\tau = 0)}{\mu^{(0)}(\tau \to \infty) - \mu^{(0)}(\tau = 0)}. \tag{4.47}$$

Results correspond to the distribution at time $\tau = 0.8$ for which $\zeta_b = 0.75$. Furthermore, it was found that a smallest section width of $\Delta_1 = 0.001$ was sufficient to fully resolve the distribution at all times.

The numerical solutions are compared in terms of the cumulative number density function defined by

$$F(x,t) \equiv \int_0^x f(x,t)dx. \tag{4.48}$$

Two quadrature points were used for the global DQMOM solution. For the HySMOM, a coarse geometric grid was used with $g = 6$ and $M = 2$. The results of this comparison are plotted in Figure 4.10. The advantage of the sectional approach is demonstrated by the resolution attained for smaller particles. The two-point DQMOM gives good global information but fails to describe the lower tail in any detail. Of course a two-point DQMOM is extremely coarse, and more points should be used. However, the problem remains that the global DQMOM will never resolve the tails of the distribution as well as the HySMOM solution on an appropriately chosen grid with a comparable number of total quadrature points.

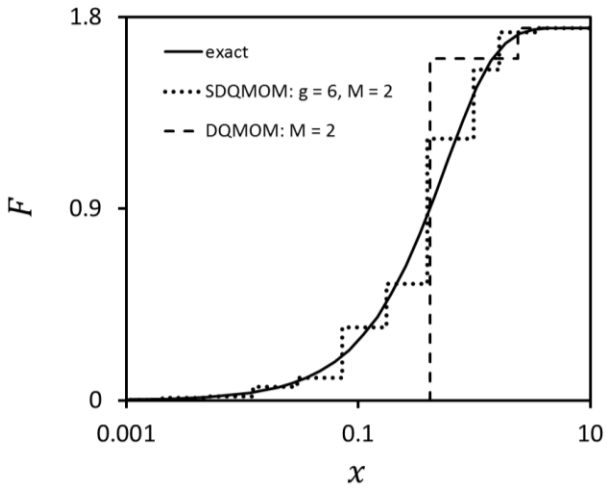

Figure 4.10: Cumulative number density functions for the exact, HySMOM, and global DQMOM solutions for combined random breakage and constant kernel aggregation at $\zeta_b = 0.75$.

4.4 SUMMARY AND CONCLUSIONS

A new approach for the solution of discretized population balance equations (PBEs) has been presented. The method is a generalization of the moving pivot technique of Kumar and Ramkrishna (1996b). Alternatively, the method is an extension of the direct quadrature of moments (DQMOM) (Fox, 2003) to a discretized domain. The approximate equations for this sectional version of the DQMOM were developed for the case of combined breakage and aggregation, but similar equations exist for including more general physics such as growth and nucleation. The primary advantage of the proposed method is that it allows the user greater control over the deployment of computational resources to the domains of primary importance.

Several verification cases were examined. The results indicate that the use of higher order methods give greater accuracy on coarser grids. The implication of this observation is that the number of quadrature points used within a section should increase as the section width increases.

Future work is needed to improve the utility of the HySMOM. Higher order quadratures ($M > 2$) should be investigated. Although moving from a one point to a two point quadrature showed significant improvements in accuracy for the cases examined, there will presumably be a point of diminishing returns with respect to the number of quadrature points used per section. The tradeoffs between grid resolution and the number of quadrature points per section should be studied more systematically. It remains to be seen how effective the HySMOM is for more complicated PBEs that include such physics as growth and nucleation combined with breakage and aggregation. A more general algorithm should include the ability to vary the number of quadrature points from section to section. This would seem to be useful in light of the observation of the potential accuracy gains associated with increasing the number of quadrature points on the coarse grids. Finally, the method presented here needs to be subjected to an error analysis in order to quantify its convergence properties with respect to both the grid and the number of quadrature points.

This chapter has dealt primarily with the numerical aspects of solving the PBEs that can be used to model pyrolysis chemistry at the mesoscale. At the continuum scale,

the loss of volatile molecules from the condensed phase is important for modeling thermal degradation physics. This is the topic of the next chapter.

5: Modeling Mass Loss

Thermal degradation can be considered as two coupled steps: (1) pyrolysis—the chemical conversion of polymer chains to successively smaller molecules and (2) devolatilization—the mass transport of sufficiently small molecules (volatiles) across the surface of the condensed phase. Pyrolysis has been considered in the previous chapters without detailed modeling of the mass loss. This is the approach typically taken in much of the thermal degradation literature. In this chapter, a step is taken towards coupling detailed mass loss and pyrolysis models.

5.1 Combined Pyrolysis and Loss

In previous chapters, the mesoscale population has been described in terms of a continuous number density function, $f(x,t)$. A continuous representation is helpful from a mathematical point of view, but it is only an approximation. Since a polymer chain is composed of a finite number of monomer units, the exact representation is discrete. The discretely distributed population can be described in terms of mass or molar density functions. Alternatively, a system of polymer chains may be described by the total number of moles or the total mass of all molecules over the range of chain lengths. In the following discussion, it is convenient to use the molar distribution function, n_i, defined as the total number of moles of chains with carbon number i. This distribution will be defined over the domain $1 \leq i \leq N$.

The dynamics of the population are exactly described by the discrete PBE

$$\frac{dn_i}{dt} = K_i - L_i, \qquad i = 1, \ldots, N, \tag{5.1}$$

where K_i accounts for changes due to pyrolysis and L_i accounts for changes due to devolatilization (or loss). The form of K_i depends upon the assumed pyrolysis mechanism. The first order loss mechanism is to assume that all of the volatile species are immediately transferred to the gas phase. This approach was used in Chapter 3 for calibrating model parameters with TGA data, and it can be expressed mathematically as $L_i = K_i$ for all i less than the critical value. In words, volatiles are immediately lost from the melt phase as soon as they are created. Under this model the number of melt phase volatiles is always zero, $n_i = 0$ for $i < l$.

Such a simple model of the loss rates, L_i, has two obvious deficiencies. First, it neglects the finite time that volatiles remain in the sample. Second, it treats all volatiles the same. In the next section, a bubbling model is introduced to take into account the transport time required for a notional volatile molecule to leave the condensed phase. In the section after the next, this model is expanded to take into account the different rates at which small molecules of different sizes devolatilize.

5.2 SINGLE COMPONENT BUBBLING MASS LOSS

A simple model of TGA is introduced that couples random scission pyrolysis and devolatilization physics. The parameters of this model are determined from literature data. Finally, the model is compared to isothermal TGA data for HDPE. The work in this section is also found in Bruns and Ezekoye (2011).

The models will be developed in the context of an isothermal polymer melt contained within a TGA sample pan as shown in Figure 5.1. The melt is discretized into two pseudo-species: volatile "1" and polymer "2". The two species have time-varying masses of $m_1(t)$ and $m_2(t)$. The initial melt is composed entirely of polymer. It is assumed that the polymer pyrolyzes due to random scission to generate volatiles. Volatiles devolatilize through the top surface of the sample. The top surface is the only surface through which mass can leave the system.

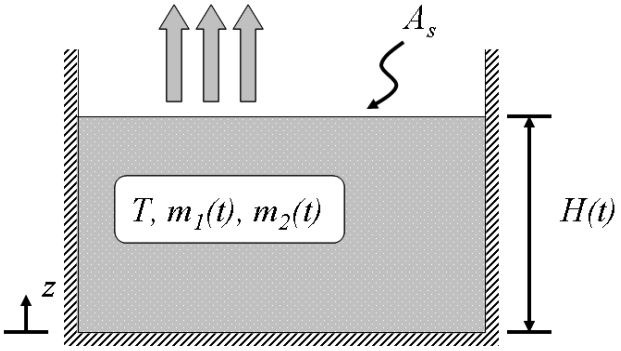

Figure 5.1: Diagram of a thermally degrading polymer melt.

The pyrolysis reactions will be modeled as random scission (Equation (3.2)). The dynamics of the polymer number distribution is governed by the discrete form of Equation (3.5) which can be written as

$$\widetilde{K}_i \equiv \frac{dn_i}{d\tau} = -(i-1)n_i + 2\sum_{j=i+1}^{N} n_j\,, \qquad i = l, \ldots, N, \tag{5.2}$$

where $\tau \equiv kt$, l is the critical carbon number dividing the notional volatile species from the polymer, and N is the largest polymer in the system. The mass of the notional polymer is proportional to the first moment of n_i over the domain from l to N. It can be shown that the notional polymer mass and number average MW, M_2, evolve according to

$$m_2(\tau) = m_0[1 + l(1 - e^{-\tau})]e^{-l\tau}, \tag{5.3a}$$

$$M_2(\tau) = M\frac{i_0 + l(i_0 - l - 1)(1 - e^{-\tau})}{i_0 - l - (i_0 - l - 1)e^{-\tau}} \tag{5.3b}$$

where m_0 is the initial mass of the sample, $M = 14\ \mathrm{g/mol}$ is the MW of a single unit of HDPE, and i_0 is the initial number average carbon number of the melt.

Equations (5.3) represent a model of isothermal pyrolysis in which the molecules immediately loose membership in the polymer population if they are smaller than the critical carbon number l. The newly generated volatile molecules (species 1) are still present in the sample, and it takes time for them to exit the sample surface.

A loss model is needed to account for the finite rate of devolatilization. The species in a polymer melt devolatilize at decreasingly slower rates with increasing carbon number. As time proceeds, pyrolysis increases the amount of volatiles in the melt. Because the sample temperature is assumed to be spatially uniform, the volatile generation will also be spatially uniform. Volatiles at the surface of the sample will devolatilize inducing a concentration gradient in the melt. Diffusion of volatiles to the surface is one possible mechanism for mass loss. However, it is known from observation that bubbling is vigorous at pyrolysis temperatures in HDPE. Bubbling reduces the

volatile concentration gradient, and introduces another, presumably dominant, loss mechanism referred to here as bubbling mass loss.

Several authors have considered bubbling mass loss. Wichman (1986) used a bubble number conservation equation to study degradation due to an imposed surface heat flux. For the purposes of comparing their kinetic pyrolysis models to experimental GC-MS data, Faravelli et al. (1999) developed a simple bubbling loss model. Butler (2002) also developed models for bubbling in combusting thermoplastic materials and incorporated these models into numerical simulations.

Consider a single bubble which nucleates, migrates, grows, and eventually crosses the sample surface. A bubble crossing the surface results in a total mass loss equal to the mass of the gas inside the bubble. In order to determine the mass loss rate for a system with many bubbles, it is necessary to model the mass and number of bubbles crossing the surface per unit of time. Depending on the location of their nucleation, bubbles crossing the surface will have different masses. The total mass loss rate is found by integration over the sample height

$$\frac{dm}{dt} = -A_s \int_0^H m_e(z_n)\, J\big(t - \tau_b(z_n)\big) dz_n \tag{5.4}$$

where $m_e(z_n)$ and $\tau_b(z_n)$ are the mass and lifespan of a bubble exiting the surface at time t and which were nucleated at position z_n. The model presented in Equation (5.4) neglects the different loss rates of different volatiles. The relationship to the detailed formulation of Equation (5.1) may be expressed as $dm/dt = -\sum_i M_i L_i$. The nucleation

rate, denoted J, is the number of bubbles produced per unit volume per unit second. Models for these three parameters are presented in the following sections.

All material properties are ultimately dependent on the thermodynamic state in the melt. The thermodynamic state is defined by the pressure and temperature, which are constant, and the chemical composition. It is assumed that the chemical composition may be approximately described by three quantities: the notional volatile MW, M_1, the notional polymer MW, M_2, and the volatile volume fraction, ϕ_1. It will be assumed that M_1 is a constant and is characteristic of the species that are volatile at the scenario temperature. The molecular weight of the polymer is determined from Equation (5.3b). Finally, a model is needed for the time evolution of the volatile volume fraction. Neglecting the mass of volatiles stored in bubbles, the volume fraction of the volatile species can be computed by

$$\phi_1 = \frac{\rho \bar{v}_1}{M_1} \frac{m - m_2}{m}, \tag{5.5}$$

where ρ is the total mixture density, $\bar{v}_1$ is the molar specific volume of the volatile, and $m = m_1 + m_2$ is the total sample mass.

5.2.1 Bubble Dynamics

The smaller molecules generated by pyrolysis are free to diffuse through the polymer melt. When enough volatile molecules diffuse in to a small region a bubble is nucleated at a height of z_n from the bottom of the sample. The bubble will rise due to its buoyancy and grow due to diffusion of volatile molecules to its surface. A diagram of this

process is sketched in Figure 5.2. Models are needed for the nucleation rate, J, the bubble growth rate, $\dot{m}_b$, and the bubble migration velocity, $\dot{z}$. In this section, models of these three processes are derived. The models are taken from the literature. For the purpose of this chapter, the simplest, reasonable model for each process was chosen.

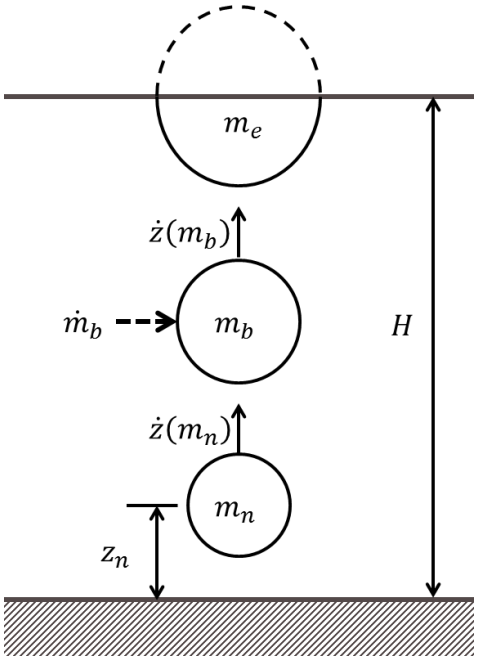

Figure 5.2: Diagram showing the three steps of bubbling mass loss: nucleation, growth, and migration.

5.2.1.1 Nucleation

For simplicity, it will be assumed that the nucleation is homogeneous. Both homogeneous and heterogeneous nucleation can be modeled as Arrhenius processes where the activation energy is equated to the work required to form a stable bubble. This work is dependent on both the surface tension and the change in pressure in the transition

from a liquid to a gas. A general model form from classical bubble nucleation theory (Blander and Katz, 1975) is

$$J = A\sigma^{1/2} \exp\left[-\frac{B\sigma^3}{T(P_1 - P)^2}\right], \qquad P_1 > P, \tag{5.6}$$

where σ is the bubble surface tension and P_1 is the vapor pressure of the volatile embedded in the polymer matrix. There is a significant literature on determining the values of A and B from more fundamental quantities, but as of yet it does not appear that any one theory is fully adequate.

For supercritical species at low concentrations, Henry's law is a valid model for the volatile vapor pressure. In terms of volume fraction,

$$P_1 = H_\phi \phi_1, \tag{5.7}$$

where H_ϕ is the volume fraction Henry coefficient.

5.2.1.2 Growth

Bubbles grow by diffusion of volatile molecules from the melt to the bubble surface. Favelukis and Albalak (1996) provide a survey of bubble growth models. A simple model for bubble growth is due to Epstein and Plesset (1950). This model assumes that (i) the diffusion is steady state, (ii) the bubble is stationary, (iii) the bubble gas is ideal, (iv) the bubble pressure is constant, (v) the process is isothermal, (vi) the pressure inside the bubble is equal to the pressure inside the liquid, and (vii) viscous normal stresses are negligible. As a consequence of assumption (ii), the predicted growth

rate is expected to be slower than the actual growth rate. A diagram of diffusionally driven bubble growth is provided in Figure 5.3.

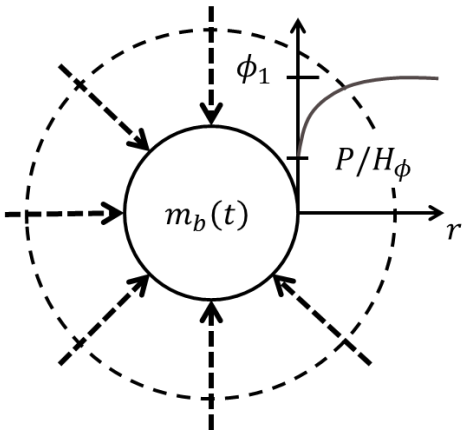

Figure 5.3: Diagram of the diffusionally driven bubble growth model used in this chapter.

Under these assumptions, the bubble radius, r_b, growth at large times is governed by the differential equation

$$\frac{dr_b}{dt} = \frac{RTD_1(P_1 - P)}{P\bar{v}_1 H_\phi}\frac{1}{r_b}, \tag{5.8}$$

where R is the gas constant and D_1 is the diffusivity of the volatiles in the condensed phase. It is reasonable to assume that the material properties in Equation (5.8) are approximately constant over the lifespan of a bubble. Integrating, and using the fact that the mass inside the bubble is $m_b = 4/3\pi r_b^3 \rho_b$, the bubble mass as a function of time is found to be

$$m_b^{2/3}(t) = m_n^{2/3} + C_1 t, \tag{5.9}$$

where

$$C_1 \equiv 2\left(\frac{4\pi}{3}\right)^{2/3} \frac{M_1 D_1 (P_1 - P)}{H_\phi \bar{v}_1 \rho_b^{1/3}}, \tag{5.10}$$

m_n is the mass of a nucleated bubble and ρ_b is the density of the volatile gas inside the bubble. The fact that the pressure inside the bubble equals the pressure in the melt implies that the volume fraction of volatile at the surface of the bubble is P/H_ϕ. The parameter C_1 is a constant over the lifespan of a bubble but will vary over the course of a TGA simulation.

5.2.1.3 Migration

A bubble velocity model is necessary so that the lifespan of the bubble can be computed as a function of its nucleation coordinate. The bubbles are assumed to rise due to buoyancy forces. Wichman (1986) modeled bubble migration in thermoplastics as being driven by a gradient in surface tension. In small samples, there is no significant gradient in temperature and thus no significant gradient in surface tension. Therefore, bubble migration is due solely to buoyancy. It is assumed that the bubble reaches its equilibrium velocity quickly relative to its growth. If the Reynold's number is small, and the fluid is Newtonian, then the bubble velocity is governed by Stokes' Law:

$$\frac{dz_b}{dt} = \frac{2}{9}\frac{\rho - \rho_b}{\mu} g r_b^2, \tag{5.11}$$

where z_b is the height of the bubble, ρ is the melt density, μ is the melt viscosity, and g is the gravitational constant. In terms of mass, Equation (5.11) is

$$\frac{dz_b}{dt} = C_2 m_b^{2/3}, \tag{5.12}$$

where

$$C_2 \equiv \frac{2}{9}\left(\frac{3}{4\pi}\right)^{2/3} \frac{g(\rho - \rho_b)}{\rho_b^{2/3}\mu} m_b^{2/3}. \tag{5.13}$$

The solution of this equation provides the lifespan of a single bubble as a function of its nucleation height. Substituting Equation (5.9) into Equation (5.12) and integrating from z_n to H while assuming constant properties gives a quadratic equation in terms of the bubble lifespan, τ_b. The only positive solution is

$$\tau_b(z_n) = \frac{1}{C_1}\left[-m_n^{2/3} + \sqrt{m_n^{4/3} + \frac{2C_1(H - z_n)}{C_2}}\right]. \tag{5.14}$$

5.2.1.4 Mass Loss Rate

The mass of a bubble exiting the surface depends upon its nucleation location. This relationship is provided by substitution Equation (5.14) into Equation (5.9) to get

$$m_e(z_n) = m_b[\tau_b(z_n)] = \left[m_n^{4/3} + \frac{2C_1(H - z_n)}{C_2}\right]^{3/4}. \tag{5.15}$$

Since the material properties are constant over a bubble's lifespan, the nucleation rate at the time of a bubble's exit from the sample is approximately the same as the rate at that bubble's nucleation. Mathematically, the approximation $J\big(t - \tau_b(z_n)\big) \approx J(t)$ is valid. Equation (5.15) may be substituted into Equation (5.4) to get

$$\frac{dm}{dt} = -JA_s \int_0^H \left[m_n^{4/3} + \frac{2C_1(H - z_n)}{C_2} \right]^{3/4} dz_n. \tag{5.16}$$

The integral may be evaluated by a simple change of variables leading to the convenient form for mass loss rate

$$\frac{dm}{dt} = -JV\bar{m}_e, \tag{5.17}$$

where

$$\bar{m}_e = \frac{2C_2}{7C_1H} \left[\left(m_n^{7/3} + \frac{2C_1H}{C_2} \right)^{7/4} - m_n^{7/3} \right]. \tag{5.18}$$

is the average mass in an exiting bubble.

5.2.2 Material Property Data

The parameters in the loss model are difficult to characterize for polymeric materials—even structurally simple thermoplastics such as HDPE. In this section, experimental data and property models for HDPE are surveyed.

5.2.2.1 Scission Rate

It is assumed that the random scission rate is equal to the chain initiation rate. The Arrhenius parameters for chain initiation are approximated by the RMD results of Chapter 3. For the largest molecule studied ($i = 200$), the activation energy and pre-exponential were found to be 251 kJ/mol and $10^{14.6}$ 1/s.

5.2.2.2 Densities

High-density polyethylene is, by definition, any polyethylene with a solid density of at least 9.41 g/cm^3. The density of polyethylene melts is around 20% less than this value. Bird et al. (1987) cite data that can be linearly fit by the correlation

$$\rho_2(T) = (1.158 + 8.09 \times 10^{-4}T)^{-1}\,\mathrm{g/cm^3}\,, 133°\mathrm{C} < T < 200°\mathrm{C}. \qquad (5.19)$$

The density of smaller *n*-alkanes depends strongly on both MW and temperature. For temperatures between 20–100ºC and carbon numbers between 3–46, von Meerwall et al. (1998) found that literature data from a variety of sources could be fit by

$$\rho_1(T, M_1) = 1/\rho(T, M_1 \to \infty) + 2V_e(T)/M_1 \qquad (5.20)$$

where V_e is the molar volume of the end-chain group. The authors provide correlations for the two parameters. Equation (5.20) can be used for computing the density of binary mixtures if M_1 is replaced by the volume average MW.

5.2.2.3 Notional Volatiles

The volatile pyrolysis products of HDPE are various alkanes and alkenes distributed over a range of carbon numbers. The products appear to be smaller than $l = 30$ for temperatures around 400ºC. Plots of the carbon number distribution at these temperatures (Figure 2.7) reveal that the average carbon number is around 12. Therefore, in the simulations of the next section, the carbon number of the notional volatile species will be taken to be one-third of the critical carbon number, or $i_1 = l/3$.

5.2.2.4 Critical Carbon Number

The carbon number dividing the notional volatiles and polymers will be chosen so that the boiling temperature of all species smaller than l is greater than the sample temperature. There are a number of correlations that relate the boiling temperature of *n*-alkanes to their carbon numbers. Inverting the correlation suggested by Egloff et al. (1940) yields

$$l(T) = 10^{\frac{T+416.31}{745.42}} - 4.4, \tag{5.21}$$

where T is in units kelvin. Within the range of carbon numbers 2 to 19, the model agrees with experimental data to within less than one percent.

5.2.2.5 Surface Tension

The nucleation rate depends strongly on the interfacial tension between the polymer melt and the bubble, σ. It is assumed that σ is approximately the surface tension of the polymer melt in air. Wu (1969) performed pendant drop experiments to measure the surface tension of HDPE at temperatures of 300–450 K. It was found that the temperature dependence is linear with

$$\sigma(T) = 0.0524 - (5.7 \times 10^{-5})T. \tag{5.22}$$

5.2.2.6 Henry Coefficient

Flory-Huggins theory provides an estimate of the Henry's law coefficient (Merrill, 1996). The fundamental quantity of this theory is the interaction parameter, χ, that measures the degree to which the volatile is compatible with the polymer. A large χ

indicates poor compatibility, and negative values correspond to good compatibility. The Henry coefficient in terms of the interaction parameter is

$$H_\phi = P_1^0 e^{1+\chi}, \tag{5.23}$$

where P_1^0 is the vapor pressure of the pure volatile substance. Schreiber et al. (1973) measured χ for various hydrocarbons in HDPE at 422 K. These experiments included results for *n*-alkanes with carbon numbers of n = 8, 9, 10, and 12. The dependence of the interaction parameter on chain length is approximately linear with $\chi = -0.02n + 0.52$.

Ruzicka and Majer (1994) surveyed the literature data for the vapor pressure of *n*-alkanes with carbon numbers from 5 to 20. The results of this survey are summarized in terms of the coefficients of the Cox equation

$$\ln \frac{P_i^0}{P^0} = \left(1 - \frac{T_{b,i}}{T}\right) \exp\left[A_{0,i} + A_{1,i}T + A_{2,i}T^2\right], \tag{5.24}$$

where P^0 is the reference pressure for the boiling temperature. Both temperatures are in units Kelvin. It was found that the coefficients $A_{0,i}$, $A_{1,i}$, and $A_{2,i}$ could be linearly fit to the carbon number:

$$A_{0,i} = 0.0367i + 2.60, \tag{5.25a}$$

$$A_{1,i} = -2.04 \times 10^{-3}, \tag{5.25b}$$

$$A_{2,i} = -(7.13 \times 10^{-8})i + 2.60 \times 10^{-6}. \tag{5.25c}$$

The boiling temperature may be computed from the correlation of Egloff et al. (1940)

$$T_{b,i} = 745.42 \log(i + 4.4) - 416.31. \tag{5.26}$$

5.2.2.7 Molar Volume of the Volatile Species

It is also necessary to specify the molar volume in order to compute Equation (5.10). The required molar volume is the space occupied by a mole of the volatile molecules in the condensed phase matrix. Molar volumes for various solvents are provided by Zielinski and Duda (1996) at 0 K. For the *n*-alkanes, the results are nearly exactly linear following

$$\bar{v}_i = 14.0i + 15.3. \tag{5.27}$$

5.2.2.8 Diffusivities

Equation (5.10) also depends upon the diffusivity of the notional volatile within the polymer matrix. As was argued in Chapter 2, the diffusivity may be approximated by the self-diffusion coefficient of the volatile in the melt. Diffusion in liquid *n*-alkanes and in *n*-alkane/polyethylene mixtures has been studied experimentally and theoretically by von Meerwall et al. (1998; 1999). It was found that the self-diffusion of *n*-alkanes in PE melts can be modeled by

$$D_1(T, M_1, M_2, \phi_1) = \frac{A}{M_1}\exp\left(-\frac{E_a}{RT} - \frac{1}{f}\right)\left\{1 + \frac{M_1}{r[1 + 15(M_e/M_1)^2]}\right\}^{-1}, \tag{5.28}$$

where f is the free-volume fraction, r is the ratio of reptation and Rouse diffusion coefficient constants, and M_e is the critical molecular weight for chain entanglements. The authors suggest using $r = 734/(1 - \phi_1)$. Also, $E_a = 0.81\,\text{kcal/mol}$ and $A = 0.306\,\text{cm}^2 \cdot \text{mol/g} \cdot \text{s}$. These constants were found from NMR experiments on *n*-alkanes. For binary mixtures,

$$f(T, M_1, M_2, \phi_1) = f_\infty(T) + 2V_e(T)\rho(T, M_v)/M_v, \tag{5.29}$$

where M_v is the volume average molecular weight and ρ is the mixture density. In addition, von Meerwall provides correlations for the fractional free-volume at infinite MW, f_∞, and the free volume of one mole of chain ends, V_E:

$$f_\infty(T) = 0.100 + 0.0007T, \tag{5.30a}$$

$$V_e(T) = 13.93 + 0.060T, \tag{5.30b}$$

where the units of temperature are in Celsius and the units of V_e are $\mathrm{cm}^3/\mathrm{mol}$.

5.2.2.9 Viscosity

The bubble velocity depends on the viscosity of the melt. Polymers are generally non-Newtonian showing a varying viscosity at high shear rates (Bird et al., 1987). At low bubble velocities, the stress tensor can be approximated by Newton's law of viscosity thus making it necessary to specify a Newtonian viscosity only. This viscosity is strongly dependent on the size distributions of the polymer chains. Berry and Fox (1968) studied the viscosity of many polymer melts and found that

$$\log \mu(M_w, T) = \begin{cases} \log \mu_e(T) + \log(M_w/M_e), & M_w < M_e \\ \log \mu_e(T) + 3.4 \log(M_w/M_e), & M_w > M_e \end{cases} \tag{5.31}$$

where M_w is the weight average molecular weight of the melt and μ_e is the entanglement viscosity. Van Krevelen and te Nijenhuis (2009) report values of $M_e = 3{,}500\ \mathrm{g/mol}$ and $\mu(M_w = 10^5, T = 190°\mathrm{C}) = 2 \times 10^4\ \mathrm{N \cdot s/m^2}$. These properties imply that the entanglement viscosity is $\mu_e = 0.224\ \mathrm{N \cdot s/m^2}$.

5.2.3 Results and Discussion

Simulations were performed by integrating Equation (5.16) using material properties based upon the data of the previous section. Three different temperatures were considered, and the results were compared to the isothermal TGA data of Conesa et al. (1996). The scenario parameters are listed in Table 5.1. These values were chosen to conform to typical isothermal TGA operating conditions.

T	400, 410, 420ºC
m_0	10 mg
i_0	990
A_s	8 mm^2

Table 5.1: Scenario parameters for simulations.

The results of the $T = 410°C$ simulation are plotted in Figure 5.4. Figure 5.4(a) shows normalized (by m_0) masses as a function of time. The volatile mass is represented by the dashed line, the polymer mass is represented by the dotted line, the total mass (sum of volatile and polymer) is represented by the solid line, and the experimental data are represented by the circles. The bubbling loss model introduces a lag into the mass loss rate due to the time needed to generate enough volatiles to so that $P_1 > P$ and nucleation is switched on according to Equation (5.6). For the system studied, the inclusion of this lag seems to improve the prediction. At around 150 min, the bubble loss model under predicts the mass loss rate indicating that the diffusion of volatiles to the surface is becoming significant. It is observed that the point of divergence between the experiment

and the model corresponds to the point at which the sample becomes mostly composed of volatiles—an unphysical state. Therefore, at large times, the bubble loss model needs to be supplemented by a surface evaporation loss model.

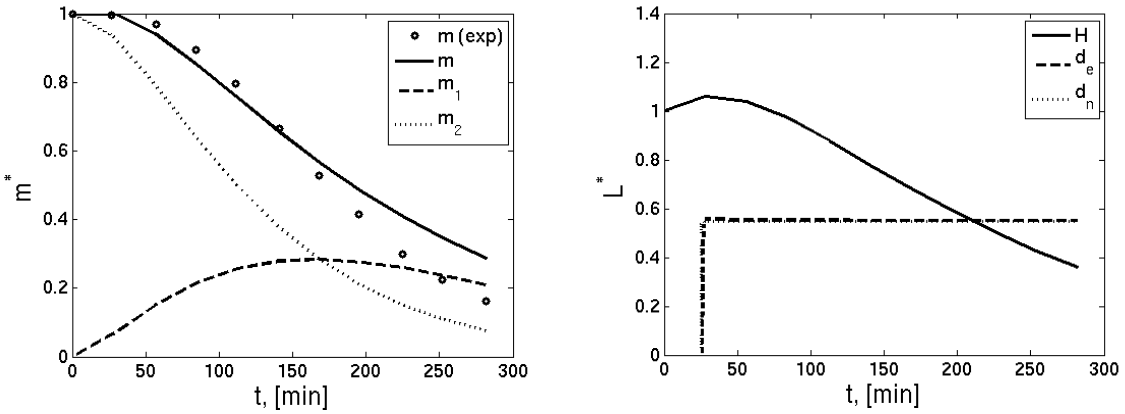

(a) (b)

Figure 5.4: TGA simulation of HDPE and experimental data (Conesa et al., 1996) at $T = 410^{\circ}$ C. Normalized masses (a) and lengths (b) as a function of time.

Figure 5.4(b) shows normalized (by H_0) lengths as a function of time. The sample initially swells as the polymer is converted to a lower MW liquid. This is due to the increasing free-volume associated with a higher number of chain end groups (see (5.20)). Bubble nucleation does not begin until approximately 30 min into the simulation. It is observed that the bubbles do not grow significantly as they migrate to the surface. At around 210 min the sample becomes thinner than a single bubble diameter, and the model is no longer valid.

Three experimental TGA traces are plotted in Figure 5.5 along with predictions based upon the bubbling loss model. At temperatures of 400°C and 410°C, the model

predicts the experimental data fairly well. The model begins to under predict the mass loss rate at 410°C for high conversions ($m^* < 0.4$). This trend becomes especially noticeable for the simulation at 420°C. This divergence between model and experiment is most likely due to changes in the material properties due to temperature that were not properly accounted for. Another possible explanation for the insufficiency of the model at higher temperatures is an increase in volatile diffusion directly to the sample surface. At high conversions and low sample heights it is likely that mass is lost in parallel between the bubbling loss mechanism and surface diffusion.

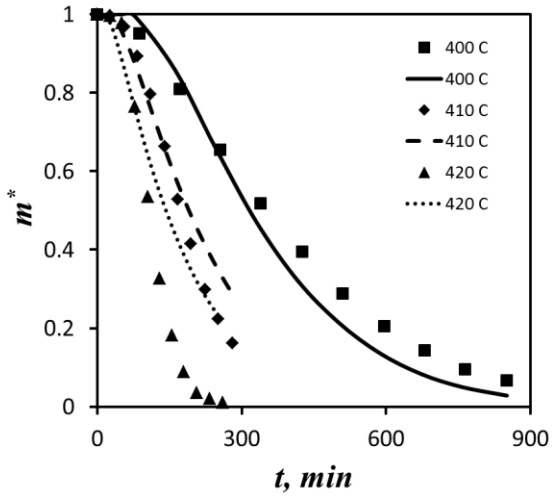

Figure 5.5: TGA simulations of HDPE at several temperatures (markers represent experimental data from Conesa et al., 1996).

5.3 MULTICOMPONENT BUBBLING MASS LOSS

In the previous section, the bubbles were treated as being composed of a single notional volatile species. The advantage of this approach is that it avoids the complexity of a multicomponent analysis. The disadvantage is that all knowledge about the

speciation of the small species is lost. That is, it is not possible to predict the composition of the pyrolysis gas. A compromise between a detailed multicomponent analysis and a single notional volatile model is to assume that the volatiles are lost by bubble growth in parallel. Under this model, there are several volatile species, but the loss of each species is independent of the loss rate of the other volatiles. A diagram of this model for three components is sketched in Figure 5.6.

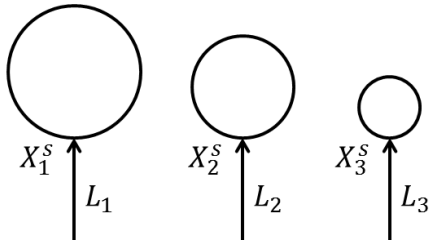

Figure 5.6: Schematic of three component parallel bubble mass loss.

For a single component bubble, nucleation will not occur unless the partial pressure of the volatile exceeds the ambient pressure, or $P_i^m > P$ where the superscript m indicates that the property is in the melt phase. For supercritical species at low concentrations, Henry's Law is valid so that

$$P_i^m = H_{X,i} X_i^m, \tag{5.32}$$

where $H_{X,i}$ is a temperature dependent constant and X_i^m is the mole fraction of species i in the melt phase. If the partial pressure exceeds the ambient pressure, then the bubble will grow through diffusion according to

$$\frac{dn_i^b}{dt} = f\left(n_i^b\right) D_i \left(X_i^m - X_i^s\left(n_i^b\right)\right), \qquad P_i^m > P, \tag{5.33}$$

where n_i^b is the number of moles inside the bubble and X_i^s is the mole fraction at the surface of the bubble on the melt side. Both f and X_i^s have a strong nonlinear dependence on the size of the bubble. These dependencies may be integrated out by assuming average values corresponding to an average molar flux over the life of the bubble. The total loss rate of a species is then the average value of Equation (5.33) multiplied by the total number of bubbles

$$L_i = \bar{f} N_b D_i (X_i^m - \bar{X}_i^s), \qquad P_i^m > P, \tag{5.34}$$

where the overline denotes an effective average value and N_b is the total number of bubbles.

Small linear alkanes diffuse at significantly faster rates as compared to larger ones. It is seen that for the diffusion of linear alkanes in polyethylene, the diffusivity of small species follows the Rouse model of diffusion such that the diffusivity is proportional to the inverse of the carbon number (von Meerwall et al., 1999), or $D_i = D_0(T) i^{-1}$. The Rouse model pertains for all chains shorter than the entanglement chain length which for polyethylene is around 3,500 g/mol corresponding to a carbon number of around 250 (van Krevelen and te Nijenhuis, 2009). Based on the results of evolved gas analysis, the volatile species are much smaller than the entanglement length. The number of bubbles will be proportional to the volume which is proportional to the mass so $N_b = a m^m$. A simplified loss model is obtained by introducing a mass loss parameter, $A_L \equiv \bar{f} a D_0$, to account for the unresolved physics of the bubbling mass loss. The mass loss parameter will be modeled as a constant to a first approximation. In reality, the

number of bubbles will depend on the nucleation rate which is temperature and partial pressure dependent. Also, the diffusivity coefficient, D_0, has a temperature dependence. Since pyrolysis takes place over a narrow temperature range it is plausible to neglect these temperature dependencies.

The average surface concentration is determined by Henry's law and the total pressure inside the bubble (since the total pressure is equal to the partial pressure of the gas in a single component mixture). The pressure inside the bubble varies significantly as the bubble grows, but it is assumed that the average bubble pressure is the limiting value of the ambient pressure. The loss mechanism can be written in its final form as

$$L_i = \begin{cases} 0, & X_i^m \leq P/H_{x,i} \\ A_L m^m i^{-1} \left(X_i^m - \dfrac{P}{H_{x,i}} \right), & X_i^m > P/H_{x,i} \end{cases}, \tag{5.35}$$

This model involves several simplifications, but it captures the details of the speciation associated with loss in a self-consistent manner.

The loss model of Equation (5.35) will be exercised in the following chapter for two applications of engineering interest. Computation of L_i requires an estimate of the Henry's constant, $H_{X,i}$. Maloney and Prausnitz (1976) developed a correlation for the weight fraction Henry's constant, $H_{W,i} = (M/M_i)H_{X,i}$, of small organic molecules in low-density polyethylene melts. The final form of the correlation is written as

$$H_{W,i} = \frac{T_{c,i}}{M_i} 10^{g_i^{(0)} + \omega_i g_i^{(1)}}, \tag{5.36}$$

where $T_{c,i}$ and ω_i are the critical temperature and accentric factor of species i. The two g functions in Equation (5.36) are

$$g_i^{(0)} = 2.401 - \frac{1.3833}{T/T_{c,i}} - \frac{0.4913}{\left(T/T_{c,i}\right)^2} + 2.006\exp\left(-0.0148T_{c,i}\right) + \frac{371.4}{T}, \quad (5.37a)$$

$$g_i^{(0)} = 0.690 + \frac{0.4813}{T/T_{c,i}} - \frac{1.1328}{\left(T/T_{c,i}\right)^2}, \quad (5.37b)$$

where all temperatures are in units Kelvin. The constants in the correlation were determined from gas-liquid chromatography data at melt temperatures of up to 300°C. The largest species used to obtain data was *n*-octane. Error in the correlation was reported to be 12% although most of the contribution to this average comes from the data for the polar species vinyl acetate. It was also found that the average molecular weight of the PE melt had no influence on the solubilities. Use of this correlation in a pyrolyzing system assumes that the extrapolation can reasonably be extended to larger molecules and higher temperatures.

The correlation of Equations (5.36) and (5.37) is parameterized in terms of solute molecular weight, critical temperature, and acentric factor. Fits of literature data were used in computing these terms. The critical temperatures were fit from data from Gallant and Yaws (1992) for alpha olefins up to 1-octadecene. It was found that a good fit in this range of carbon numbers is provided by

$$T_{c,i} = 213.3\ln i + 126.9, \qquad i = 2, \ldots, 18, \quad (5.38)$$

where the resultant temperature is in degrees Kelvin. Equation (5.38) is plotted along with the experimental data in Figure 5.7.

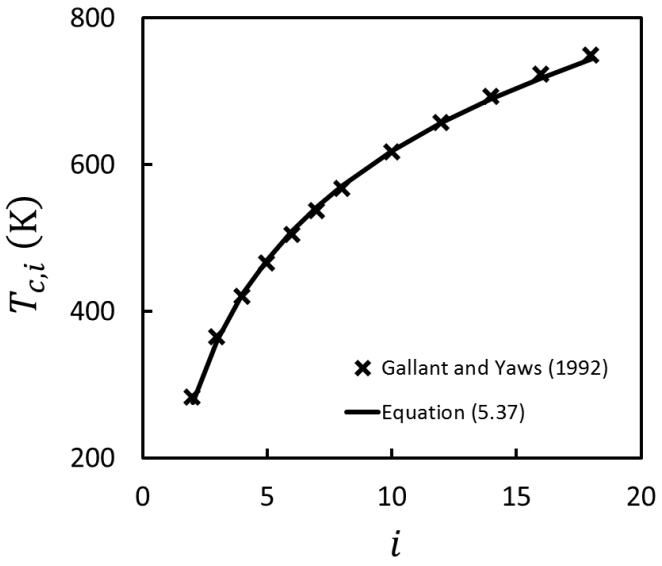

Figure 5.7: Experimental data for critical temperature versus carbon number for linear α-alkenes along with fit.

Data for acentric factors of linear alkanes up to *n*-isocane are available in Poling et al. (2001). Since the reported values are similar for linear alkanes and alkenes with identical carbon numbers, the same linear fit will be used for both types of molecules. A good fit is provided by

$$\omega_i = 0.0425i + 0.0442, \qquad i = 2, \ldots, 20. \tag{5.39}$$

The fit is compared to data in Figure 5.8.

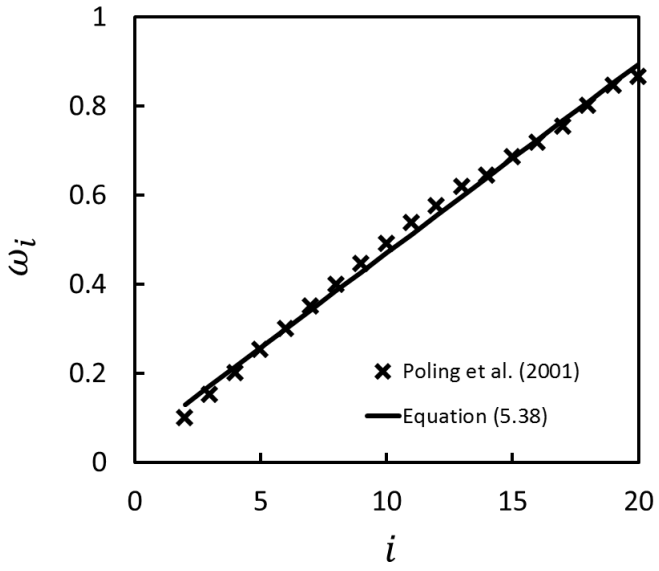

Figure 5.8: Experimental data for acentric factor versus carbon number for linear alkanes along with fit.

Both Equation (5.38) and Equation (5.39) are purely empirical. It is therefore unjustifiable to extrapolate beyond the bounds within which the data were obtained.

5.4 CONCLUSIONS

In this chapter, two models for mass loss for thermally degrading linear thermoplastics were developed. Both of these models were based on the observation that HDPE vigorously bubbles at the onset of pyrolysis. The first model predicts the total mass loss rate assuming a single volatile component. Devolatilization was modeled as bubble nucleation, growth, and migration across the sample surface. Making predictions based on this model required a literature review of HDPE material properties. There is a great deal of uncertainty in the material property estimates, and it would be helpful to

perform a sensitivity analysis to find which properties need to be more accurately modeled. The single component model was compared to experimental TGA data for HDPE. The bubble loss mechanism seems promising as a model for predicting TGA data for linear thermoplastics, but the model has a limited range of validity and needs to be supplemented by a diffusion and surface vaporization loss mechanism. It seems that the model can predict TGA traces fairly well at low temperatures. In order to extend the applicability of the model to higher temperatures, it will be necessary to improve the material property models.

Since many applications require detailed information about the pyrolysis gas composition, a multicomponent bubble loss model was also developed. This model assumes that individual bubbles are single component, but different bubbles are composed of different. In the next chapter, the multicomponent loss model is used in two applications.

6: Applications using Combined Pyrolysis and Loss Models

The modeling efforts of the previous chapters have been directed towards providing the simulation tools necessary for detailed modeling of thermal degradation in engineering applications. As was mentioned in Chapter 1, two engineering applications of particular importance are material flammability and industrial pyrolysis of plastic wastes. In this chapter, two specific problems are selected in order to demonstrate the practical use of the methods developed in this dissertation. In the first section, a combined pyrolysis/loss model is presented. The pyrolysis submodel is a chemically consistent version of the random scission model used in Chapter 3. For both applications, the multicomponent bubbling loss of Chapter 5 is used. The domain is discretized according to a discrete version of the approximate PBE solution method presented in Chapter 4.

The combined PBE model is then applied towards two problems of engineering relevance. The first problem is to predict the piloted ignition conditions of a slab of HDPE. The second problem is to predict DSC results.

6.1 Pyrolysis Model and Discretization

In this section, pyrolysis and devolatilization are modeled in detail using a discrete PBE. Condensed phase heat transfer will not be considered since it is assumed that the sample is isothermal. Similarly, it is assumed that the chemical composition is the

same everywhere. These assumptions are reasonable for thin samples of HDPE since significant bubbling will result in a well-mixed melt phase.

A modified random scission pyrolysis mechanism will be assumed for the development of the kinetic part of the governing PBE. Random scission has been widely used in the pyrolysis modeling literature and is a reasonable approximation to the actual mechanism of polyethylene pyrolysis. However, typical random scission models are chemically invalid. Specifically, care must be taken to ensure that the breakage reaction results in products in the same population as the reactants. This detail becomes necessary when detailed modeling of the energetics is required. A chemically valid version of random scission is described below.

All molecules are assumed to be linear alpha-olefins. Linear alpha-olefins have at least one unsaturated end-group. It is assumed that the molecules pyrolyze by a single, compound reaction that includes both an initiation reaction to form radicals and a disproportionation reaction to convert the radicals back to olefins. Neither type of end-group bond is allowed to break. This assumption is reasonable since these bonds are significantly stronger (see Chapter 3).

The assumed mechanism can be described by the chemical balance

$$\mathrm{O}_i \xrightarrow{k} \mathrm{O}_j + \mathrm{O}_{i-j}, \qquad i = 4, \ldots, N, \qquad j = 2, \ldots, i-2, \tag{6.1}$$

where O_i denotes an olefin polymer chain with i carbon atoms and N is the size of the largest molecule in the sample population. Random scission is just the assumption that

the rate constant is the same for all possible reactions in the template of Equation (6.1). The evolution of the species in the melt phase is then governed by the discrete PBE

$$\frac{dn_i^m}{dt} = K_i^m - L_i, \qquad i = 2, \ldots, N, \tag{6.2}$$

where

$$K_i^m \equiv \begin{cases} k^m \left[-(i-3)n_i^m + 2 \sum_{j=i+2}^{N} n_j^m \right], & i \geq 3 \\ 2k^m \sum_{j=4}^{N} n_j^m, & i = 2 \end{cases} \tag{6.3}$$

and n_i^m is the number of moles of olefins of carbon number i in the melt phase. The first term in Equation (5.1), K_i^m, represents the net gain of species i due to the pyrolysis reactions. The second term, L_i, accounts for mass loss out of the melt phase. In the remainder of this chapter, the multicomponent loss model from the previous chapter (Equation 5.34) will be assumed.

Since N is typically large ($\sim 10^4 - 10^6$), it is expensive to numerically integrate Equation (5.1) in time. The strategy of the method developed in Chapter 4 is to partition the size domain, in this case i, into the minimum number of sections necessary to preserve the information required in the application. For ignition and DSC applications it is desirable to retain information about the composition of the pyrolysis gas, but large species may be lumped together. The sectional moment method (see Chapter 4) used in the following divides the carbon number domain into two sections. All species with carbon number less than a critical value, l, are kept distinct and their number distribution

is evolved according to Equation (5.1). These small species will be referred to as volatiles since l is chosen to be the smallest species that does not appreciably devolatilize. In other words, the loss term in Equation (5.1) is subject to the constraint $L_i = 0$ for all $i \geq l$. All species with carbon number greater than or equal to l will be accounted for by a single notional polymer species. This notional polymer is characterized by the moments of the number distribution of the non-volatile species. Specifically, the moments describing the notional polymer are defined as

$$\mu_P^{(j)} \equiv \sum_{i=l}^{N} i^j n_i^m. \tag{6.4}$$

Applying the moment operation of Equation (6.4) to the PBE, Equation (5.1), leads to the system of equations

$$\frac{d\mu_P^{(0)}}{dt} = k^m\left[\mu_P^{(1)} - (2l-1)\mu_P^{(0)}\right], \tag{6.5a}$$

$$\frac{d\mu_P^{(1)}}{dt} = k^m\left[-(l^2 - l - 2)\mu_P^{(0)}\right], \tag{6.5b}$$

$$\frac{dn_i^m}{dt} = K_i^m - L_i, \qquad 2 \leq i < l \tag{6.5c}$$

where the kinetic terms is computed in terms of the moments as

$$K_i^m = \begin{cases} k^m\left[-(i-3)n_i^m + 2\sum_{j=i+2}^{l-1} n_j^m + 2\mu_P^{(0)}\right], & i \geq 3, \\ k^m\left[2\sum_{j=4}^{l-1} n_j^m + 2\mu_P^{(0)}\right], & i = 2. \end{cases} \tag{6.6}$$

A diagram showing the discretization of the melt phase polymer population is given in Figure 6.1.

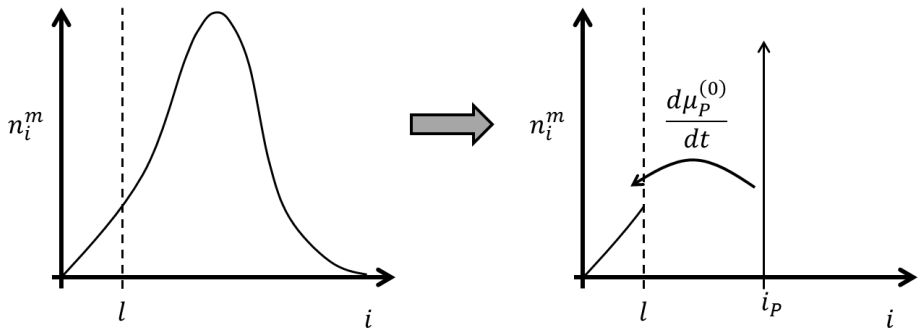

Figure 6.1: Discretized representation of the melt phase species.

The total mass and number-average MW of polymer molecules are computed as $m_P = M_0\mu_P^{(1)}$ and $M_P = m_P/\mu_P^{(0)}$ where M_0 is the molecular weight of the molecule per carbon number. For linear α-olefins, $M_0 = 14.03\ \mathrm{g/mol}$. The change in the amount of the notional polymer is due solely to losses to the volatiles, $d\mu_P^{(0)}/dt$, as is shown in Figure 6.1. It is also helpful to introduce sectional moments for the melt phase volatiles defined as

$$\mu_V^{(j)} \equiv \sum_{i=1}^{l-1} i^j n_i^m. \tag{6.7}$$

Thus the total melt phase mass is $m^m = M_0\left(\mu_P^{(1)} + \mu_V^{(1)}\right)$, and the total number of moles in the melt phase is $n^m = \mu_P^{(0)} + \mu_V^{(0)}$. The number-average MW of melt phase volatiles is $M_V = M_0\mu_V^{(1)}/\mu_V^{(0)}$.

Equations (5.35) and (6.5) constitute a combined pyrolysis and devolatilization model for linear thermoplastic thermal degradation. Both the loss and pyrolysis models were developed for HDPE, but the model should have applicability to other thermoplastics that degrade by similar mechanisms. To demonstrate the value of this combined model, it is applied to two applications in the following.

6.2 PILOTED IGNITION

The ignition time and the temperature of a material at ignition are largely dependent upon the external heating condition. A more useful quantity for characterizing the ignition of complex materials is the mass flux at ignition. The critical mass flux from the surface can be investigated theoretically using various forms of fire point equations (Rasbash et al., 1986). A fire point equation relates the mass flux needed to sustain a diffusion flame, $\dot{m}''_{F,cr}$, to the surface temperature, T_s, of the sample producing the gaseous fuel. The heat and mass transfer processes relevant to piloted ignition are shown in Figure 6.2. The fire point equation is independent of the state of the material below its surface, and it is therefore compatible with a variety of condensed phase transport models. For stoichiometric combustion, allowing for environmental heat loss, the fire point equation can be written as (Rich et al., 2007)

$$\dot{m}''_{F,cr} = \frac{h}{c_p^g} \ln\left\{1 + \frac{Y_{O,\infty}(1-\chi_r)\frac{\Delta h_c}{\nu} - c_p^g(T_s - T_\infty)}{(1-\chi_r)\Delta h_c - \frac{\nu c_p^g}{Y_{O,\infty}}\left[T_s - T_\infty + \left(1 + \frac{Y_{O,\infty}}{\nu}\right)(T_f - T_\infty)\right]}\right\}, \quad (6.8)$$

where h is the heat transfer coefficient, T_f is the flame temperature, Δh_c is the heat of combustion, c_p^g is the specific heat of the gas, χ_r is the fraction of heat lost from the flame, ν is the stoichiometric oxygen-to-fuel mass ratio for the combustion reaction, $Y_{O,\infty}$ is the mass fraction of oxygen in the free stream, and T_∞ is the free stream temperature.

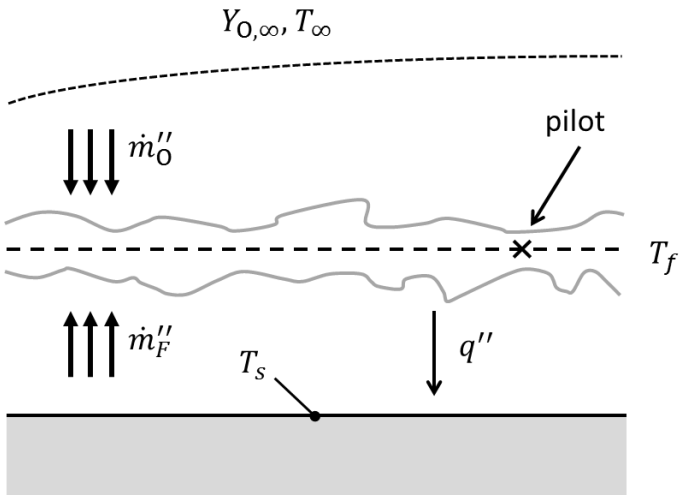

Figure 6.2: Gas phase energy and mass transfer in a piloted ignition scenario.

Atreya and Wichman (1989) derived an expression for the mass flux of pyrolysis gas out of a convectively and radiatively heated slab. Heat transfer based approaches such as this assume that the chemistry and transport are fast relative to the timescales of heat transfer within the condensed phase. It is not immediately clear that this assumption is valid in all fire scenarios. The purpose of this section is to investigate the application of more detailed population balance models to piloted ignition predictions.

Most of the experimental results for piloted ignition include measurements of critical mass flux, ignition temperature, and ignition time. The typical scenario parameter

is a constant input heat flux into the surface of the sample. Tewarson (1982) measured the critical mass flux for polyethylene on horizontal samples in natural convection to be $\dot{m}''_{F,cr} = 1.9\,\mathrm{g/m^2 \cdot s}$. Thomson and Drysdale (1987) found the ignition temperature for polyethylene to be $T_{ig} = 363 \pm 3°\mathrm{C}$. In later work, Thomson et al. (1988) had difficulty measuring the surface temperature of polyethylene because the thermocouple sank into the polymer melt. When trying to measure the critical mass flux for polyethylene, Drysdale and Thomson (1989) found that the mass loss curves were irregular, but they estimated the critical mass flux to be around $1.15 - 1.38\,\mathrm{g/m^2 \cdot s}$. Hopkins and Quintiere (1996) performed extensive experiments for the ignition of several polymers including polyethylene. This data included surface temperature histories that are useful for validating heat transfer models. Unfortunately, for the purposes of this chapter, the samples are too thick (2.5 cm) to be treated isothermally.

6.2.1 Results for HDPE

The thermal degradation model of the previous section is used to predict the mass flux of fuel out of a thermally and chemically lumped thermoplastic slab. The total fuel mass flux is related to the molar loss rates through $\dot{m}''_F = (1/A_s)\sum_i M_i L_i$. Most of the parameters in fire point equation, Equation (6.8), are constants. The following values will be used: $T_f = 1550\,\mathrm{K}$, $c_p = 1.12\,\mathrm{J/g \cdot K}$, $\chi_r = 0.1$, $T_\infty = 300\,\mathrm{K}$, $Y_{\mathrm{O},\infty} = 0.23$, and $\Delta h_c/\nu = 13.1\,\mathrm{kJ/g}$. The value of the radiative loss fraction was taken from Rich et al. (2007). Walters et al. (2000) report a net heat of combustion (lower heating value) for

polyethylene of $\Delta h_c = 44.60\,\mathrm{kJ/g}$. A nominal value of $h = 8\,\mathrm{W/m^2 \cdot K}$ was found by fitting Equation (6.8) to the experimental values of $T_{s,ig} = 363°\mathrm{C}$ and $\dot{m}''_{F,cr} = 1.9\,\mathrm{g/m^2 \cdot s}$. The RMD kinetics calculated in Chapter 3 are used as nominal values for the pyrolysis rate constant.

Two scenarios are considered: constant sample temperature and constant external heating rate. The PBE model of Equations (6.5) corresponds to a spatially uniform system. Therefore, the model is only appropriate for sufficiently small systems. Unfortunately, there is no literature data for the ignition of small samples. Since ignition is primarily controlled by the critical mass flux, it is possible to confirm the appropriateness of the model by comparison to TGA data. Note that there is nothing inherently 0^{th} order about the approach. Spatial gradients in temperature and composition were neglected in this chapter in order to test the concept for the simplest possible scenarios.

6.2.1.1 Constant Temperature

The first scenario assumes a step function temperature history so that $T(t < 0) = T_\infty$ and $T(t \geq 0) = T_S$. This scenario is sketched in Figure 6.3. The model was used to determine ignition times and mass fluxes at various sample temperatures. All of the following results correspond to an exposed sample surface area of $A_s = 50\,\mathrm{cm^2}$ and an initial HDPE number-average carbon number of $i_0 = 10^6$. The surface area and thickness

were chosen chosen to correspond to typical piloted ignition test samples as in Thomson and Drysdale (1987).

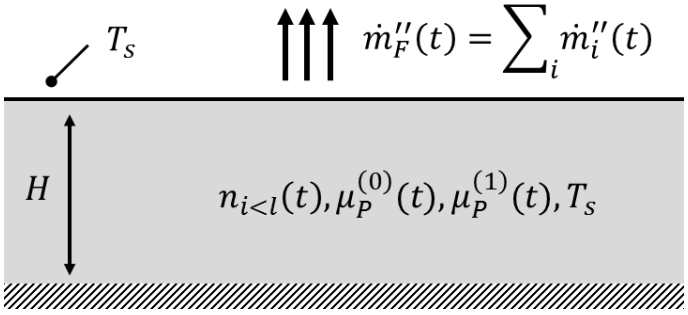

Figure 6.3: Condensed phase characterization for constant temperature piloted ignition scenario.

As a preliminary to predicting mass flux rates for piloted ignition experiments, the condensed phase mass loss coefficient (A_L in Equation (5.35)) was calibrated from isothermal TG data for HDPE from Conesa et al. (1996). This data was chosen because the low temperature at which it was obtained is comparable to ignition temperatures. It was found that the model converged to the TG data in the limit of $A_L \to \infty$. The match between the isothermal TG data and the model in this limit is shown in Figure 6.4. This result indicates that at low temperatures, the mass loss from HDPE is kinetically limited.

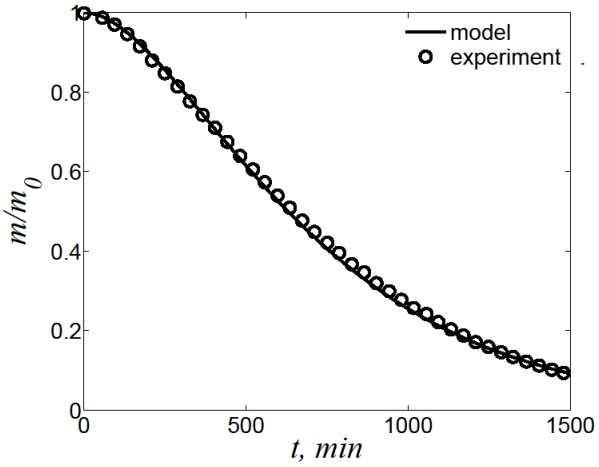

Figure 6.4: Isothermal TG simulation at $T = 385°C$ used to calibrate the condensed phase mass loss coefficient with data from Conesa et al. (1996).

For $H = 6$ mm, mass flux histories were simulated for several temperatures. The results are plotted in Figure 6.5. Also plotted in Figure 6.5 is the critical mass flux needed to achieve piloted ignition from Equation (6.8). If the predicted mass flux never equals the critical value, then the sample will not ignite. The model predicts that the 6 mm sample never ignites for temperatures less than $400°C$. The minimum ignition temperature is the temperature at which the predicted mass flux of fuel out of the sample intersects the critical mass flux line. For the 6 mm sample the minimum ignition temperature was found to be $402°C$. This is significantly higher than the reported value of $363°C$. This discrepancy cannot be attributed to differences in the heating scenario for the following reason. In the isothermal case the entire volume of the sample is generating volatile species at the same rate as at the surface. Therefore, the isothermal sample should always produce a larger mass flux than a sample in which only the surface equals this

temperature. So there must be another factor leading to the overprediction of the ignition temperature.

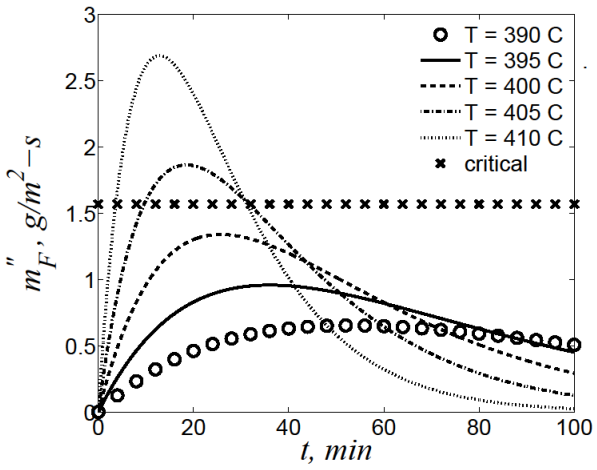

Figure 6.5: Constant temperature fuel mass flux histories at several temperatures for $H = 6$ mm.

The minimum ignition temperatures for the other two samples are $T_{ig}(4\text{ mm}) = 408°\text{C}$ and $T_{ig}(8\text{ mm}) = 398°\text{C}$. The minimum ignition temperature decreases with sample thickness because the thicker samples have more volume in which volatiles are being generated. Therefore, the thicker samples are capable of producing a sufficient amount of fuel even at lower temperatures. A consequence of this is that small samples will not ignite unless the temperature is very large. Small samples lose all of their mass before the mass flux out of the sample reaches the critical value. For non-bubbling systems, the mass loss time scales are likely significant, and the sample size will have less influence on the ignition behavior. The effect of sample size on mass flux is shown

in Figure 6.6. The thicker sample is seen to have an increasingly higher mass loss rate. This leads to shorter ignition times and lower ignition temperatures.

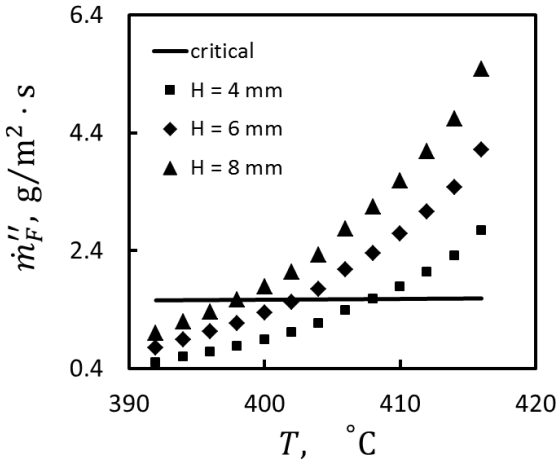

Figure 6.6: Constant temperature maximum mass fluxes as a function of temperature for several sample thicknesses.

Comparisons of ignition times across sample thicknesses are provided in Figure 6.7. Each of the three curves has a critical point corresponding to the minimum temperature at which a sample of that thickness can be ignited. Of course the same sample will be ignited at temperatures greater than this minimum temperature, and the time of ignition decreases with temperature as less time is needed to pyrolyze the polymer chains.

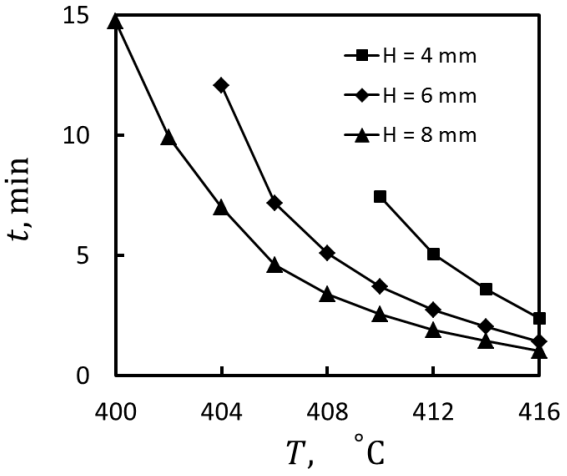

Figure 6.7: Ignition times for constant temperature samples as a function of temperature.

Finally, as was mentioned previously, a material's performance in a fire involves many coupled processes. One advantage of using PBEs to model the material in detail is that a significant amount of information about the material is preserved to better characterize these other processes. For instance, the tendency of a material to flow and drip is undesirable in fires. This tendency is primarily controlled by the viscosity which is heavily dependent on the average MW in the melt. The PBE model used in this paper provides the number-average MW, M_P. The decrease in M_P is the same for all sample thicknesses since it depends only on the temperature history. The variation of M_p versus time is plotted for $T = 408°\mathrm{C}$ in Figure 6.8. The vertical lines correspond to the ignition times of the three samples and so their intersection with $M_P(t)$ corresponds to the MW of the sample at ignition. Because the thinner samples have longer ignition times, there is more time for the polymer chains to break down and for the MW to decrease. The

number-average MWs at ignition are 724 g/mol for $H = 4$ mm, 13,900 g/mol for $H = 6$ mm, and 19,000 g/mol for $H = 8$ mm. Thus, smaller samples are more likely to be dripping at ignition for isothermal scenarios.

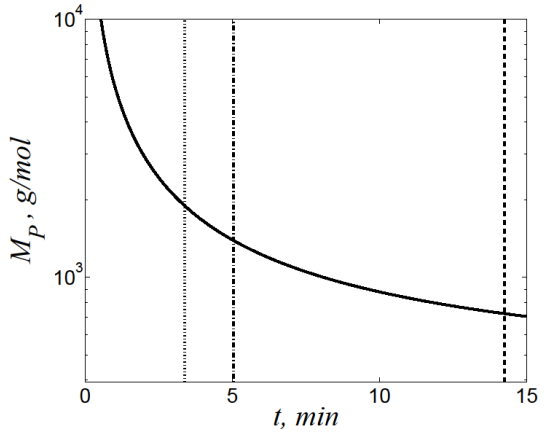

Figure 6.8: Number average MW of the polymer melt as a function of time at $T = 408°C$. The vertical lines correspond to the ignition times for sample thicknesses of 8, 6, and 4 mm (from left to right).

6.2.1.2 Constant External Heating

Better comparison to experimental data is obtained by considering the transient behavior of the sample in a constant external heating scenario. A sketch of this scenario is provided in Figure 6.9. The sample temperature may be evolved using conservation of energy

$$mc_p^s \frac{dT}{dt} = q'' A_s - hA_s(T - T_\infty), \tag{6.9}$$

where q'' is the imposed external heat flux and c_p^s is the sample specific heat. Equation (6.9) assumes that heat losses from conduction and re-radiation are negligible. For the

values of q'' and h typical in ignition experiments, the temperature ramp rate is essentially linear. Another obvious consequence of Equation (6.9) is that larger isothermal samples will heat more slowly. However, Equation (6.9) becomes increasingly invalid for large samples with significant internal temperature gradients.

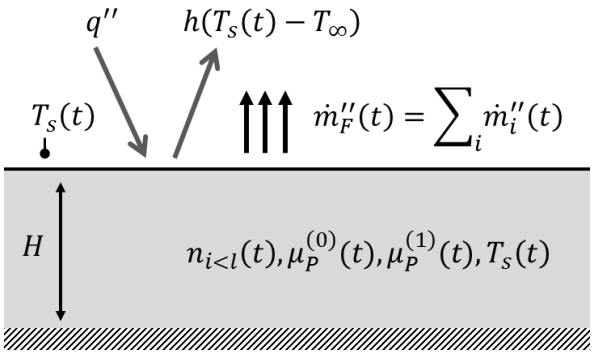

Figure 6.9: Condensed phase characterization for constant external heating piloted ignition scenario.

As was done for the constant temperature scenario, the model parameters were calibrated by comparison with TGA data. It was found that dynamic TGA data was more difficult to fit with the model, and it was necessary to tweak the kinetic parameters in addition to the loss parameter. The heating rates for ignition experiments are typically large, $\sim 150\ \mathrm{K/min}$ (Hopkins and Quintiere, 1996), and so the model was calibrated for the fastest available HDPE dynamic TGA data from Conesa et al. (1996), $100\ \mathrm{K/min}$. The fit was performed only for the initial stages of mass loss since this is the regime most comparable to ignition and the best fit is shown in Figure 6.10. The calibrated parameters are $A = 3 \times 10^{13}\ \mathrm{s^{-1}}$, $E = 215\ \mathrm{kJ/mol}$, and $A_L = 10^{-1}\ \mathrm{mol/kg \cdot s}$.

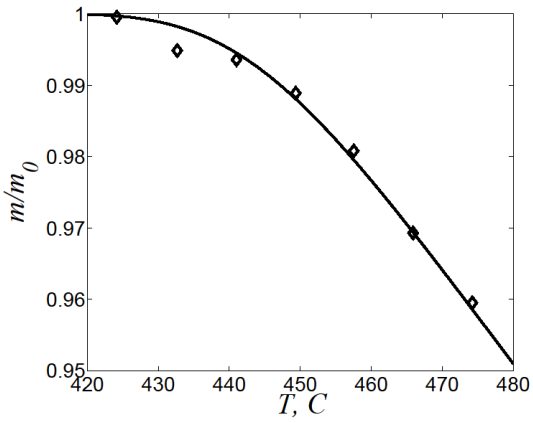

Figure 6.10: Dynamic TG simulation at 100 K/min used to calibrate model parameters.

Another interesting comparison is between TGA mass fluxes and the critical mass flux for ignition as predicted by Equation (6.8). This comparison is provided in Figure 6.11 using the dynamic data from Conesa et al. (1996). Three observations are worth pointing out. First, low heating rates will not lead to ignition. This observation is similar to what was shown for the isothermal simulations in Figure 6.5. As was explained there, this failure to ignite is due to the entire mass of the sample degrading before a critical mass flux is reached. The second important observation from Figure 6.11 is that, at least for small samples, the ignition temperature is greatly overpredicted at $T_{ig}(TGA) \approx 516°C$. This overprediction is even more pronounced than what was found in the constant temperature scenario of the previous section. Thirdly, the mass fluxes as a function of temperature for different heating rates collapse onto the same curve for the initial stages of degradation. This explains the observed independence of critical mass flux to the heating scenario.

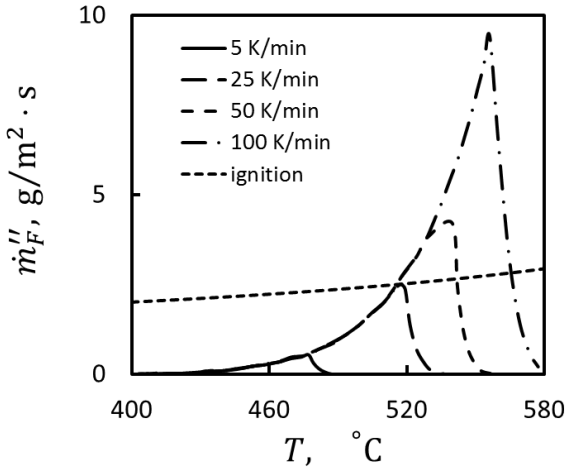

Figure 6.11: Dynamic TGA data (Conesa et al., 1996) as compared to critical mass flux for ignition from Equation (6.8).

To see if the observed overprediction in ignition temperature is due to sample size effects, the calibrated model parameters were used to predict ignition temperatures at several thicknesses. Figure 6.12 shows predicted ignition temperatures as a function of the external heating load for several sample thicknesses. Once again, it is seen that the ignition temperature decreases with sample size due to the fact that larger samples produce larger volatile fuel mass fluxes. However, even for large samples, the ignition temperature is overpredicted.

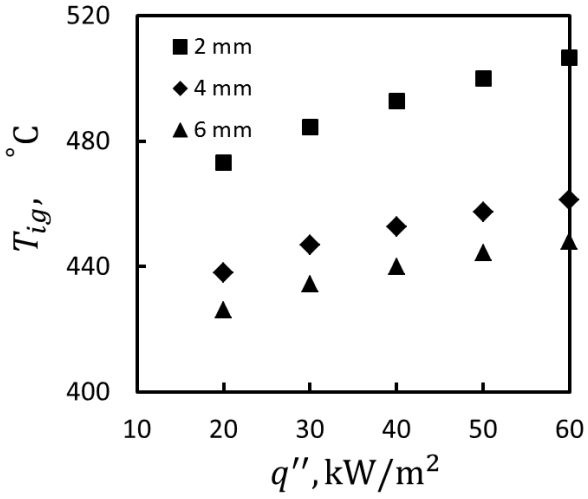

Figure 6.12: Simulated ignition temperatures versus external heating for various sample thicknesses.

Even though ignition temperatures are being consistently overpredicted, simulated ignition times are reasonable when compared to literature data as is shown in Figure 6.13. In this plot, simulated ignition times are compared to data from Thomson et al. (1988) for 6 mm thick samples at various heating loads. Since the temperatures of the sample at these ignition times is too large, the model must be overpredicting in the sample temperature at the ignition time. Since the sample is isothermal, the prediction of too rapidly increasing temperature is due to an underestimation of heat losses.

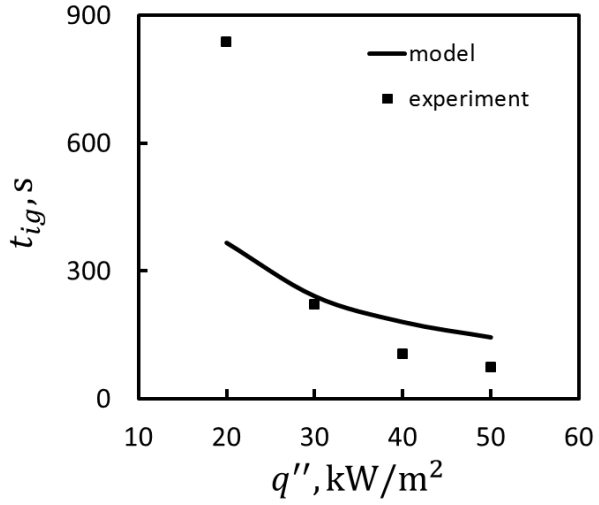

Figure 6.13: Ignition time versus external heating for 6 mm thick samples.

The most likely explanation for the failure of the calibrated model to predict ignition mass loss rates and temperatures is due to the fact that inert atmosphere TGA data were used to calibrate the kinetic and loss parameters. It has been observed that HDPE is much less stable in oxidative environments (Quackenbos, 1966). This implies that surface oxidation reactions are in fact important. Future work should take this into account.

6.2.2 Piloted Ignition Conclusions

PBEs can be used to model the complex physics of the condensed phase in fire applications. A PBE was applied to model the pyrolysis and mass loss in an isothermal slab. This model was parameterized through reactive molecular dynamics and calibration to TG data. The model was used to simulate the piloted ignition of HDPE.

Although the model overpredicts ignition temperature in constant temperature scenarios, several helpful observations were made. First, the low temperature TGA calibration indicates that in piloted ignition conditions devolatilization is fast relative to pyrolysis. This would indicate that detailed mass loss modeling is unimportant for studying piloted ignition (at least at low temperatures). However, the model provides information about the pyrolysis gas composition and this might be useful for accurate modeling of gas phase combustion.

The transiently heated results also result in an overprediction of ignition temperatures and mass fluxes. Despite this, the predicted ignition times agree fairly well with experimental data. This felicitous success is attributed to an overprediction in the sample temperature ramp rate due to an underprediction in surface heat losses. Slower devolatilization and faster heat loss are needed for the model to consistently agree with both experimental ignition times and temperatures.

Model parameters were calibrated using isothermal and dynamic TGA data. In both cases, it was found that the model reproduced the data very well. However, the TGA data indicates that HDPE is much more stable than the ignition experiments indicate. The best explanation of this discrepancy is that inert environment TGA data is inappropriate for calibrating mass loss for oxidative environment ignition experiments. Since the model presented in this paper does not take into account surface oxidation, further modifications are needed for the techniques presented here to accurately predict ignition behavior.

There is a great deal of opportunity for future work. Of primary importance is including a surface oxidation component to the mass loss model. Heat transfer models can be introduced to make the PBE approach applicable to thicker samples. The model should also be validated against other polymers with different pyrolysis and devolatilization mechanisms.

6.3 DIFFERENTIAL SCANNING CALORIMETRY

The measured quantity in DSC experiments is the difference in heat input rates between the sample and reference cells. The quantity of interest is the energy absorption rate. A proper analysis of DSC data requires a data reduction model for predicting the energy absorption rate as a function of the differential heat input rates. The goal of this section is to develop and test a detailed, PBE-based model for DSC experiments with thermally degrading HDPE samples.

The DSC experiment can be modeled as two separate cells for the sample pan and the reference pan. These cells and the relevant control volumes are sketched in Figure 6.14. The reference cell contains static control volumes for the pan (including the cover) and the inert purge gas. In place of a single gas phase control volume, the sample cell contains moving control volumes for the melt and gas phases. In the model development, it will be convenient to work with masses in the reference cell and mole numbers in the sample cell. Simulation of a DSC experiment requires conservation of mass and energy equations for each of these control volumes.

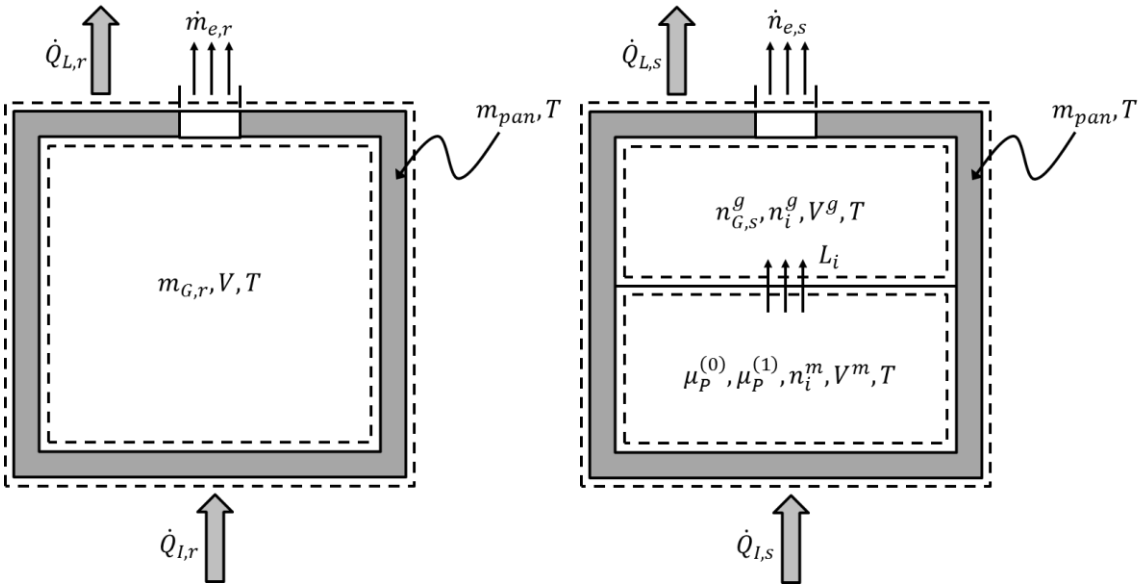

Figure 6.14: Control volumes for integral analysis of DSC experiments.

The measured quantity in a DSC experiment is the differential heat input $\Delta\dot{Q}_I(t) \equiv \dot{Q}_{I,s} - \dot{Q}_{I,r}$. Heat inputs into the separate cells are controlled so that the temperatures of both cells are equal. Because there are significant thermal events occurring in the sample cell, the differential heat input will not be zero.

The modeling equations needed for simulating DSC experiments are derived below. The resultant models contain relatively few parameters, and estimates for these parameters are determined from the literature. Finally, simulations of DSC for HDPE are performed and compared to literature data.

6.3.1 DSC Modeling

Pyrolysis and loss in the sample melt phase are governed by Equations (6.5) and (5.35). In addition to these equations, several additional models are needed in order to simulate a DSC experiment. Global conservation of mass and energy equations are needed for the reference and sample cells. Several simplifying assumptions can be made at this point. Because the DSC cells are small, spatial variations in temperature are neglected. Furthermore, within any of the control volumes (e.g., the sample cell melt phase) there are no spatial variations of bulk or species densities.

6.3.1.1 Reference Cell

The only mass transfer in the reference cell is a small gas flow out due to expansion as the gas is heated. The gas inside of the pan is just the purge gas (e.g. nitrogen). It is assumed purge gas is ideal so that the mass is a function of the temperature only

$$m_{G,r} = \frac{PM_G V}{RT}, \tag{6.10}$$

where M_G is the molecular weight of the inert purge gas. The mass flow rate out of the sample cell is just the negative of the time derivative of Equation (6.10)

$$\dot{m}_{e,r} = -\frac{dm_{G,r}}{dt} = \frac{PM_G V}{RT^2}\frac{dT}{dt}, \tag{6.11}$$

where the subscript e refers to the exit of the cell.

Since there are no thermal events occurring in the reference cell, all of the heat transfer goes toward heating the pan and the purge gas. It will be assumed that the

pressure is always equal to atmospheric pressure in both the reference and sample cells. The validity of this assumption depends upon the mass loss rate being sufficiently low and the pan exit area being sufficiently large. A consequence of the constant pressure assumption is that changes in total internal energy are equal to changes in total enthalpy, or $dU = dH$, within each cell. Neglecting the kinetic energy of the exiting gas, conservation of energy for the sample cell is

$$\frac{dH_r}{dt} = \dot{Q}_{net,r} - \dot{m}_{e,r} h_G, \tag{6.12}$$

where H_r is the total enthalpy of the reference cell, $\dot{Q}_{net,r} \equiv \dot{Q}_{I,r} - \dot{Q}_{L,r}$ is the net heat transfer into the reference cell, and h_G is the specific enthalpy of the purge gas. The reference cell internal energy may be divided into the internal energy of the purge gas within the pan and the internal energy of the pan, or $H_r = H_{G,r} + H_{pan}$. Since the mass and composition of the pan are constant, $dH_{pan} = C_{pan} dT$ where C_{pan} is the total heat capacity of the pan. This heat capacity is easily calculated from the mass of the pan as $C_{pan} = m_{pan} c_{p,pan}$. Decomposing the internal energy of the purge gas gives $dH_{G,r} = m_{G,r} dh_G + h_G dm_{G,r}$ where h_G is the mass specific enthalpy of the purge gas. Using the fact that $dh_G = c_{p,G} dT$ and $dm_{G,r}/dt = -\dot{m}_{e,r}$, Equation (6.12) may be rewritten as

$$\dot{Q}_{net,r} = \left(C_{G,r} + C_{pan}\right) \frac{dT}{dt}, \tag{6.13}$$

where $C_{G,r} \equiv m_{G,r} c_{p,G}$. The total heat capacity of the reference cell purge gas may be rewritten using Equation (6.10) as

$$C_{G,r} = \frac{PVM_G c_{p,G}}{RT}. \tag{6.14}$$

Typically, DSC experiments are constant heating rate so that $dT/dt = \beta$ and $T(t) = T_0 + \beta t$ where T_0 is the initial temperature of the reference cell. In constant heating scenarios, these parameters may be substituted into Equation (6.13) to obtain the heat flow into the reference cell as a function of time or temperature.

6.3.1.2 Sample Cell

The sample cell is more difficult to model because of the chemical reactions and mass transfer occurring within the cell. The volatile molecules can exist in the gas phase and as a solute in the melt phase while the notional polymer only exists in the melt. The gas phase will be treated as an ideal mixture composed of the volatile species and the purge gas. These species are assumed to pyrolyze by the same mechanism as Equation (6.1) at a different rate, k^g, than the melt phase pyrolysis reactions. Volatile species are transported to the gas phase at a rate of L_i and they are lost from the sample pan due to gas expansion. The conservation of olefin species in the gas phase can be written as

$$\frac{dn_i^g}{dt} = K_i^g + L_i - \dot{n}_{e,s} X_i^g, \qquad i = 2, \ldots, l-1 \tag{6.15}$$

where

$$K_i^g \equiv \begin{cases} k^g \left[-(i-3)n_i^g + 2\sum_{j=i+2}^{l-1} n_j^g \right], & i \geq 3 \\ 2k^g \sum_{j=4}^{l-1} n_j^g, & i = 2 \end{cases} \tag{6.16}$$

$\dot{n}_{e,s}$ is the total molar flow rate out of the sample cell, and X_i^g is the mole fraction of species i in the gas phase. The gas phase kinetic rates of Equation (6.16) are of the same form as the melt phase kinetic rates of Equation (6.3) with the exception of the contribution from the moments representing the polymer species since there are no non-volatile polymer species in the gas phase. Under the assumption of constant pressure, the amount of purge gas in the sample cell, $n_{G,s}^g$, may be computed from the number of gas phase olefins through

$$n_{G,s}^g = \frac{PV}{RT} - \sum_{i=1}^{l-1} n_i^g. \tag{6.17}$$

An expression for the unknown molar flow rate, $\dot{n}_{e,s}$, can be obtained by considering the conservation equation for the total number of moles in the gas phase of the sample cell. The time rate of change of the total number of gas phase moles, $n_s^g \equiv n_{G,s}^g + \sum_i n_i^g$, is equal to the rate at which moles are lost from the cell through the outlet plus the rate at which they are generated through pyrolysis plus the rate at which they enter the gas phase through the loss mechanism. This may be stated mathematically as

$$\frac{dn_s^g}{dt} = -\dot{n}_{e,s} + \sum_{i=2}^{l-1} \left(K_i^g + L_i \right). \tag{6.18}$$

Since the gas is assumed to be ideal, the time rate of change of the total number of gas phase moles may be computed as

$$\frac{dn_s^g}{dt} = \frac{d}{dt}\left(\frac{PV^g}{RT}\right) = \frac{P}{RT}\left(\frac{dV^g}{dt} - \frac{V^g}{T}\frac{dT}{dt}\right). \tag{6.19}$$

Substituting Equations (6.16) and (6.19) into Equation (6.18) and solving for the total molar outflow rate yields

$$\dot{n}_{e,s} = \frac{P}{RT}\left(\frac{V^g\beta}{T} - \frac{dV^g}{dt}\right) + k^g\sum_{i=4}^{l-1} n_i^g(i-3) + \sum_{i=2}^{l-1} L_i. \tag{6.20}$$

The volume occupied by the gas is known if the volume occupied by the melt phase is known since the total volume is constant, $V = V^m + V^g$. It will be assumed that the density of the melt phase, ρ^m, changes slowly relative to the mass loss rate. Therefore, the gas volume and its time rate of change are

$$V^g = V - \frac{m^m}{\rho^m}, \tag{6.21a}$$

$$\frac{dV^g}{dt} = \frac{M_0}{\rho^m}\sum_{i=2}^{l-1} iL_i. \tag{6.21b}$$

since $V^m = m^m/\rho^m$.

As was the case for the reference cell, changes in sample cell internal energy equal changes in sample cell enthalpy, $dU_s = dH_s$. This is a consequence of the constant pressure and volume within the cell, and so conservation of energy for the sample cell is

$$\frac{dH_s}{dt} = \dot{Q}_{net,s} - \dot{n}_{e,s}\bar{h}_s^g, \tag{6.22}$$

where $\bar{h}_s^g$ is the molar enthalpy of the sample cell gas and the kinetic energy of the exiting gas is neglected. Assuming that the gas phase is an ideal mixture, the purge gas and gas phase alkene enthalpies are additive so that

$$H_s = H_{pan} + H_{G,s}^g + H_O^g + H_O^m, \tag{6.23}$$

where H_{pan} is the enthalpy of the sample pan, $H_{G,s}^g$ is the enthalpy of the purge gas in the sample cell, H_O^g is the enthalpy of the gas phase olefins, and H_O^m is the total enthalpy of the melt phase olefins. The gas phase alkene enthalpy may be further decomposed into the enthalpies of the individual species

$$H_O^g = \sum_{i=2}^{l-1} H_i^g, \tag{6.24}$$

since it is assumed that the gas phase is an ideal mixture. The melt phase is not an ideal solution, and so the total melt phase enthalpy must include an enthalpy change associated with the mixing of its components. This mixing enthalpy is a thermodynamic property and so it depends on the pressure, temperature, and composition of the melt phase. Representing the composition as a vector of melt phase moles, $\mathbf{n}^m \equiv [n_2^m\ n_3^m \cdots n_N^m]^{\mathrm{T}}$, the total melt phase enthalpy can be expressed as

$$H_O^m = \left(\sum_{i=2}^{N} H_i^m \right) + \Delta H_{mix}(T, \mathbf{n}^m), \tag{6.25}$$

where the pressure dependency of the mixing enthalpy is neglected since DSC is a constant pressure experiment.

The conservation of energy equation (Equation (6.22)) requires the time derivative of the total sample cell enthalpy. Therefore, it is necessary to determine the differentials of the terms on the right-hand side of Equation (6.23). It is assumed that the sample cell pan is identical to the reference cell pan so that $dH_{pan} = C_{pan}dT$.

$$\frac{dH_{pan}}{dt} = C_{pan}\frac{dT}{dt}. \tag{6.26}$$

The purge gas enthalpy can be decomposed using molar specific enthalpies so that $dH_{G,s}^{g} = n_{G,s}^{g}d\bar{h}_G + \bar{h}_G dn_{G,s}^{g} = n_{G,s}\bar{c}_{p,G}dT + \bar{h}_G dn_{G,s}^{g}$ where $\bar{c}_{p,G}$ is the constant pressure molar specific heat. The time derivative of this enthalpy is thus

$$\frac{dH_{G,s}^{g}}{dt} = n_{G,s}^{g}\bar{c}_{p,G}\frac{dT}{dt} - \bar{h}_G X_{G,s}\dot{n}_{e,s}, \tag{6.27}$$

since the time rate of change of moles of the purge gas is $-X_{G,s}\dot{n}_{e,s}$. For olefin species i in the gas phase, the total differential enthalpy is $dH_i^g = n_i^g\bar{c}_{p,i}dT + \bar{h}_i dn_i^g$. The molar specific enthalpy, $\bar{h}_i$, is defined as the enthalpy of species i in the ideal gas state. The time rate of change of n_i^g is provided by Equation (6.15). The time rate of change of gas phase olefin enthalpies is

$$\frac{dH_O^g}{dt} = \frac{d}{dt}\left(\sum_{i=2}^{l-1}H_i^g\right) = \sum_{i=2}^{l-1}\left[n_i^g\bar{c}_{p,i}\frac{dT}{dt} + \bar{h}_i\left(K_i^g + L_i - X_i^g\dot{n}_{e,s}\right)\right]. \tag{6.28}$$

Similarly, the differential of the total melt phase enthalpy is

$$dH_O^m = \sum_{i=2}^{N}\left(n_i^m\bar{c}_{p,i}dT + \bar{h}_i dn_i^m\right) + d[\Delta H_{mix}(T, \mathbf{n}^m)]. \tag{6.29}$$

At this point, it becomes necessary to model the total mixture enthalpy of the melt phase. A first order model is the linear form

$$\Delta H_{mix}(T, \mathbf{n}^m) = \sum_{i=2}^{N} \Delta \bar{h}_{mix,i}(T) n_i^m \tag{6.30}$$

where $\Delta \bar{h}_{mix,i}(T)$ is the enthalpy required to mix one mole of species i as an ideal gas into the melt phase. The physical assumption corresponding to the linear form of Equation (6.30) is that the molar specific enthalpy of mixing is independent of the composition of the melt phase. This assumption is reasonable since the bulk phase melt phase is composed of chemically and structurally similar molecules. In terms of the intermolecular forces, the environment that the melt phase provides to a mixed (or dissolved) molecule is largely independent of the details of the melt phase composition. The differential of the linear form for the total mixing enthalpy becomes

$$d[\Delta H_{mix}(T, \mathbf{n}^m)] = \sum_{i=2}^{N} \left(n_i^m \Delta \bar{c}_{mix,i} dT + \Delta \bar{h}_{mix,i} dn_i^m \right) \tag{6.31}$$

where $\Delta \bar{c}_{mix,i} \equiv d\left(\Delta \bar{h}_{mix,i}\right)/dT$. Substituting Equation (6.31) into Equation (6.29), dividing through by dt and using Equation (6.2) for the time derivative of n_i^m results in

$$\frac{dH_O^m}{dt} = \sum_{i=2}^{N} \left[\left(\bar{c}_{p,i} + \Delta \bar{c}_{mix,i} \right) n_i^m \frac{dT}{dt} + \left(\bar{h}_i + \Delta \bar{h}_{mix,i} \right) \left(K_i^m - L_i \right) \right]. \tag{6.32}$$

The left-hand side of Equation (6.22) is equal to the sum of Equations (6.26), (6.27), (6.28), and (6.32). Making these substitutions, conservation of energy for the sample cell may be rewritten as

$$\dot{Q}_{net,s} = \left(C_{pan} + C_{G,S}^{g} + C_{O}^{g} + C_{O}^{m}\right)\frac{dT}{dt} + \dot{Q}_{dev} + \dot{Q}_{pyr}^{g} + \dot{Q}_{pyr}^{m}, \tag{6.33}$$

where

$$C_{G,s}^{g} \equiv \bar{c}_{p,G} n_{G,s}^{g}, \tag{6.34}$$

is the total heat capacity of the purge gas,

$$C_{O}^{g} \equiv \sum_{i=2}^{l-1} \bar{c}_{p,i} n_{i}^{g}, \tag{6.35}$$

is the total heat capacity of olefins in the gas phase,

$$C_{O}^{m} \equiv \sum_{i=2}^{N} \left(\bar{c}_{p,i} + \Delta\bar{c}_{mix,i}\right) n_{i}^{m}, \tag{6.36}$$

is the total heat capacity of olefins in the melt phase,

$$\dot{Q}_{dev} \equiv -\sum_{i=2}^{l-1} \Delta\bar{h}_{mix,i} L_{i}, \tag{6.37}$$

is the energy absorbed by devolatilization,

$$\dot{Q}_{pyr}^{g} \equiv \sum_{i=2}^{l-1} \bar{h}_{i} K_{i}^{g}, \tag{6.38}$$

is the energy absorbed by gas phase pyrolysis, and

$$\dot{Q}_{pyr}^{m} \equiv \sum_{i=2}^{N} \left(\bar{h}_{i} + \Delta\bar{h}_{mix,i}\right) K_{i}^{m}, \tag{6.39}$$

is the energy absorbed by melt phase pyrolysis. In words, Equation (6.33) says that the neat heat transfer into the sample cell goes into (1) sensible heating, (2) devolatilizing volatile olefins from the melt phase, and (3) pyrolyzing the olefins in both melt and gas

phases. The enthalpy loss due to gas exiting the sample cell is eliminated from both sides of the conservation of energy equation. It is clear from Equation (6.36), that $\Delta\bar{c}_{mix,i}$ is the correction to the ideal gas specific heat capacity associated with dissolving species i into the melt phase. This correction represents the energy stored in weak intermolecular bonds and should be small compared to the energy storage in the intramolecular covalent bonds.

In addition to the models for pyrolysis and devolatilization (K_i^m, K_i^g, L_i), evaluation of the terms in Equation (6.33) requires several thermodynamic properties for each olefin species. Since the total number of species is large, it is infeasible to determine these properties experimentally. To overcome this limitation, group additivity of thermodynamic properties (Benson, 1976; van Krevelen and te Nijenhuis, 2009) is utilized in the following. The underlying principle of group additivity is that the properties of a molecule may be estimated by summing contributions from small groups of atoms composing the molecule. A group is defined as a polyvalent atom and its atoms. Since all of the molecules are linear α-olefins, the only groups that need to be accounted for are methyl ($(\mathrm{C})-\mathrm{CH}_3$), alkyl ($(\mathrm{C})-\mathrm{CH}_2-(\mathrm{C})$), and "ethyl" groups ($(\mathrm{C})-\mathrm{CH}=\mathrm{CH}_2$). The "ethyl" group is introduced for convenience. It is not a true group since it contains two polyvalent atoms. The decomposition of an i carbon number olefin, O_i, into these three basic groups is sketched in Figure 6.15. An α-olefin with i carbon atoms contains one methyl (M) group, $i-3$ alkyl (A) groups, and one ethyl (E) group.

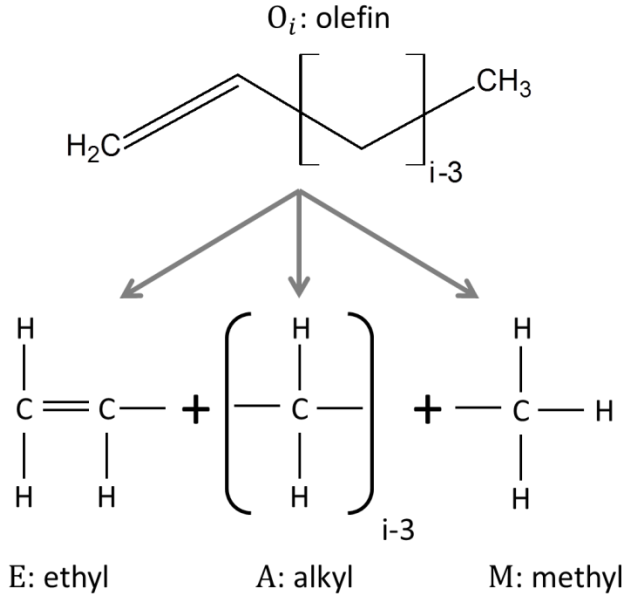

Figure 6.15: Group decomposition of linear α-olefin molecules.

In addition to α-olefins, ethylene molecules are also formed during pyrolysis. Ethylene molecules are different from the previously defined ethyl groups by a single hydrogen atom. This difference is significant, however. For instance, using group properties tabulated in Benson (1976), the enthalpies of formation (at 1 atm and 298 K) for ethyl and ethylene are 62.1 and 52.4 kJ/mol (see Table 6.1). It is therefore necessary to introduce an additional pseudo-group for ethylene molecules.

For species i, the ideal gas enthalpies of formation and molar specific heats can be computed in terms of group properties as

$$\Delta\bar{h}^{\circ}_{f,i} = \begin{cases} \Delta\bar{h}^{\circ}_{f,M} + (i-3)\Delta\bar{h}^{\circ}_{f,A} + \Delta\bar{h}^{\circ}_{f,E}, & i \geq 3 \\ \Delta\bar{h}^{\circ}_{f,E^*}, & i = 2 \end{cases} \tag{6.40a}$$

$$\bar{c}_{p,i} = \begin{cases} \bar{c}_{p,M} + (i-3)\bar{c}_{p,A} + \bar{c}_{p,E}, & i \geq 3 \\ \bar{c}_{p,E^*}, & i = 2 \end{cases} \tag{6.40b}$$

where the subscripts M, A, E, and E^* denote methyl, alkyl, ethyl, and ethylene group properties. The enthalpies of formation correspond to a standard state of $T = 298$ K and a pressure of one atmosphere. The group molar specific heats are temperature dependent. The temperature dependent molar specific enthalpy of species i is calculated in terms of the enthalpy of formation and the molar specific heat capacity as

$$\bar{h}_i(T) = \Delta\bar{h}^\circ_{f,i} + \int_{298}^{T} \bar{c}_{p,i}(T')dT'. \tag{6.41}$$

In addition to these gas phase thermodynamic properties, the terms of Equation (6.33) also depend on corrections associated with mixing the molecules into the melt phase, $\Delta\bar{c}_{p,i}$ and $\Delta\bar{h}_{mix,i}$. Because of a lack of data on these parameters, it will be assumed that $\Delta\bar{c}_{p,i} = 0$ for all species, and $\Delta\bar{h}_{mix,i} = 0$ for the non-volatile species ($i \geq l$). It is likely that simple corrections could be used in future work to account for the differences in heat capacity between the phases (Pavlinov et al., 1984).

The group additivity model, along with the two simplifying assumptions stated above, allows the right-hand side of Equation (6.33) to be computed in terms of known quantities. Specifically, the total heat capacity of olefins in the gas phase is

$$C_O^g = \bar{c}_{p,E^*} n_2^g + \left(\bar{c}_{p,M} - 3\bar{c}_{p,A} + \bar{c}_{p,E}\right) \sum_{i=3}^{l-1} n_i^g + \bar{c}_{p,A} \sum_{i=3}^{l-1} i n_i^g, \tag{6.42}$$

the total heat capacity of olefins in the melt phase is

$$C_O^m = \bar{c}_{p,E^*} n_2^m + \left(\bar{c}_{p,M} - 3\bar{c}_{p,A} + \bar{c}_{p,E}\right)\left(\mu_P^{(0)} + \sum_{i=3}^{l-1} n_i^m\right) + \bar{c}_{p,A}\left(\mu_P^{(1)} + \sum_{i=3}^{l-1} i n_i^m\right), \tag{6.43}$$

the energy absorbed by gas phase pyrolysis is

$$\dot{Q}_{pyr}^g = \bar{h}_{E^*} K_2^g + \left(\bar{h}_M - 3\bar{h}_A + \bar{h}_E\right)\sum_{i=3}^{l-1} K_i^g + \bar{h}_A \sum_{i=3}^{l-1} i K_i^g, \tag{6.44}$$

and the energy absorbed by melt phase pyrolysis is

$$\dot{Q}_{pyr}^m = \left(\bar{h}_{E^*} + \Delta\bar{h}_{mix,2}\right)K_2^m + \left(\bar{h}_M - 3\bar{h}_A + \bar{h}_E\right)\left(\frac{d\mu_P^{(0)}}{dt} + \sum_{i=3}^{l-1} K_i^m\right) + \bar{h}_A\left(\frac{d\mu_P^{(1)}}{dt} + \sum_{i=3}^{l-1} i K_i^m\right) + \sum_{i=3}^{l-1} \Delta\bar{h}_{mix,i}\, K_i^m. \tag{6.45}$$

These equations have been written in terms of known or previously computed quantities.

6.3.1.3 Model Summary

The net heat transfer into the reference and sample cells may be computed by Equations (6.13) and (6.33). Separating the net heat fluxes into input and loss components ($\dot{Q}_{net} = \dot{Q}_I - \dot{Q}_L$), the DSC output is computed as

$$\Delta\dot{Q}_I = \left(C_{G,s}^g + C_O^g + C_O^m - C_{G,r}\right)\frac{dT}{dt} + \dot{Q}_{dev} + \dot{Q}_{pyr}^g + \dot{Q}_{pyr}^m + \Delta\dot{Q}_L. \tag{6.46}$$

where $\Delta\dot{Q}_I \equiv \dot{Q}_{I,s} - \dot{Q}_{I,r}$ and $\Delta\dot{Q}_L \equiv \dot{Q}_{L,s} - \dot{Q}_{L,r}$. Equation (6.46) involves a number of scenario parameters and material properties. The scenario parameters are fairly well-

controlled by the experimentalist. Ideally, the heat losses of the two cells should be equal so that $\Delta\dot{Q}_L = 0$. There is evidence to suggest that this is not the case in practice (Stoliarov, 2008). The differential heat loss rate may be measured by running a DSC experiment with an empty sample pan—in this scenario, $\Delta\dot{Q}_I = \Delta\dot{Q}_L$. Evaluation of the material properties appearing in the terms of Equation (6.46) will be discussed in the next section.

6.3.2 Material Properties for HDPE

The model developed in the previous section is simple enough to require relatively few material properties. For the reference cell, the governing equations require the specific heat and the molecular weight of the purge gas. Nitrogen is the most common purge gas for DSC experiments, and so $M_G = 28.01\ \mathrm{g/mol}$. Tabulated values of the constant pressure mass specific heat of N_2 gas were obtained from Mills (1999) at temperatures from $250 - 1500$ K. Linear interpolation was used to estimate values of $c_{p,G}$ at temperatures between the tabulated temperatures.

In comparison to the reference cell, the sample cell mass and energy equations require a relatively large number of material properties to be specified. The kinetic terms require pyrolysis rates for both the melt and gas phases, k^m and k^g. The proposed mechanism is a composite reaction involving a homolytic chain scission and a disproportionation. Assuming that the disproportionation is fast relative to the scission, the needed pyrolysis rates can be estimated from chain initiation rates, that is $k^m \approx k^i$.

Specification of the pyrolysis rates as a function of temperature requires a pre-exponential and an activation energy for both phases. As was discussed in Chapter 3, there is much uncertainty in predicting condensed phase reaction rates. Ranzi et al. (1997) have proposed that condensed phase rates can be estimated by a correction to gas phase activation energies. For chain intiation reactions, Ranzi et al. estimate the gas phase and melt phase activation energies to be 343 kJ/mol and 321 kJ/mol or a correction of $E^g - E^m = 22\ \mathrm{kJ/mol}$. From the analysis and discussion of Chapter 3, it would appear that these activation energies are too large. Therefore, in the following, the RMD value of $E^m = 251\ \mathrm{kJ/mol}$ will be used. The gas phase value was determined by correcting E^m by the same amount as Ranzi et al. to get $E^g = 273\ \mathrm{kJ/mol}$. Finally, it is assumed that the reaction rates in both phases have the RMD determined pre-exponential of $A = 10^{14.6}\ \mathrm{s}^{-1}$.

The multicomponent bubbling loss of Equation (5.35) was used to model L_i. The only parameters are the loss constant, A_L, and the critical carbon number, l. A value of $A_L = 10^{-4}$ was determined based on calibration to dynamic TGA data. The loss rates for $i > 20$ were negligibly small and so $l = 20$ was used in the simulations.

Group thermodynamic properties are needed to compute enthalpies and heat capacities in the sample cell conservation of energy equation. The relevant group properties are tabulated in Table 6.1 using data found in Benson (1976). Specific heat capacities at given temperatures are found by linear interpolation on the data in Table 6.1.

Similarly, specific enthalpies as a function of temperature are found by piecewise integration of the interpolated specific heat function.

	$\Delta\bar{h}_f^\circ$, kJ/mol	$\bar{c}_p$, J/mol · K					
		300 K	400 K	500 K	600 K	800 K	1000 K
Metyhl, M	−42.68	25.9	32.8	39.3	45.1	54.5	61.8
Alkyl, A	−20.6	23.0	29.1	34.5	39.1	46.3	51.6
Ethyl, E	62.1	38.7	47.7	55.7	62.8	74.1	82.5
Ethylene, E^*	52.4	42.7	53.2	62.8	71.1	84.3	94.3

Table 6.1: Group thermodynamic properties for linear α-olefins.

Under the assumptions of the previous section, the only thermodynamic property associated with mixing that is needed is the molar specific enthalpy of mixing for the volatile olefins, $\Delta\bar{h}_{mix,i}$ for $i < l$. Unfortunately, it seems that there is no literature data for this property. An alternative to experimental data is to use thermodynamic principles to relate the mixing enthalpy with the Henry's constant. Correlations for Henry's constant are available in the literature (Equation (5.35)), and the relationship to mixing enthalpy is derived as follows. The fugacity of species i in a mixture, f_i, is related to the mixing enthalpy through (Prausnitz et al., 1999)

$$\left(\frac{\partial \ln f_i}{\partial T}\right)_{P,\mathbf{X}^m} = -\frac{\Delta\bar{h}_{\mathrm{mix},i}}{RT^2}, \tag{6.47}$$

where $\mathbf{X}^m$ is the vector of mole fractions for species present in the mixture. For ideal solutions in which Henry's Law is valid, $f_i = H_{X,i}X_i^m$. Therefore,

$$\left(\frac{\partial \ln f_i}{\partial T}\right)_{P,\mathbf{X}^m} = \left(\frac{\partial \ln H_{X,i}}{\partial T}\right)_{P,\mathbf{X}^m} + \left(\frac{\partial \ln X_i^m}{\partial T}\right)_{P,\mathbf{X}^m}. \tag{6.48}$$

Since the last term in Equation (6.48) is zero, substitution into Equation (6.47) gives

$$\Delta\bar{h}_{\mathrm{mix},i} = -RT^2\left(\frac{\partial \ln H_{X,i}}{\partial T}\right)_{P,\mathbf{X}^m}. \tag{6.49}$$

Thus, if the temperature variation of the Henry's constant is known for species i dissolved in the polymer melt, then the mixing enthalpy is computable.

A correlation (Equation (5.35)) for the weight fraction Henry's constant, $H_{W,i}(T)$, for small hydrocarbons in polyethylene was developed by Maloney and Prausnitz (1976). Taking the natural logarithm of Equation (5.35) and then the derivative with respect to T at constant pressure and composition results in

$$\left(\frac{\partial \ln H_{W,i}}{\partial T}\right)_{P,\mathbf{X}^m} = 2.303\left(\frac{\partial g_i^{(0)}}{\partial T} + \omega_i \frac{\partial g_i^{(1)}}{\partial T}\right). \tag{6.50}$$

Since $H_{W,i}W_i = H_{X,i}X_i$,

$$\left(\frac{\partial \ln H_{W,i}}{\partial T}\right)_{P,\mathbf{X}^m} = \left(\frac{\partial \ln H_{X,i}}{\partial T}\right)_{P,\mathbf{X}^m}. \tag{6.51}$$

Taking the temperature derivatives of $g_i^{(0)}$ and $g_i^{(1)}$ from Equations (5.36), substituting into Equation (6.50), and making use of Equations (6.49) and (6.51) leads to

$$\Delta\bar{h}_{\mathrm{mix},i}(T) = -(18.81 + 43.38\omega_i)\frac{T_{c,i}^2}{T} - (26.49 - 9.216\omega_i)T_{c,i} + 7111. \tag{6.52}$$

where the units of all temperatures are in Kelvin, and the units of the enthalpy of mixing are J/mol. Correlations for $T_{c,i}$ and ω_i for α-alkenes are provided by Equations (5.37) and (5.38).

Plots of Equation (6.52) as a function of temperature are shown as lines in Figure 6.16. The top line corresponds to 1-butene ($i = 4$), and the bottom line corresponds to 1-octene ($i = 8$). The markers correspond to the enthalpies of vaporization of the volatiles as pure substances. It is seen that mixing small hydrocarbons into the polyethylene melt results in a net enthalpy decrease in the system, and so mixing is exothermic. Conversely, the removal of small hydrocarbons from the polyethylene melt increases the system enthalpy, and so devolatilization is an endothermic process. An enthalpy of devolatilization may be defined as $\Delta\bar{h}_{dev,i} \equiv -\Delta\bar{h}_{mix,i}$ where $\Delta\bar{h}_{dev,i} > 0$ and $\Delta\bar{h}_{mix,i} < 0$. It is clear from Figure 6.16 that the larger the volatile the more heat is released upon mixing into the polymer melt. Conversely, more heat is required to devolatilize larger volatiles as compared to smaller ones. This observation is explained by the fact that larger molecules in the condensed phase, because of their larger surface area, experience a larger total intermolecular force. The enthalpy of devolatilization is equal to the energy required to overcome this intermolecular force, and so it is larger for larger molecules. The other obvious trend for the mixing enthalpies in Figure 6.16 is that the magnitude of the enthalpy change decreases with increasing temperature.

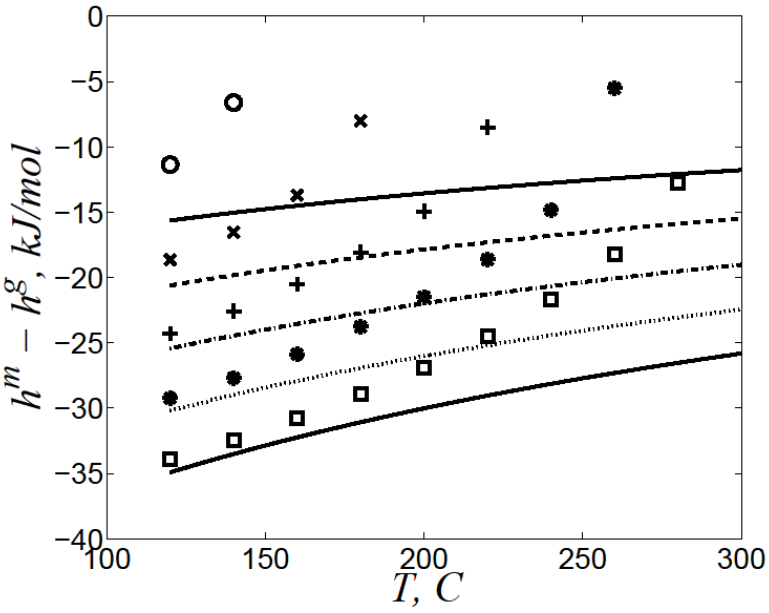

Figure 6.16: Enthalpies of mixing for volatiles in HDPE (lines) and in a pure volatile liquid (markers) for 1-butene (−,∘), 1-pentene (−−,×), 1-hexene (− ·, +), 1-heptene (⋯ ,∗), and 1-octene (−,□).

Also plotted in Figure 6.16 (as markers) are the negative enthalpies of vaporization of the pure substances from Gallant and Yaws (1992). It is seen that at low temperatures the enthalpy change of the pure volatile approaches that of the volatile-polyethylene mixture. However, as temperature increases, the magnitude of the enthalpy change of the pure substance decreases rapidly. This rapid decrease is associated with the approach to the critical temperature at which the pure substance cannot exist in a condensed phase and the enthalpy of vaporization is zero. This same behavior does not occur in the polyethylene mixtures because the condensed phase is maintained by the large (sub-critical) molecules of the polymer melt.

6.3.3 Simulation Results for HDPE

Simulated DSC results were generated at heating rates of 5, 10, and 50 K/min to coincided with the available literature data. The other scenario parameters were chosen to coincide with the experiments of Conesa et al. (1996). Specifically, the sample pan was circular with a diameter and height of 5 mm, and the initial sample mass was 5 mg. For all cases, it was assumed that the heat losses were negligible, $\Delta\dot{Q}_L = 0$. For simplicity, it was assumed that ethylene and ethyl group properties were the same.

For the case of a heating rate of $\beta \equiv dT/dt = 5\ \mathrm{K/min}$, the terms in Equation (6.46) are plotted as a function of temperature in Figure 6.17. The label "Sensible" refers to $\left(C_{G,s} + C_O^g + C_O^m - C_{G,r}\right)\beta$, the label "Pyrolysis" refers to $\dot{Q}_{pyr}^g + \dot{Q}_{pyr}^m$, and the label "Devolatilization" refers to $\dot{Q}_{dev}$. The total differential energy absorption rate, $\Delta\dot{Q}_I$ goes to zero as the polyethylene mass in the sample cell goes to zero. At this point, the sample cell is identical to the reference cell. For materials or scenarios in which a significant amount of char is formed, $\Delta\dot{Q}_I$ should not go to zero, but the model presented above would have to be modified to account for residue formation.

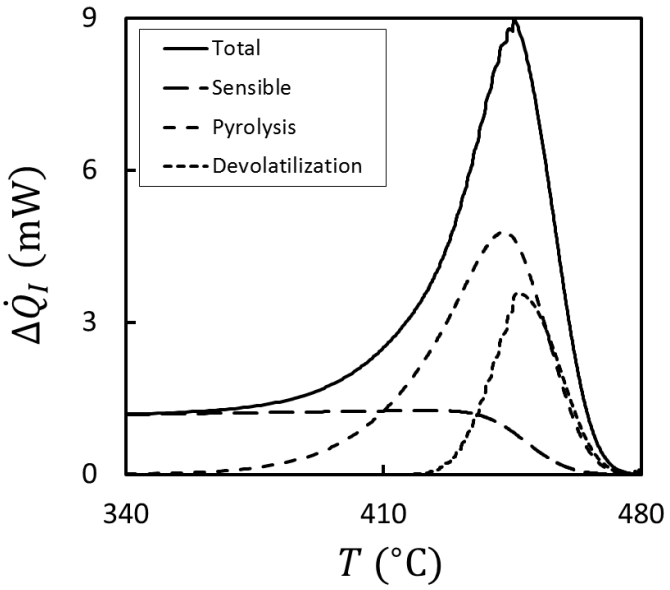

Figure 6.17: Energy absorption rates in the thermal decomposition of HDPE during a simulated DSC experiment at $\beta = 5$ K/min.

The oscillations observed at the peak of the total heating rate differential in Figure 6.17 are associated with the turning on of the loss rates for larger molecules as T increases. From Equation (5.35), $L_i = 0$ until $P_i > P$. Since $P_i = H_{X,i}X_i^m$ and since $H_{X,i}$ increases with temperature and X_i^m increases with time as the pyrolysis reactions proceed, P_i will increase until L_i is switched on. Once L_i is switched on, X_i^m will decrease since species i is lost from the melt phase, and, consequently, L_i will decrease. As L_i decreases, the total mass loss rate will decrease until the next largest species begins to devolatilize. Because there is a heat of devolatilization associated with mass loss from the melt phase, this oscillatory behavior in L_i leads to an oscillatory behavior in $\dot{Q}_{dev}$ and thus in $\Delta\dot{Q}_I$.

The energy associated with pyrolysis, $\dot{Q}_{pyr}^{g} + \dot{Q}_{pyr}^{m}$, contributes significantly more to the total energy absorption than the energy associated with devolatilization. This is not surprising since the covalent bonds broken during pyrolysis are stronger than the weak intermolecular bonds broken during devolatilization. Also, the energy absorption rate associated with pyrolysis grows and peaks before the energy absorption rate associated with devolatilization. This is a consequence of the bubbling loss mechanism which will not "turn on" until the pyrolysis reaction has generated a significant amount of volatile species. The ultimate decrease in $\dot{Q}_{pyr}$ is associated with the loss of pyrolyzable species from the sample pan. As pyrolysis slows down, devolatilization slows down as well since new species to devolatilize are no longer being generated.

The sensible heating rate difference, $\left(C_{G,s} + C_O^g + C_O^m - C_{G,r}\right)\beta$, essentially follows the TGA trace for the sample pan. This is because as the sample degrades, $C_O^g, C_O^m \to 0$, and the sample cell becomes identical to the reference cell. When the sample is completely removed, both cells contain only the sample pan filled with the purge gas. If any residue remains, then it will not be the case that the sensible heating rate differential goes to zero.

The total energy absorption differential is plotted as a function of temperature in Figure 6.18 for three different heating rates. As heating rate increases, both the height and the temperature of the peak increase. This is primarily a consequence of the change in coordinates from time to temperature, but there might be differences in the relative rates of pyrolysis and devolatilization leading the different results at different heating rates.

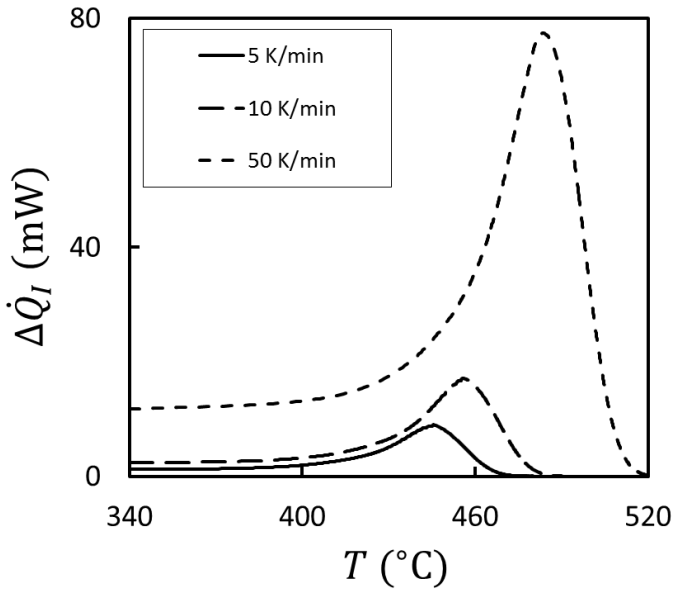

Figure 6.18: Total energy absorption differential at three heating rates.

The DSC simulation results are compared to literature data in terms of the normalized heating differential $\Delta\dot{q}_I \equiv \Delta\dot{Q}_I/m_0$. The results for $\beta = 5$ K/min are plotted in Figure 6.19 with data from Conesa et al. (1996) and Straka and Nahunkova (2004). The predicted DSC trace reaches its peak at a lower temperature than either of the data sets. The failure of the model to predict the correct peak decomposition temperature may be attributed to the kinetic parameters—the peak decomposition temperatures could easily be matched by increasing the pyrolysis activation energy. It is surprising that the peak decomposition temperature from the Straka and Nahunkova data is so large, ~510°C. Conesa et al. do not observe peak decomposition temperatures that large until the heating rates larger than 25 K/min. The predicted maximum heating differential is on the order of magnitude of the Straka and Nahunkova data, but Conesa et al. peak is

almost one order of magnitude smaller than the simulated result. Because of the significant difference between the two data sets, there is clearly a large amount of experimental error in at least one of the experiments. Until this experimental error can be characterized, it is not possible to invalidate any DSC model. Also of interest from Figure 6.19 is the fact that in the Straka and Nahunkova data, $\Delta\dot{q}_I$ does not go to zero as is expected. This could indicate a significant amount or residue remaining in the sample cell, but it is also possible that the authors did not record or report the final stages of degradation. The model presented here does not include a residue formation component. It will therefore always predict that the differential heat will go to zero as $T \to \infty$. Neglecting char formation is justifiable since the measured mass in TGA data for HDPE goes to zero at large temperatures. Before the onset of pyrolysis, $\Delta\dot{q}_I$ should not be zero as it is in the Conesa et al. data.

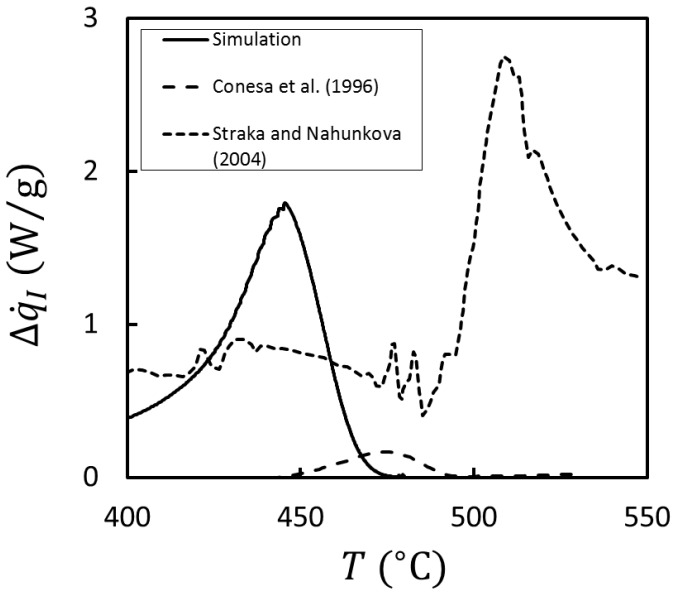

Figure 6.19: Normalized DSC heating differential at $\beta = 5$ K/min.

The predicted and experimental DSC traces for $\beta = 10$ K/min are plotted in Figure 6.20. The data are from Cozzani et al. (1995) and Jinno et al. (2004). The peak decomposition temperatures are in much better agreement for this scenario. The order of magnitude of the peak differential heating is similar between the predicted results and both sets of experimental data. However, from inspection of Figure 6.20, it seems plausible that the Jinno et al. data is incorrectly shifted upward. This hypothesis is supported by the fact that the reported data from Jinno et al. do not go to zero at high temperatures as would be expected. Once again, the simulations underpredict the temperature at which peak sample cell energy absorption occurs. Both sets of experimental data reach peak energy absorption at around 470°C whereas the simulated DSC trace peaks at approximately 455°C. Surprisingly, the peak energy absorption

temperature for the $\beta = 5\ \mathrm{K/min}$ experiments is either greater than (in the Straka and Nahunkova data) or equal to (in the Conesa et al. data) the peak energy absorption temperature for the $\beta = 10\ \mathrm{K/min}$ experiments. The model used in the simulations predicts that the temperature of peak energy absorption in the sample cell increases with heating rate. From inspection of Figure 6.20 it would seem that the Cozzani et al. is more consistent with the expected result. First, the sensible storage differential, corresponding to $\Delta\dot{q}_I$ at low temperatures, agrees closely with the value predicted by the model. Second, Cozzani et al. report that $\Delta\dot{q}_I$ goes to zero at high temperatures which is the physically reasonable result considering that minimal residue formation is observed in HDPE pyrolysis.

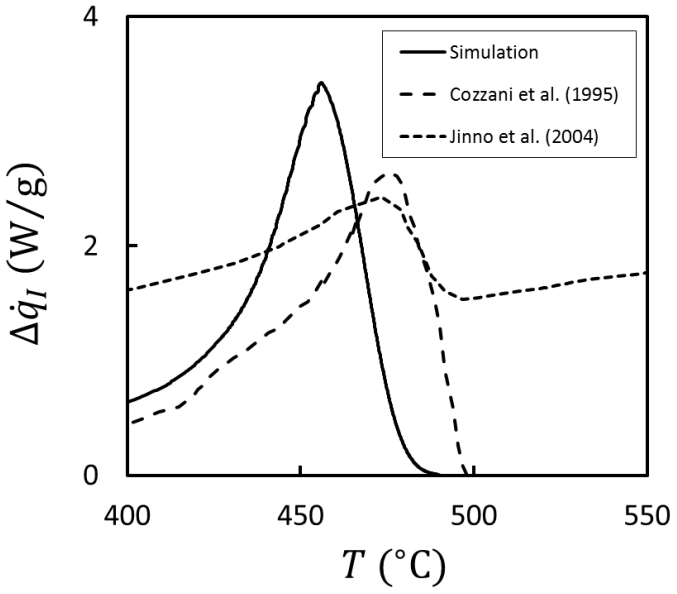

Figure 6.20: Normalized DSC heating differential at $\beta = 10\ \mathrm{K/min}$.

Only a single data set was available for the heating rate of 50 K/min. This data was from Jinno et al. (2004). Once again, the model underpredicts the peak energy absorption temperatures This is further evidence that the pyrolysis activation energies used in the simulations are too low. The initial sensible energy storage rate differences are comparable in this scenario. However, the model overpredicts the peak energy input differential by a factor of almost two. Again, the high temperature energy input differential does not go to zero in the Jinno et al. data. This is further evidence that the data from Jinno et al. is either incorrectly reported or biased.

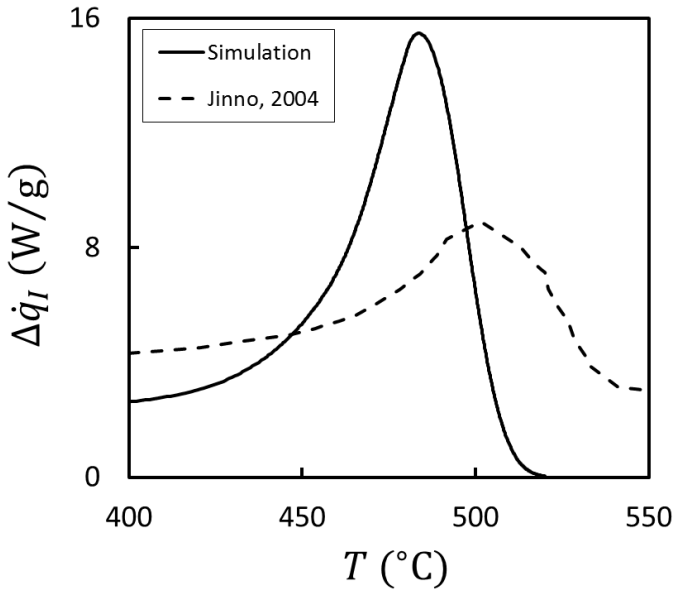

Figure 6.21: Normalized DSC heating differential at $\beta = 50$ K/min.

6.3.4 DSC Conclusions

A detailed model of DSC experiments was presented. This model accounts for pyrolysis chemistry with a chemically consistent random scission mechanism.

Devolatilization is treated as a simplified form of bubbling mass loss developed in Chapter 5. Additionally, accumulation of gas phase mass and gas phase pyrolysis are accounted for inside the sample pan. The model can be used to predict the various components contributing to DSC output data. Specifically, the differential heat input is decomposed into sensible, chemical (pyrolysis), and devolatilization terms.

The pyrolysis reaction was parameterized by the RMD initiation reaction parameters predicted in Chapter 3. Heat capacities and gas phase enthalpies are accounted for using group additivity models, and the enthalpy of devolatilization is determined from a correlation for the Henry constant of hydrocarbons in polyethylene.

The model was used to predict DSC traces at three heating rates. The results were compared to experimental data for all three scenarios. It was found that the peak decomposition temperature was consistently, but slightly, underpredicted. This can be attributed to errors in the pyrolysis model—either the mechanism, which is approximate, or the rates. The simulated peak heat input differential is generally of the same order of magnitude as the experimental data, but significant differences were observed. More troubling are the differences in the various literature data sets. Part of the problem might be attributed to a simple measurement bias as seems to be the case in the data reported by Jinno et al. (2004). Some of the data seems to be unphysical. Conesa et al. (1996) report that the input heat differential is initially zero which should not be the case if there is material in the sample pan. The data from Straka and Nahunkova (2004) and Jinno et al.

(2004) do not go to zero at large temperatures. Since HDPE does not produce significant pyrolysis residue, this implies that there are measurement or reporting errors.

7: Conclusions

7.1 Summary of Main Results

The objective of this dissertation was to improve the modeling capabilities for the thermal degradation of thermoplastics. This work is motivated by the need for designing less flammable consumer materials and finding optimal ways to reuse large amounts of plastic waste as was described in Chapter 1. High-density polyethylene (HDPE) was chosen as a test case because of its widespread use and because of the large amount of available literature data. Additionally, the chemical and structural simplicity of HDPE make it ideal for developing and testing new models.

In Chapter 2, several small scale experiments were identified for providing validation data. Literature data were collected for three of these experiments. It was found that there is a significant amount of disparity in the reported results for HDPE. Part of this difference might be attributed to differences in the exact material used, but it seems that there remains a significant amount of imprecision in the implementation of these experiments. It is hoped that the modeling tools developed in this dissertation will prove useful for designing better small scale thermal degradation testing apparatuses. As a preliminary to model derivation, the test tube pyrolysis of HDPE was recorded with a high-speed camera. The principal qualitative observation of these tests was that thermally degrading polyethylene vigorously bubbles. It was observed that the bubbles are spherical and do not break or coalesce. Measurements were made of bubble size distributions and

velocities at several stages of pyrolysis. It seems that there is a slight decrease in average bubble diameter as pyrolysis proceeds.

A modeling framework was presented in the second half of Chapter 2 in terms of the tools and equations appropriate at three different length scales. Of critical importance is the mesoscale at which microscale results are related to the transport equations needed to model realistic engineering problems. It was shown that population balance equations (PBEs) provide a general formalism for modeling the mesoscale dynamics of complex materials such as thermoplastics. At the microscale, it was shown how elementary pyrolysis reactions could be generically described by dissociation and addition reaction templates. The rate constant matrices that parameterize these reaction templates are then related to the breakage and aggregation rates in a discrete PBE. The continuous PBE used to model the mesoscale is just an approximation to the exact discrete PBE arising out of the user specified reaction templates.

Microscale modeling was treated in Chapter 3 by considering the details of pyrolysis chemistry. The literature on condensed phase pyrolysis mechanisms was surveyed to identify plausible models. Once a reasonable mechanism is identified, it is necessary to parameterize that mechanism with kinetic parameters. Condensed phase measurements of pyrolysis kinetics are currently unavailable, and so two alternative approaches were used to estimate the Arrhenius parameters for an HDPE chain initiation reaction. The first approach was to compile experimental results for the gas phase pyrolysis of *n*-alkanes which are structurally similar to HDPE molecules. Gas phase

analogs can only provide qualitative information about the relative importance of various condensed phase reactions, and so reactive molecular dynamics (RMD) was employed to obtain quantitative results. In the RMD simulations, it was found that larger polyethylene chains tend to break faster than smaller chains. Furthermore, the location of the initial backbone scission reaction was seen to be randomly distributed across the length of the chain.

Although fundamental results such as RMD are promising, the calculations are computationally expensive, and the results are not yet well validated. The more traditional approach of using TGA data to calibrate Arrhenius parameters was used in Chapter 3 to estimate the kinetics for three thermal degradation models. In addition to a commonly used single-step Arrhenius model, two PBEs were used: random scission and radical depolymerization. For the two PBEs a critical chain size loss model was used. The calibration was performed using sequential quadratic programming and a genetic algorithm for HDPE and poly(methyl methacrylate) (PMMA). Optimal solutions were found by minimizing the sum of squared errors between the models and data. The kinetic compensation effect was observed in plots of the objective function. It was found that all three models could be parameterized to fit the data, but that the solutions were not unique. The non-uniqueness of calibrated kinetic parameters presents a significant obstacle to using these parameters in scenarios that are significantly different from TGA.

A challenge for using PBEs to model polymer pyrolysis at the mesoscale is that the standard solution methods are either too slow to be coupled to continuum scale

models or they do not preserve the necessary information—i.e. pyrolysis gas composition. This obstacle was addressed in Chapter 4 by testing a hybrid sectional-moment method. The method allows for the preservation of detailed information for the small species in the number density function while describing the vast majority of species with low-order moments. A simple error analysis was performed for the case of random breakage. The method was seen to be fast and accurate for random breakage, constant kernel aggregation, additive kernel aggregation, and combined random breakage and constant kernel aggregation. The model was also compared to the global direct quadrature method of moments (DQMOM). It was demonstrated that error could be reduced by further discretization or, more effectively, by increasing the number of quadrature nodes within the sections.

The primary issue in modeling thermal degradation at the continuum scale is predicting the time required for pyrolysis products to exit the condensed phase. Based on the observation that thermally degrading HDPE produces a large number of rapidly moving bubbles, a bubbling mass loss mechanism was developed and tested in Chapter 5. The model depends upon several thermophysical properties that are not well characterized or modeled for complex materials such as thermoplastics. A literature review was performed to identify the best available models for properties such as density, diffusivity, and viscosity for HDPE. The model was shown to make reasonable for predictions of isothermal TGA data for early stages of degradation. It is hypothesized that the underprediction of the mass loss rate at high conversions is due to diffusional surface

mass loss increasing in relative importance as the sample volume decreases. Furthermore, the model predictions were better at low temperatures. Since diffusivity increases rapidly with temperatures, it is likely that surface loss is also more important at high temperatures.

In Chapter 6, the pyrolysis rates and mechanisms, the approximate PBE method, and the bubbling loss model were used to analyze two applications of engineering interest. Material flammability is partly characterized by piloted ignition experiments. Random scission pyrolysis and bubbling mass loss were used to predict the temperature, time, and external heat load required to sustain a flame in piloted ignition in a thin sample of HDPE. The predicted ignition temperatures were seen to be around 40-100 K too high. This overprediction is believed to be due to neglecting surface oxidation which, from TGA data, is seen to significantly decrease the thermal stability of HDPE.

The second application of engineering importance is modeling differential scanning calorimetry (DSC). In addition to the tools used for piloted ignition, gas phase species conservation and conservation of energy equations were utilized. Group additivity principles were used to model the thermodynamic properties of the pyrolyzing sample. It was shown how a correlation for the Henry constants of the volatile species could be used to predict the enthalpy change associated with removing volatile molecules from the melt phase. The DSC model predictions were compared to literature data at three heating rates. Although the peak decomposition temperature was consistently under-predicted, the simulated results were generally on the order of magnitude of the

experimental data. Unfortunately, there is too much variance in the literature data for the model to be properly validated. Several problems with the literature data were pointed out. Some of the data indicates that the initial mass in the sample pan is zero. Other data sets indicate a significant amount of residue which is not observed in TGA experiments.

7.2 SUGGESTIONS FOR FUTURE WORK

The inherent complexity of polymer thermal degradation lends itself to many possible avenues for future research. The models presented here represent only a first step towards accurately describing the coupled physics of pyrolysis and devolatilization. The discrepancy in much of the literature data indicates that a significant amount of work remains to be done to properly characterize small scale thermal degradation experiments. Future progress should therefore proceed carefully and rationally. Before spending significant effort on developing new physical models, the link between models and experiment should be more firmly established. In the course of this research, it was found that although there is a significant amount of literature data from thermal degradation experiments, there is not much systematic uncertainty analysis accompanying this data. Progress on the experimental front will require detailed uncertainty analysis and device modeling to identify and quantify possible sources of error.

With better experimental data, it will be possible to better calibrate and validate the models. As a first step that can be performed in the absence of well characterized experimental data, a systematic sensitivity analysis can help identify what physical processes need to be more carefully studied. Calibration can be performed across

multiple coupled modeling domains with a variety of experiments and experimental scenarios. The models can be validated by more complex scenarios such as steady burning experiments.

It is also important to incorporate more materials into the modeling framework. Different materials such as PMMA will pyrolyze and devolatilize through slightly different mechanisms than HDPE. As more physical models for different physical mechanisms are developed, it will become increasingly important to organize the tools into a well-designed code base for easy use and extension.

Once a flexible, robust, and validated toolkit has been developed for modeling the thermal degradation of polymers, it will be possible to reliably design better materials for flammability and better processes for reuse. Flammability may be decreased by modifying the chemical structure of the polymer or by the use of flame retardants. Most flame retardants function by inhibiting the gas phase combustion reaction, but it has recently been found that the addition of nanoparticles reduce polymer flammability by changing the chemical or transport properties of the condensed phase. The mechanism by which nanoparticles function to reduce flammability may be explored by developing the methods presented in this dissertation.

Bibliography

Amar AJ, Blackwell BF, Edwards JR. One-Dimensional Ablation with Pyrolysis Gas Flow Using a Full Newton's Method and Finite Control Volume Procedure. 39th AIAA Thermophysics Conference, 25-27 June 2007, Miami, FL.

Atreya A, Wichman IS. Heat and Mass Transfer During Piloted Ignition of Cellulosic Solids. Journal of Heat Transfer 1989; 111:719-725.

Ayres WM, Bens EM. Differential Thermal Studies with Simultaneous Gas Evolution Profiles. Analytical Chemistry 1961; 33:568-572.

Balta Calleja FJ, Rueda DR. Study of the Interlamellar Folded Structure of Polyethylene as Revealed by Melting Point and Crystallinity 1974; 6:216-221.

Benson SW. Thermochemical Kinetics. New York: John Wiley & Sons; 1976.

Berry GC, Fox TG. The Viscosity of Polymers and their Concentrated Solutions. Advances in Polymer Science 1968; 5:261-357.

Bird RB, Stewart WE, Lightfoot EN. Transport Phenomena. New York: John Wiley & Sons; 1960.

Bird RB, Curtiss CF, Armstrong RC, Hassager O. Dynamics of Polymeric Liquid; Volume 1: Fluid Mechanics. New York: John Wiley & Sons; 1987.

Blander M, Katz JL. Bubble Nucleation in Liquids. AIChE Journal 1975; 21:833-848.

Bockhorn H, Hentschel J, Hornung A, Hornung U. Environmental Engineering: Stepwise Pyrolysis of Plastic Waste. Chemical Engineering Science 1999; 54:3043-3051.

Boyd RH. In: Conley RT, editor. Thermal Stability of Polymers. New York: Marcel Dekker, Inc., 1970. p. 47.

Breen C, Last PM, Taylor S, Komadel P. Synergic Chemical Analysis — The Coupling of TG with FTIR, MS and GC-MS: 2. Catalytic Transformation of the Gases Evolved During the Thermal Decomposition of HDPE using Acid-activated Clays. Thermochimica Acta 2000; 363:93-104.

Brenner DW. Empirical Potential for Hydrocarbons for Use in Simulating the Chemical Vapor Deposition of Diamond Films. Physical Review B 1990; 42:9458-9471.

Brown ME. Introduction to Thermal Analysis—Techniques and Applications; 2nd Edition. Dordrecht: Kluwer Academic Publishers; 2001.

Bruns MC, Koo JH, Ezekoye OA. Population-Based Models of Thermoplastic Degradation: Using Optimization to Determine Model Parameters. Polymer Degradation and Stability 2009; 94: 1013-1022.

Bruns MC, Ezekoye OA. Pyrolysis and Devolatilization of High-Density Polyethylene. 10th IAFSS Symposium 2011; College Park, MD.

Butler KM. A Numerical Model for Combustion of Bubbling Thermoplastic Materials in Microgravity. National Institute of Standards and Technology Report NISTIR 6894, Gaithersburg, MD, 2002.

Ceamanos J, Mastral JF, Millera A, Aldea ME. Kinetics of Pyrolysis of High Density Polyethylene. Comparison of Isothermal and Dynamic Experiments. Journal of Analytical and Applied Pyrolysis 2002; 65:93-110.

Conesa JA, Marcilla A, Font R, Caballero JA. Thermogravimetric Studies on the Thermal Decomposition of Polyethylene. Journal of Analytical and Applied Pyrolysis 1996; 36:1-15.

Cozzani V, Nicolella C, Petarca L, Rovatti M, Tognotti L. A Fundamental Study on Conventional Pyrolysis of a Refuse-Derived Fuel. Industrial & Engineering Chemistry Research 1995; 34:2006-2020.

Cullis CF, Hirschler MM. The Combustion of Organic Polymers. Oxford: Clarendon Press; 1981.

Cussler EL. Multicomponent Diffusion. Amsterdam: Elsevier Scientific Publishing Company; 1976.

Deen WM. Analysis of Transport Phenomena. Oxford: Oxford University Press; 1998.

Dente ME, Ranzi EM. In: Albright LF, Crynes BL, Corcoran WH, editors. Pyrolysis: Theory and Industrial Practice. New York: Academic Press, 1983. p. 133.

Drysdale DD, Thomson HE. Flammability of Plastics II: Critical Mass Flux at the Firepoint. Fire Safety Journal 1989; 14:179-188.

Duda JL, Vrentas JS, Ju ST, Liu HT. Prediction of Diffusion Coefficients for Polymer-Solvent Systems. AIChE Journal 1982; 28:279-285.

Egloff G, Sherman J, Dull RB. Boiling Point Relationships Among Aliphatic Hydrocarbons. The Journal of Physical Chemistry 1940; 44:730-745.

Epstein PS, Plesset MS. On the Stability of Gas Bubbles in Liquid-Gas Solutions. The Journal of Chemical Physics 1950; 18(11):1505-1509.

Faravelli T, Bozzano G, Scassa C, Perego M, Fabini S, Ranzi E, Dente M. Gas Product Distribution from Polyethylene Pyrolysis. Journal of Analytical and Applied Pyrolysis 1999; 52:87-103.

Favelukis M, Albalak RJ. In: Albalak RJ, editor. Polymer Devolatilization. New York: Marcel Dekker, Inc., 1996. p. 103.

Ferriol M, Gentilhomme A, Cochez M, Oget N, Mielosynski JL. Thermal Degradation of Poly(methyl Methacrylate) (PMMA): Modelling of DTG and TG Curves. Polymer Degradation and Stability 2003; 79:271-281.

Flory PJ. Molecular Size Distribution in Ethylene Oxide Polymers. Journal of the American Chemical Society 1940; 62:1561-1565.

Flory PJ. Principles of Polymer Chemistry. Ithaca: Cornell University Press; 1953.

Fox RO. Computational Models for Turbulent Reacting Flows. Cambridge: Cambridge University Press; 2003.

Frederick WJ, Mentzer CC. Determination of Heats of Volatilization for Polymers by Differential Scanning Calorimetry. Journal of Applied Polymer Science 1975; 19:1799-1804.

Gallant RW, Yaws CL. Physical Properties of Hydrocarbons. Houston: Gulf Publishing Company; 1992.

Gear CW. Numerical Initial Value Problems in Ordinary Differential Equations. Englewood Cliffs, NJ: Prentice-Hall, Inc.; 1971.

Gelbard F, Tambour Y, Seinfeld JH. Sectional Representations for Simulating Aerosol Dynamics. Journal of Colloid and Interface Science 1980; 76: 541-556.

Gordon RG. Error Bounds in Equilibrium Statistical Mechanics. Journal of Mathematical Physics 1968; 9:655-663.

Grassie N, Scott G. Polymer Degradation and Stabilization. Cambridge: Cambridge University Press; 1985.

Hernandez M, Garcia AN, Marcilla A. Study of the Gases Obtained in Thermal and Catalytic Flash Pyrolysis of HDPE in a Fluidized Bed Reactor. Journal of Analytical and Applied Pyrolysis 2005; 73:314-322.

Hill PJ, Ng KM. New Discretization Procedure for the Breakage Equation. Process Systems Engineering 1995; 41:1204-1216.

Hopkins D, Quintiere JG. Material Fire Properties and Predictions for Thermoplastics. Fire Safety Journal 1996; 26:241-268.

Hounslow MJ, Ryall RL, Marshall VR. A Discretized Population Balance for Nucleation, Growth, and Aggregation. AIChE Journal 1988; 34:1821-1832.

Inaba A, Kashawagi T. A Calculation of Thermal Degradation Initiated by Random Scission. 1. Steady-State Radical Concentration. Macromolecules 1986; 19:2412-2419.

Jellinek HHG. In: Jellinek HHG, editor. Aspects of Degradation and Stabilization of Polymers. Amsterdam: Elsevier Scientific Publishing Company, 1978. p. 1.

Jinno D, Gupta AK, Yoshikawa K. Thermal Decomposition Characteristics of Critical Components in Solid Wastes. Environmental Engineering Science 2004; 21:65-72.

Knyazev VD. Effects of Chain Length on the Rates of C-C Bond Dissociation in Linear Alkanes and Polyethylene. Journal of Physical Chemistry A 2007; 111:3875-3883.

Kossiakoff A, Rice FO. Thermal Decomposition of Hydrocarbons, Resonance Stabilization and Isomerization of Free Radicals. Journal of the American Chemical Society 1943; 65:590-595.

Kumar S, Ramkrishna D. On the Solution of Population Balance Equations by Discretization—I. A Fixed Pivot Technique. Chemical Engineering Science 1996a; 51:1311-1332.

Kumar S, Ramkrishna D. On the Solution of Population Balance Equations by Discretization—II. A Moving Pivot Technique. Chemical Engineering Science 1996b; 51:1333-1342.

Kunugi T, Sakai T, Kazuhiko S, Sasaki Y. Kinetics and Mechanism of the Thermal Reaction of Ethylene. Industrial & Engineering Chemistry Fundamentals 1969; 8:375-383.

Kuroki T, Sawaguchi T, Niikuni S, Ikemura T. Mechanism for Long-Chain Branching in the Thermal Degradation of Linear High-Density Polyethylene. Macromolecules 1982; 15:1460-1464.

Lyon RE. Pyrolysis Kinetics of Char Forming Polymers. Polymer Degradation and Stability 1998; 61:201-210.

Lyon RE. In: Grand AF, Wilkie CA, editors. Fire Retardancy of Polymeric Materials. New York: Marcel Dekker, Inc., 2000. p. 391.

Maloney DP, Prausnitz JM. Solubilities of Ethylene and Other Organic Solutes in Liquid, Low-Density Polyethylene in the Region 124˚ to 300˚C. AIChE Journal 1976; 22:74-82.

Marchisio DL, Fox RO. Solution of Population Balance Equations using the Direct Quadrature Method of Moments. Aerosol Science 2005; 36: 43-73.

Mastral FJ, Esperanza E, Berrueco C, Juste M, Ceamanos J. Fluidized Bed Thermal Degradation Products of HDPE in an Inert Atmosphere and in Air-Nitrogen Mixtures. Journal of Analytical and Applied Pyrolysis 2003; 70:1-17.

Mastral JF, Berrueco C, Ceamanos J. Modelling of the Pyrolysis of High Density Polyethylene Product Distribution in a Fluidized Bed Reactor. Journal of Analytical and Applied Pyrolysis 2007; 79:313-322.

McCoy BJ, Wang M. Continuous-Mixture Fragmentation Kinetics: Particle Size Reduction and Molecular Cracking. Chemical Engineering Science 1994; 49: 3773-3785.

McCoy BJ, Madras G. Degradation Kinetics of Polymers in Solution: Dynamics of Molecular Weight Distributions. AIChE Journal 1997; 43:802-810.

McCoy BJ, Madras G. Analytical Solution for a Population Balance Equation with Aggregation and Fragmentation. Chemical Engineering Science 2003; 58: 3049-3051.

McGraw R. Description of Aerosol Dynamics by the Quadrature Method of Moments. Aerosol Science and Technology 1997; 27: 255-265.

Merrill EW. In: Albalak RJ, editor. Polymer Devolatilization. New York: Marcel Dekker, Inc., 1996. p. 13.

Michal J, Mitera J, Tardon S. Toxicity of Thermal Degradation Products of Polyethylene and Polypropylene. Fire and Materials 1976; 1:160-168.

Mills AF. Heat Transfer; Second Edition. Upper Saddle River, NJ: Prentice Hall; 1999.

Murata K, Sato K, Sakata Y. Effect of Pressure on Thermal Degradation of Polyethylene. Journal of Analytical and Applied Pyrolysis 2004; 71:569-589.

Montroll EW, Simha R. Theory of Depolymerizaiton of Long Chain Molecules. Journal of Chemical Physics 1940; 8:721-727.

Nelson GL. In: Grand AF, Wilkie CA, editors. Fire Retardancy of Polymeric Materials. New York: Marcel Dekker, Inc., 2000. p. 1.

Ng SH, Seoud H, Stanciulescu M. Conversion of Polyethylene to Transportation Fuels through Pyrolysis and Catalytic Cracking. Energy & Fuels 1995; 9:735-742.

Nyden MR, Forney GP, Brown JE. Molecular Modeling of Polymer Flammability: Application to the Design of Flame-Resistant Polyethylene. Macromolecules 1992; 25:1658-1666.

O'Neill MJ. Measurement of Specific Heat Functions by Differential Scanning Calorimetry. Analytical Chemistry 1966; 38:1331-1336.

Ozawa T. A New Method of Analyzing Thermogravimetric Data. Bulletin of the Chemical Society of Japan 1965; 38:1881-1886.

Pavlinov LI, Marchenko GN, Lebedev YA. Calculations of the Thermodynamic Properties of Polymers. Russian Chemical Reviews 1984; 53:683-696.

Peebles LH. Molecular Weight Distributions in Polymers. New York: Interscience Publishers; 1971.

Poling BE, Prausnitz JM, O'Connell JP. The Properties of Gases and Liquids: Fifth Edition. New York: McGraw-Hill; 2001.

Poutsma ML. Reexamination of the Pyrolysis of Polyethylene: Data Needs, Free-Radical Mechanistic Considerations, and Thermochemical Kinetic Simulation of Initial Product-Forming Pathways. Macromolecules 2003; 36: 8931-8957.

Powers DR, Corcoran WH. Pyrolysis of *n*-Butane—Explicit Effects of Primary and Secondary Butyl Radicals and of Secondary Reactions. Industrial & Engineering Chemistry Fundamentals 1974; 13:351-355.

Prausnitz JM, Lichtenthaler RN, Gomes de Azevedo E. Molecular Thermodynamics of Fluid-Phase Equilibria. Upper Saddle River: Prentice Hall PTR; 1999.

Press WH, Teukolsky SA. Orthogonal Polynomials and Gaussian Quadrature with Nonclassical Weight Functions. Computers in Physics 1990; 4:423-426.

Quackenbos HM. Thermal and Oxidative Effects in Polyethylene above 200°C. Polymer Engineering and Science 1966; 6:117-123.

Quintiere JG. Fundamentals of Fire Phenomena. Chichester: John Wiley & Sons, Ltd.; 2006.

Ralston A, Rabinowitz P. A First Course in Numerical Analysis (Second Edition). Mineola: Dover Publications, Inc.; 2001.

Ramkrishna D. Population Balances: Theory and Applications to Particulate Systems in Engineering. San Diego: Academic Press; 2000.

Ranzi E, Dente M, Faravelli T, Bozzano G, Fabini S, Nava R, Cozzani V, Tognotti L. Kinetic modeling of polyethylene and polypropylene thermal degradation. Journal of Analytical and Applied Pyrolysis 1997; 40-41: 305-319.

Rasbash DJ, Drysdale DD, Deepak D. Critical Heat and Mass Transfer at Pilot Ignition of a Material. Fire Safety Journal 1986; 10:1-10.

Rich D, Lautenberger C, Torero JL, Quintiere JG, Fernandez-Pello C. Mass Flux of Combustible Solids at Piloted Ignition. Proceedings of the Combustion Institute 2007; 31:2653-2660.

Ruzicka K, Majer V. Simultaneous Treatment of Vapor Pressures and Related Thermal Data Between the Triple and Normal Boiling Temperatures for *n*-alkanes C_5-C_{20}. Journal of Physical and Chemical Reference Data 1994; 23:1-39.

Sakata Y, Uddin MA, Koizumi K, Murata K. Thermal Degradation of Polyethylene Mixed with Poly(Vinyl Chloride) and Poly(Ethyleneterephthalate). Polymer Degradation and Stability 1996; 53:111-117.

Schreiber HP, Tewari YB, Patterson D. Thermodynamic Interactions in Polymer Systems by Gas-Liquid Chromatography. III. Polyethyelene-hydrocarbons. Journal of Polymer Science: Polymer Physics Edition 1973; 11:15-24.

Scott WT. Analytic Studies of Cloud Droplet Coalescence I. Journal of Atmospheric Sciences 1968; 25:54-65.

Sezgi NA, Cha WS, Smith JM, McCoy BJ. Polyethylene Pyrolysis: Theory and Experiments for Molecular-Weight-Distribution Kinetics. Industrial & Engineering Chemistry Research 1998; 37:2582-2591.

Shampine LF, Reichelt MW. The MATLAB ODE Suite. SIAM Journal on Scientific Computing 1997; 18:1-22.

Siegel R, Howell JH. Thermal Radiation Heat Transfer; 4th Edition. London: Taylor & Francis; 2002.

Simha R. Kinetics of Degradation and Size Distribution of Long Chain Polymers. Journal of Applied Physics 1941; 12:569-578.

Simha R, Wall LA, Blatz PJ. Depolymerization as a Chain Reaction. Journal of Polymer Science 1950; 5:615-632.

Simha R, Wall LA. Some Aspects of Depolymerization Kinetics. Journal of Polymer Science 1951; 6:39-44.

Simha R, Wall LA. Kinetics of Chain Depolymerization. The Journal of Physical Chemistry 1952; 56:707-715.

Smith KD, Stoliarov SI, Nyden MR, Westmoreland PR. RMDff: A Smoothly Transitioning, Forcefield-Based Representation of Kinetics for Reactive Molecular Dynamics Simulations. Molecular Simulation 2007; 33:361-368.

Smith KD, Bruns M, Stoliarov SI, Nyden MR, Ezekoye OA, Westmoreland PR. Assessing the Effect of Molecular Weight on the Kinetics of Backbone Scission Reactions in Polyethylene Using Reactive Molecular Dynamics. Polymer 2011; 52:3104-3111.

Smoluchowski MZ. Versuch einer Mathematischen Theorie der Koagulationskinetick Kolloider Lösungen. Zeitschrift für Physikalische Chemie 1917; 92:129.

Speyer RF. Thermal Analysis of Materials. New York: Marcel Dekker, Inc.; 1994.

Staggs JEJ. Modelling Random Scission of Linear Polymers. Polymer Degradation and Stability 2002; 76:37-44.

Staggs JEJ. Population Balance Models for the Thermal Degradation of PMMA. Polymer 2007; 48:3868-3876.

Stoliarov SI. Determination of the Heats of Gasification of Polymers Using Differential Scanning Calorimetry. Polymer Degradation and Stability 2008; 93:422-427.

Straka P, Nahunkova J. Thermal Reactions of Polyethylene with Coal (TG/DSC Approach). Journal of Thermal Analysis and Calorimetry 2004; 76:49-53.

Sundaram KM, Froment GF. Modeling of Thermal Cracking Kinetics. 3. Radical Mechanisms for the Pyrolysis of Simple Paraffins, Olefins, and their Mixtures. Industrial & Engineering Chemistry Fundamentals 1978; 17:174-182.

Tewarson A. In: Lewin M, Atlas SM, Pearce EM, editors. Experimental Evaluation of Flammability Parameters of Polymeric Materials. New York: Plenum Press, 1982. pp. 97-153.

Thomson HE, Drysdale DD. Flammability of Plastics I: Ignition Temperatures. Fire and Materials 1987; 11:163-172.

Thomson HE, Drysdale DD, Beyler CL. An Experimental Evaluation of Critical Surface Temperature as a Criterion for Piloted Ignition of Solid Fuels. Fire Safety Journal 1988; 13:185-196.

Uddin MA, Koizumi K, Murata K, Sakata Y. Thermal and Catalytic Degradation of Structurally Different Types of Polyethylene into Fuel Oil. Polymer Degradation and Stability 1997; 56:37-44.

Van Duin ACT, Dasgupta S, Lorant F, Goddard III WA. ReaxFF: A Reactive Force Field for Hydrocarbons. Journal of Physical Chemistry A 2001; 105:9396-9409.

Van Krevelen DW, te Nijenhuis K. Properties of Polymers (4th Edition). Amsterdam: Elsevier; 2009.

Vanni M. Approximate Population Balance Equations for Aggregation-Breakage Processes. Journal of Colloid and Interface Science 2000; 221:143-160.

Von Meerwall E, Beckman S, Jang J, Mattice WL. Diffusion of *n*-alkanes: Free-volume and Density Effects. Journal of Chemical Physics 1998; 108:4299-4304.

Von Meerwall E, Feick EJ, Ozisik R, Mattice WL. Diffusion in Binary Liquid *n*-Alkane and Alkane-Polyethylene Blends. Journal of Chemical Physics 1999; 111:750-757.

Vyazovkin S. A Unified Approach to Kinetic Processing of Nonisothermal Data. International Journal of Chemical Kinetics 1996; 28:95-101.

Wallis M, Bhatia SK. Kinetic Study of the Thermal Degradation of High Density Polyethylene. Polymer Degradation and Stability 2006; 91:1476-1483.

Walters RN, Hackett SM, Lyon RE. Heats of Combustion of High Temperature Polymers. Fire and Materials 2000; 24:245-252.

Wendlandt, WW. Thermal Analysis; 3rd Edition. New York: John Wiley & Sons; 1986.

Westerhout RWJ, Waanders J, Kuipers JAM, van Swaaij WPM. Kinetics of the Low-Temperature Pyrolysis of Polyethylene, Polypropylene, and Polystyrene Modeling, Experimental Determination, and Comparison with Literature Models and Data. Industrial & Engineering Chemistry Research 1997; 36:1955-1964.

Wichman IS. A Model Describing the Steady-State Gasificaiton of Bubble-Forming Thermoplastics in Response to an Incident Heat Flux. Combustion and Flame 1986; 63: 217-229.

Wu S. Surface and Interfacial Tensions of Polymer Melts: I. Polyethylene, Polyisobutylene, and Polyvinyl Acetate. Journal of Colloid and Interface Science 1969; 31:153-161.

Zielinski JM, Duda JL. In: Albalak RJ, editor. Polymer Devolatilization. New York: Marcel Dekker, Inc., 1996. p. 35.

Ziff RM, McGrady ED. The Kinetics of Cluster Fragmentation and Depolymerisation. Journal of Physics A: Mathematical and General 1985; 18:3027-3037.

Ziff RM, McGrady ED. Kinetics of Polymer Degradation. Macromolecules 1986; 19:2513-2519.